3-14-2014

Verification and Validation of Monte Carlo n-Particle Code 6 (MCNP6) with Neutron protection Factor Measurements of an Iron Box

Andrew W. Decker

VERIFICATION AND VALIDATION OF MONTE CARLO N-PARTICLE CODE 6 (MCNP6) WITH NEUTRON PROTECTION FACTOR MEASUREMENTS OF AN IRON BOX

THESIS

Andrew W. Decker, MAJ, USA

AFIT-ENP-14-M-05

DEPARTMENT OF THE AIR FORCE
AIR UNIVERSITY

AIR FORCE INSTITUTE OF TECHNOLOGY

Wright-Patterson Air Force Base, Ohio

The views expressed in this thesis are those of the author and do not reflect the official policy or position of the United States Air Force, Department of Defense, or the United States Government.

AFIT-ENP-14-M-05

VERIFICATION AND VALIDATION OF MONTE CARLO N-PARTICLE CODE 6 (MCNP6) WITH NEUTRON PROTECTION FACTOR MEASUREMENTS OF AN IRON BOX

THESIS

Presented to the Faculty

Department of Engineering Physics

Graduate School of Engineering and Management

Air Force Institute of Technology

Air University

Air Education and Training Command

In Partial Fulfillment of the Requirements for the

Degree of Master of Science

Andrew W. Decker, B.S.

MAJ, USA

27 March 2014

DISTRIBUTION STATEMENT A.
APPROVED FOR PUBLIC RELEASE; DISTRIBUTION UNLIMITED

AFIT-ENP-14-M-05

VERIFICATION AND VALIDATION OF MONTE CARLO N-PARTICLE CODE 6 (MCNP6) WITH NEUTRON PROTECTION FACTOR MEASUREMENTS OF AN IRON BOX

Andrew W. Decker, B.S.
MAJ, USA

Approved:

//signed//	07MAR14
LTC Stephen McHale, Ph.D. (Chairman)	Date
//signed//	07MAR14
Justin Clinton, Ph.D. (Member)	Date
//signed//	28FEB14
LTC Michael Shannon, Ph.D. (Member)	Date

AFIT-ENP-14-M-05

Abstract

Using a 1984 benchmark experiment, MCNP6 replicated the neutron flux and neutron protection factor (NPF) measurements of an iron box, which simulated a basic military vehicle, resulting in less than 5% difference from the published results. Additionally, the neutron flux spectrum of a ^{239}PuBe source was characterized using a Bonner Sphere Spectrometer (BSS) and the solution unfolded using the Maximum Entropy Deconvolution (MAXED) program, producing a χ^2/df of 0.97. Utilizing a steel box provided by the DTRA, measurements of neutron flux from a D-D neutron accelerator were recorded via BSS inside and outside of the box. Both flux spectra were unfolded through MAXED using MCNP6 computations as *a priori*, which resulted in χ^2/df values of 0.86 and 0.91, respectively. NPF assessments of the steel box were then conducted using experimental and MCNP6 flux spectra for the box, as well as *H*(10)* scaling, with final results differing by less than 1%. MAXED software was leveraged for all flux spectrum unfolding, incorporating updated BSS response functions generated within this research from MCNP6. This experiment and its conclusions strongly support the verification and validation of MCNP6 for modeling NPF assessments of military vehicles.

To my beloved wife;
this would never have been possible
without your love, support,
and understanding.

Acknowledgments

I would like to first thank God for giving me the strength and determination to succeed at AFIT. His blessings have enriched my life enormously, and I am sincerely grateful for all of His influence in my life. I next want to express my sincere love, respect, and admiration for my wife, who motivated and supported me throughout this long endeavor; this document is dedicated to her. I also wish to thank my two wonderful daughters for their continued love, support, and understanding.

I would also like to thank my Thesis Advisor, LTC Steve McHale, for all of his assistance and support. LTC McHale always provided sound advice, technical expertise, and unwavering encouragement throughout this research, and I am sincerely grateful for his time, efforts, and mentorship.

I wish to also thank the fellow members of my committee, Dr. Justin Clinton and LTC Michael Shannon. Dr. Clinton greatly assisted my understanding of radiation transport modeling, as well as patiently oversaw my running of the DD108 generator and helped significantly during my experiments. I wish to thank LTC Shannon for entrusting me with this research opportunity, as well as for all the support he, and the NSERC team, provided to facilitate my success. Maj. Ben Kowash also deserves a great deal of credit and thanks for his patience and expertise in helping me develop my understanding of MCNP6.

Lastly, I wish to thank all the faculty and staff at AFIT, especially those in the Department of Engineering Physics, for their professionalism, service, and support to all of us struggling to complete our programs. Thank you all very much!

Table of Contents

List of Figures

Figure Page

List of Tables

Table Page

VERIFICATION AND VALIDATION OF MONTE CARLO N-PARTICLE CODE 6 (MCNP6) WITH NEUTRON PROTECTION FACTOR MEASUREMENTS OF AN IRON BOX

I. Introduction

Current Risk

Since the collapse of the Union of Soviet Socialist Republics (USSR) and the end of the Cold War, the threat of a nuclear attack against the United States (US) or one of her allies has never been greater [1]. This risk not only arises from hostile nation-states, such as North Korea and Iran, but also from terrorist groups and similar non-state actors determined to acquire nuclear weapons technology. If a nuclear attack against American interests occurred, a significant portion of the US Army would likely respond to the ensuing devastation and humanitarian crisis. Units deployed in support of these efforts could be ordered to provide local and regional security, support the civil government, triage and evacuate the wounded, and possibly defeat an invading military force.

Individually, each of these missions would surpass the capabilities of the US Army's organic Nuclear, Biological, and Chemical (NBC) units, those soldiers specially trained and equipped to conduct operations in radiological environments. Consequently, the US response to even a single nuclear detonation would likely require soldiers from a variety of backgrounds within the US Army to operate within areas likely contaminated with radioactive fallout. Additionally, if a nuclear attack is perpetrated by an aggressive

nation-state, deployed soldiers could also face hostile forces and open combat amid radioactive fallout, or be required to conduct operations in areas at risk of future nuclear attack.

These scenarios present military commanders with a staggering challenge: how does one weigh the risks of radiation exposure to their soldiers against accomplishment of the mission? This determination might be simplified for dismounted soldiers wearing only the Mission-Oriented Protective Postures (MOPP) suit; however, to answer this question for mechanized and armored unit commanders, the US Army must understand the degree of radiation shielding afforded by these vehicle types. In March of 2011, during OPERATION TOMODACHI in Japan, this consideration became evident when such information was required to support operational decisions [2].

Currently, the degree of radiation protection provided by US Army vehicles is unknown for all but a handful of legacy items and variants. Additionally, the effort in recent years to provide vehicles with better protection to American soldiers in both Iraq and Afghanistan forced the Department of Defense (DoD) to rapidly field dozens of new armored combat vehicles and vehicle variants. Although many boasted superior ballistic protection, no experimental or computational evaluation of the radiological protection afforded by the vehicles was required [2]. Consequently, this information simply does not exist for the vast majority of wheeled and tracked vehicles in the US Army inventory.

Filling the Void

To counter this information gap, the Department of Defense tasked the Defense Threat Reduction Agency (DTRA) and the US Army Nuclear and Combating Weapons

of Mass Destruction Agency (USANCA) to devise a methodology for delivering this critical information into the hands of US Army commanders; fortunately, this task is not novel. Prior to the collapse of the USSR, the US Army routinely conducted experimental and computational assessments of mission critical platforms to determine the degree of radiological protection afforded to their crews [3, 4]. According to "The Final Report of Radiation Shielding in Armored Vehicles" published by the Defense Technical Information Center (DTIC) in 1988,

> Radiation protection measures have several applications. It is desirable to know the radiation protection factors of U.S. and allied vehicles since it will affect the best mode of deployment in the event of the reality, or even the threat of nuclear war. Similarly, the protection factors of potentially hostile vehicles will affect U.S. targeting doctrine. It is also important to make known to U.S. designers of vehicles of the future the best techniques for attaining good radiation protection, so that they may be implemented in an efficient and cost-effective manner [4].

Therefore, knowledge of each vehicle's degree of radiation shielding offered a variety of benefits at the tactical, operational, and strategic levels. Furthermore, by incorporating such factors into US Army vehicle fielding requirements, the DoD provided improved radiation protection to soldiers in a cost-effective manner.

The US Army quantifies radiation shielding into a value known as the radiation protection factor (RPF) for each vehicle variant, which represents the ability of that particular vehicle type to protect its occupants from different forms of external radiation. Each measurement depends on the thickness and composition of the shielding material, as well as the type and energy of the incident radiation. The specific type of RPF is calculated based upon the ratio of the radiation dose outside compared to the dose present inside the vehicle and may be determined using the equation

$$\text{RPF} = \frac{\text{Free Field Dose}}{\text{Dose Penetrating the Vehicle}}. \tag{1.1}$$

Since the two most biologically significant sources of radiation pursuant to a nuclear detonation consist of neutrons and secondary gammas, a more detailed analysis of a vehicle RPF can be obtained by defining both the neutron protection factor (NPF) and the gamma ray protection factor (GPF) [5]:

$$\text{NPF} = \frac{\text{Free Field Neutron Dose}}{\text{Neutron Dose Penetrating the Vehicle}} \tag{1.2}$$

$$\text{GPF} = \frac{\text{Free Field Gamma Dose}}{\text{Gamma Dose Penetrating the Vehicle}} \tag{1.3}$$

The clear implication to draw from these three equations is that the larger the RPF, the better the protection afforded by the vehicle to its crew.

The RPF assessment also conveys information concerning the optimal positioning of the vehicle, relative to the radiation source location, to minimize radiation exposure to the crew. Consequently, unit commanders and their staffs would consider vehicle RPF assessments invaluable for mission planning and risk assessment purposes when operating in hazardous radiation environments, thereby enabling commanders to employ their combat vehicle systems more safely and effectively.

Historically, the US Army pursued both experimental and computational approaches to solve for the RPF. These techniques were applied against dozens of

experiments involving the initial and residual radiation created by a nuclear weapon [3, 6]. When analyzing radiation shielding, initial radiation refers to any nuclear emissions occurring within the first minute after detonation. All subsequent radiation produced by a nuclear weapon or its effects beyond that time is considered residual radiation [7]. This distinction became important after it was discovered how different types of shielding provided varying levels of protection against different forms of radiation. At that time, the persistent threat of nuclear war served as justification for these tests; however, based upon recent statements by President Obama [1], a strong argument exists today for identifying the degree of radiation shielding provided by each vehicle system currently in the US Army inventory.

Experimental Approach

Experimentation with residual radiation shielding typically employed Cobalt-60, which simulated the gamma emissions anticipated from nuclear fallout [8]. From measurements taken both inside and outside a vehicle, a calculation of the GPF could be made. Other experiments investigated how a particular vehicle's armor, when mounted with radiation detectors, would attenuate incident radiation, thereby producing erroneous detector responses [9]. Despite the variety of conducted experiments, the US Army quickly realized the most difficult radiation environment to simulate and operate within came from the initial radiation emitted by a nuclear weapon.

Most of the experimental research on initial radiation effects was conducted at either the Army Pulse Radiation Facility (APRF), located at Aberdeen Proving Grounds, Maryland, or near the White Sands Missile Range in New Mexico. Both sites offered

open-air nuclear reactors capable of projecting high-energy neutrons toward stationary targets. The APRF boasted a nuclear reactor capable of rising out of the ground to a maximum height of 14 meters above the surface, a configuration which offered the best possible simulation of an above ground nuclear detonation [4]. However, due to funding limitations, the reactors at Aberdeen and White Sands were decommissioned for many years, although efforts in recent years have returned this capability to White Sands [2].

Computational Approach

Methodology (Deterministic versus Stochastic)

Fortunately, the US Army also researched and developed computational methods to answer information gaps related to radiation transport. The impetus behind this approach began in the 1950's and 1960's, prior to the advent of computer technology. In response to the threat of nuclear war posed by the USSR, the Office of Civil Defense sought to determine the extent to which certain structures protected Americans from radioactive fallout expected from Soviet nuclear weapons. The first attempt resulted in the "Engineering Method," which the National Bureau of Standards developed to provide semi-empirical estimates of gamma ray transport through simple geometries and materials [10]. Understandably, this method lacked the capability to analyze complex shapes and materials; however, these limitations were lifted by the eventual emergence of computer technology.

One early computer-based approach involved discrete ordinates transport (DOT) codes. This method utilized deterministic methods to solve the radiation transport problem in terms of the average particle, which can provide different solutions than those

achieved through stochastic methods. This discrepancy is due to DOT reliance on "phase space" approximations within the integro-differential transport equation. Phase spaces represent the six-dimensional properties of a particle, including its position on the x,y,z axes and its component momentum in each direction. For example, phase spaces can be represented using an equation such as

$$P = (\hat{r}, \Omega, E)\,, \tag{1.4}$$

which symbolizes the six independent variables used to determine the classical description of particle motion. In this case, $\hat{r}$ is the vector of movement, Ω is the solid angular component (θ,φ), and E represents the energy of the particle. This facilitates a calculation of particle track length density, ρ_L, at a specific time via

$$\rho_L = \mathrm{v}N(\hat{r}, \Omega, E, t)\Delta P \Delta t\,, \tag{1.5}$$

where $N(\hat{r}, \Omega, E, t)$ represents the particle density function. From Equation (1.5), a determination of particle flux may be reached using the relationship

$$\phi(\hat{r}, \Omega, E, t) = \mathrm{v}N(\hat{r}, \Omega, E, t)\,. \tag{1.6}$$

For DOT calculations, this definition is applied to solve the neutron Boltzmann transport equation for an arbitrary volume of a partial phase space $\Delta P = (\Delta\hat{r}, \Delta\Omega, \Delta E)$ during Δt. Essentially, the solution is derived computationally by tracking the particle count over time using an integro-differential transport equation, which accounts for all particle scattering and absorption events:

$$[\nabla\Omega + \Sigma(\hat{r},E)]\phi(\hat{r},\Omega,E) =$$
$$= \int_0^\infty dE' \int_{4\pi} d\Omega' \Sigma_s \phi(\hat{r},\Omega,E') + \frac{D(E)}{4\pi}\int_0^\infty dE' \int_{4\pi} d\Omega' \nu(E')\Sigma_f(\hat{r},E')\phi(\hat{r},\Omega,E') + , \tag{1.7}$$
$$+Q(\hat{r},\Omega,E')$$

where

$\phi(\hat{r},\Omega,E) = \int_0^\infty \phi(\hat{r},\Omega,E,t)dt$, the particle flux integrated over all time

D(E) is the energy distribution range of the neutrons

Σ is the macroscopic cross section for neutrons, and

Q is the steady-state source distribution.

Early computers also enabled employment of Monte Carlo calculations, a stochastic approach to radiation transport first realized by von Neumann and Ulam in the 1950's, which is still in use today. In general, the Monte Carlo technique offers a numerical solution to problems involving an object's interactions with other objects or its environment [11]. This is accomplished by conducting a separate random sampling event for each microscopic exchange between objects involved in the larger problem. Similar to rolling dice at a casino, hence the name Monte Carlo, each final outcome is randomly determined from the statistical chances of all possible outcomes. Each individual particle track, or random walk, is known as a Markov Chain. After sufficient repetition of these Markov Chains, a realistic solution to the macroscopic problem is determined stochastically [12]. Therefore, although the probability distribution function (PDF) for each particle remains unknown, the stochastically-determined sample mean and variance become increasingly representative of the unknown PDF as the number of particle tallies increases. This positive relationship between simulated particle number and solution

veracity demonstrates the dependence of the Monte Carlo method on vast computational resources. In other words, Monte Carlo techniques utilize repetition and random sampling at interaction sites to solve for the integral transport equation, thereby providing a solution to Equation (1.7) as $\phi(\mathbf{r},E)$ without the differential or limit calculations required by deterministic methods.

Therefore, both the Monte Carlo and DOT methods provide solutions to two forms of the same equation, which are fundamentally equivalent. Despite this, a flaw inherent within the DOT solution exists, one which stems from the reliance of integro-differential equation on numerical approximations [12]. Numerically derived solutions to Equation (1.7) will always converge *toward* the real answer; however, they will never attain the level of accuracy achieved by Monte Carlo methods. To this day, the Monte Carlo technique of random sampling forms the fundamental pillar for nearly all computer-modeled radiation transport calculations.

Computational Codes

The three primary computer codes designed over the years by the US National Laboratories to model radiation interactions with matter consist of the Vehicle Code System (VCS), the Monte Carlo Adjoint SHielding (MASH), and the Monte Carlo n-Particle (MCNP) code.

Of the three, the oldest and still most widely utilized radiation transport code is MCNP. First created at Los Alamos National Laboratory (LANL) in 1957, the code simulated neutral particle transport to enable predictions of radiation flux due to shielding and distance. It provides extremely accurate modeling for a variety of particle types, and previous versions of MCNP were repeatedly validated using both simple and complex

geometries [12, 13]. Much greater discussion and explanation of the current capabilities of MCNP will occur within the next chapter of this document; however, it is important to note that MCNP consistently offered, throughout its years of development and refinement, the most comprehensive databases of cross-sections and advanced Monte Carlo calculations available. This code was originally validated against a benchmark test using a two-meter iron box and was trusted for RPF evaluation of numerous military vehicles, including the M60 and M1 Abrams main battle tank.

During the early 1970's, Oak Ridge National Laboratory (ORNL) began designing a different code, one which incorporated both Monte Carlo transport and DOT calculations. This effort produced the first generation of the Vehicle Code System (VCS), which was designed specifically to replicate radiation transport to a vehicle or structure. Based upon the separation distances involved, this typically simplified into a point source to point detector calculation. Within the code, the radiation transport was divided into two parts: a DOT portion and a Monte Carlo portion [7]. The DOT code solved the Boltzmann Equation deterministically for the average flux created at the target location by the weapon burst. A special Monte Carlo code then provided an importance function at the surface of the vehicle, which offered an adjoint measurement of the probability that particles on the vehicle surface would reach a crew member. Folded together, these two calculations offered an estimate of flux and dose rate, which allowed assessments of a vehicle RPF [13].

In the 1980's ORNL also developed the MASH code to succeed VCS. It enabled the modeling of mixed neutron and gamma-ray environments, such as those found within seconds to minutes after a nuclear detonation. The code enabled RPF assignments for

military vehicles, buildings, trenches, and other structures [14]. Similar to VCS, it accomplished this through coupling a forward discrete ordinate air-over-ground transport calculation with an adjoint Monte Carlo treatment of the shielding geometry [15]. Based upon the neutron and/or gamma-ray source, the DOT calculation determined the flux incident on a given surface of the shielding geometry. Once determined, the Monte Carlo calculation determined the effectiveness of the particle flux in creating a response from the detector inside the shielding geometry. Based upon that detector response, a "dose importance" could be determined from the coupled surface flux. The flux and dose importance were then folded together to provide an effective dose response. The coupling code surpassed VCS by determining the dose response as a function of the shielding geometry orientation relative to the source type, distance, and energy [15]. This provided a much more useful calculation of flux and dose rate than previously attainable through the VCS.

Despite these improvements, decades of competition between the three codes eventually resulted in the determination by the DTIC that MCNP proved superior to both VCS and MASH, offering the best overall estimation of radiation transport possible [13, 16]. MCNP6, the latest and most advanced version of MCNP to date, is already experimentally verified and validated for a wide variety of intermediate and high-energy particles [17, 18].

Research Focus

To address the US Army's lack of vehicle RPF information, MCNP6 must first undergo verification and validation for the task, a mission championed by DTRA and

USANCA. To accomplish this objective, however, experimental and computational methods must both be applied to the same problems, thereby facilitating side-by-side comparisons of the results. Representing the first step in this effort, the research described herein will attempt to verify and validate MNCP6 results for just one aspect of RPF evaluations: modeling neutron transport and NPF assessments for simplified geometries and materials. Specifically, this research utilizes a hollow steel box with 61 cm sides and walls 2.51 cm thick, which simulates a geometrically simplified military vehicle. In addition to providing a quantifiable assessment of MCNP6 estimates of NPF, this research will also establish a scientific methodology for replicating and expanding these efforts to eventually validate MCNP6 for RPF assessment of military vehicles.

Implications

Due to the growing nuclear threat from nation-states such as North Korea and Iran, as well as the persistent danger of terrorist groups like Al Qaeda obtaining a nuclear device, the US Army must plan for scenarios wherein its soldiers operate and fight in radiological environments. Consequently, vehicle crews exposed to high-energy neutrons and gamma rays, such as those documented within seconds to minutes following a nuclear detonation, must understand the degree of radiation protection provided by their vehicles. Such knowledge will enable US Army leaders to optimally employ combat vehicles systems in relation to a radiation source, thereby maximizing the odds of mission accomplishment and crew survivability. This represents the ultimate objective behind research to provide accurate RPF assessments for all US Army vehicles.

II. Theory

Chapter Overview

This chapter describes the theoretical background of neutron transport supporting this research, as well as provides a description of all computational software and radiation detection equipment relevant to the experiment. A detailed explanation of all the physics behind each component or system is not provided; however, the reader is encouraged to utilize the resources documented within this manuscript to answer any theoretical questions that may remain unresolved at the conclusion of this thesis.

Neutron Interactions and Kinematics

Due to their charge neutrality, neutrons fail to produce direct ionization events when traveling through media. Consequently, these particles do not interact with matter via the Coulomb force, but instead deposit their energy discretely via collisions with other particles or atomic nuclei [19]. Such collisions can result in either absorption or scattering events.

An absorption event occurs when an incident neutron and all its kinetic energy is captured by a target atom, thereby producing a compound nucleus in an excited state. The likelihood of this occurrence is governed by the isotope's absorption cross section. Cross sections are used to quantify the probability that an incident neutron of specific energy will interact with a target nucleus and are expressed in units of barns, which is equal to 10^{-24} cm^2. The likelihood of such reactions occurring generally increases as neutrons lose kinetic energy, following a 1/v dependence for reaction cross section across

most energies [20]. Consequently, absorption events are most likely for neutrons in the thermal energy range. Following a neutron capture, the excitation energy within the compound nucleus typically results in a (n,α), (n,p), or fission reaction, all of which are important in neutron detection. The specific absorption reaction and fission products germane to this research will be addressed in the next section.

Neutron scattering events consist of either inelastic or elastic scattering. Inelastic scattering usually imparts a small degree of the incident neutron's kinetic energy to the target, thereby leaving the nucleus in an excited state. The deposited energy is subsequently released by the nucleus as a gamma emission, so *kinetic* energy is not conserved. Inelastic scatterings account for a negligible percentage of neutron reactions within a moderator and, therefore, are of much less importance within the scope of this research. Conversely, elastic scattering results when a neutron collides with an atomic nucleus and imparts a portion of its kinetic energy to the object, thereby decreasing its own kinetic energy in the process. This event conserves kinetic energy and represents the dominant reaction type between neutrons and materials used to moderate, or slow down, high-energy neutrons. As in neutron absorption, the likelihood of neutron scattering is expressed in terms of cross sections. Consequently, materials with large cross sections for high-energy neutrons are commonly employed to reduce neutrons to thermal energy ranges, thereby increasing the odds of measurable interactions, including neutron absorption. To better understand the kinematics of elastic scattering, the following equations governing neutron energy and direction are explained. These equations form the foundation of the stochastic calculations leveraged by MCNP during computational runs.

Each time a neutron collides with an atomic nucleus, a ratio exists between the final neutron energy, E_f, and the initial neutron energy, E_i. According to the classical laws of conservation of energy and momentum, this can be expressed mathematically as

$$\frac{E_f}{E_i} = \frac{A^2 + 1 + 2A\cos(\theta)}{(A+1)^2}, \tag{2.1}$$

where A is equal to the mass of the nucleus struck and θ is the scattering angle of the incident neutron. Therefore, in the absence of scattering (i.e. $\theta = 0^o$), Equation (2.1) provides an energy ratio of 1, while a head-on collision (i.e. $\theta = 180^o$) results in a maximum energy loss calculated by

$$\frac{E_f}{E_i} = \frac{(A-1)^2}{(A+1)^2}. \tag{2.2}$$

Additionally, the calculated angles from this interaction must be modified to determine the final scattering direction. This involves a shift from the incident neutron coordinate system, one relative to the approach of the neutron, back to the laboratory coordinate system, which represents the real-world angles. This adjustment involves utilizing the conversion

$$\cos(\varphi) = \sqrt{\frac{1-\cos(\theta)}{2}}. \tag{2.3}$$

By substituting Equation (2.3) into Equation (2.1), a final calculation for the scattered neutron energy, E_f, within the laboratory coordinate system can be generated with

$$E_f = \frac{4A\cos^2(\varphi)E_i}{(1+A)^2}. \tag{2.4}$$

Based upon Equation (2.4), the maximum amount of kinetic energy deposited by a neutron into a target nucleus results from a head-on collision ($\varphi = 0^o$), as demonstrated by

$$E_{f,\max} = \frac{4A}{(1+A)^2} E_i. \tag{2.5}$$

Therefore, the maximum energy transferrable from an incident neutron to its target nuclei depends largely upon the value of *A* for a given material. Using the relationship described in Equation (2.5), a hydrogen atom, ^1H with *A*=1, allows a neutron to potentially transfer all of its kinetic energy to the nuclei, thereby potentially reducing the neutron to thermal energy in a single collision.

This explains why neutron moderators are typically constructed from low-*A* materials, such as polyethylene (C_2H_4); neutrons incident upon such materials possess a higher probability of depositing more of their kinetic energy in fewer collisions, which more quickly reduces the neutrons to thermal energy levels. This concept is central to the functioning of the neutron detector used for this experiment, which is described in the following section.

Bonner Sphere Spectrometer

In 1960, the multisphere spectrometer, or Bonner Sphere Spectrometer (BSS), was first introduced to measure neutron spectra [20]. The system typically detects neutrons using a small (4mm x 4mm) LiI(Eu) scintillator crystal, although He^3 tubes are also commonly used. The ^6Li within the crystal offers a relatively large absorption cross

section of 838 barns to thermal neutrons [19], and any captured neutrons produce a large, measurable light output. The result of each reaction produces a total energy of 4.78 MeV, illustrated as

$$ {}^{1}_{0}\mathrm{n} + {}^{6}_{3}\mathrm{Li} \rightarrow {}^{3}_{1}\mathrm{H}\ (2.728\ \mathrm{MeV}) + {}^{4}_{2}\mathrm{He}\ (2.055\ \mathrm{MeV})\,. \tag{2.6} $$

Since the effectiveness of LiI(Eu) is limited to detecting only thermal neutrons, the crystal scintillator is designed to operate interchangeably within the center of a variety of polyethylene spheres, typically ranging in diameter from two to twelve inches. This ability to easily exchange shielding depths allows the BSS to measure neutron flux across a wide range of energies using the principle of particle moderation.

Particle Moderation

The number of neutrons, *dN*, traversing a given region of space, *dA*, is known as neutron flux, $\phi(r,t)$, which has dimensions of length and time [21] and is usually described in units of neutrons/cm^{-2}-sec^{-1}. Therefore, the neutron reaction rate density, ρ_n, for any reaction type can be calculated by multiplying the neutron flux by the cross section for that specific material and reaction type [19]. This is shown as

$$ \rho_n = \Sigma\phi(r,t)\,, \tag{2.7} $$

where

Σ represents the macroscopic cross section for a specific neutron interaction, and

$\phi(r,t)$ is the flux at any time, *t*.

Neutrons undergoing scattering events within a moderator lose energy until they are either absorbed or escape the moderator. Polyethylene is used in BSS moderator

spheres due to its large ratio of scattering to absorption cross sections. Such a ratio maximizes the possible number of incident neutrons that may become thermalized before reaching the LiI(Eu) crystal [22], a concept demonstrated in Figure 1.

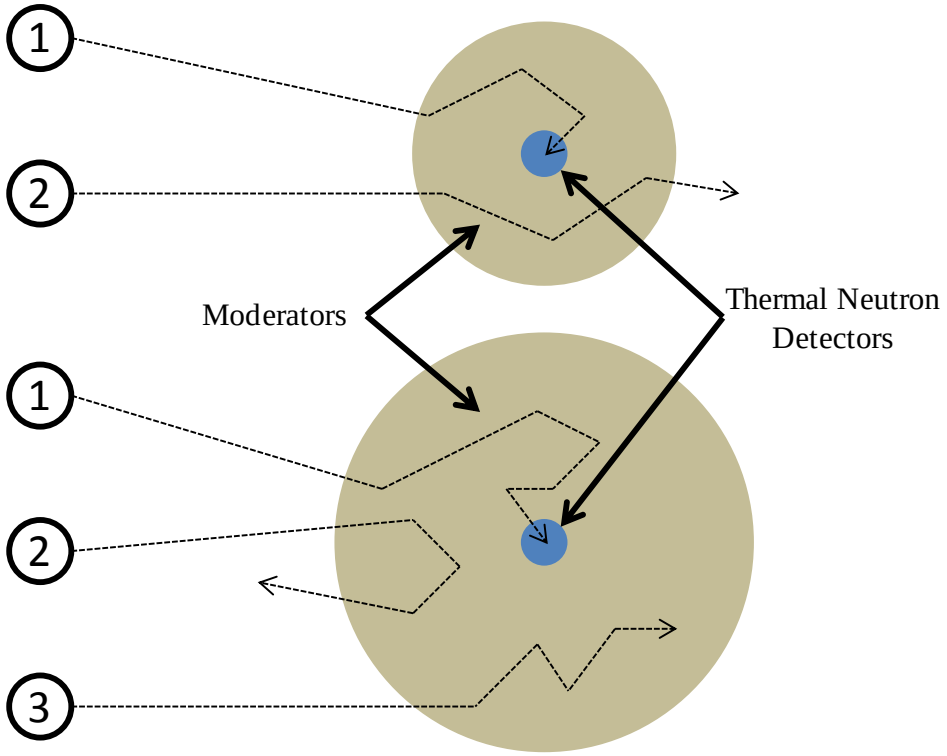

Figure 1. Schematic of possible neutron histories within two Bonner spheres of different sizes. Track 1 represents neutrons moderated by the polyethylene and detected by the crystal, Track 2 represents partially-moderated neutrons that escape the detector, and Track 3 shows how neutrons may be parasitically captured within the moderator material. Larger spheres tend to enhance the frequency of Track 3, while reducing the frequency of Track 2 [21]. (Adapted from Knoll, pg. 554)

By interchanging the polyethylene spheres between measurements of flux, the crystal scintillator records the neutron counts for that specific depth, or radius, of moderator material. This creates a characteristic response function for each sphere, which is a measure of detector efficiency as a function of incident neutron energy [23]. As the sphere radius increases, the energy range of peak efficiency for the response

functions shifts from lower to higher neutron energy levels because only neutrons of increasing energy can reach the detector. The BSS response functions, also known as a response matrix, illustrate the principle of particle moderation.

The shift in peak efficiency amongst the BSS response functions also becomes important when determining the optimal number of spheres to employ for a given experiment. The traditional number is as many spheres as possible, provided the shapes of their response functions differ sufficiently [24]. Of note, the BSS suffers from relatively poor detector resolution across intermediate energy ranges (10 eV – 500 KeV) due to the lack of strong structures across that region of the response matrix [24].

Solving for Neutron Flux

The BSS response matrix is essential when solving for the neutron flux spectrum, as shown in Equations (2.8) and (2.9). Within an array of "i" elements, the individual detector responses, or counts, can be expressed as a homogeneous Fredholm equation [22],

$$B_j = \int_0^\infty \phi(E) R_j(E) dE \,, \tag{2.8}$$

where,

B_j is number of counts for the j-th detector, j=(1,i)

$\phi(E)$ is the neutron flux energy spectrum, and

$R_j(E)$ is the response function of the j-th detector.

Once these count values are known for a set of "n" detectors, Equation (2.8) can be rewritten as the following equation

$$B_j = \sum_{g=1}^{n} \phi_g R_{j,g} \Delta E_g \ , \tag{2.9}$$

where,

ϕ_g represents the differential neutron flux for the g-th energy group,

$R_{j,g}$ is the response of the j-th detector to the g-th energy group, and

ΔE_g is the energy bin width of the g-th group.

Therefore, the incident neutron energy spectrum is determined by solving for $\phi(E)$ from Equation (2.9), a process known as spectral deconvolution or unfolding. The software utilized throughout this research to unfold neutron spectra is described briefly in the next section.

MAXED

The MAXED Few Channel software was authored specifically for the purposes of unfolding neutron spectra from Bonner Sphere data and uses the principle of maximum entropy in the deconvolution of multisphere spectroscopy data [27]. The maximum entropy principle suggests that, for problems where multiple probability distribution solutions exist, the best solution is the one with the largest degree of entropy, or uncertainty in a random variable. This provides MAXED a method of inference which is both consistent and unbiased [23].

Before spectrum deconvolution begins, however, some information must already exist about the neutron source. Whether derived by calculation, computation, or experimentation, a default spectrum, or *a priori*, is required to support the deconvolution

calculation [23]. The MAXED program uses this default spectrum as a baseline for the generated answer, even if the provided spectrum is little more than conjecture. To accomplish this, the program evaluates a number of solutions which all match the measured response functions, and the solution most closely matching the default spectrum is selected. A more robust explanation of the algorithms and input parameters used by MAXED for the purposes of this experiment is included later within this paper.

MCNP6

MCNP6 is the latest version of MCNP produced by LANL. The following discussion is intended only as an overview of the tremendous capabilities inherent within this computational tool. Information not provided within this paper on the use of first principles by MCNP6 for modeling radiation transport is left to the explanations provided within the MCNP6 User's Manual.

MCNP6 includes the recent merger of MCNP5 and MCNPX and is capable of modeling three-dimensional geometries, the transport of 36 continuous-energy particle types, reactor fuel burn-up, and delayed-gamma emissions [18]. This latest version also boasts new tally, source, and variance reduction options, as well as an improved plotting capability [25]. Essentially, MCNP6 represents the most comprehensive update to the MCNP code in recent decades, a fact which makes this version, once sufficiently validated, attractive to the US Army for solving the problem of vehicle RPF assessment.

Similar to previous versions of MCNP, MCNP6 operates from a user-written input file, which contains all the necessary information to enable the program to model any given experiment. First among this information is the definition of the geometric

spaces within the problem, known as cells, and how they exist within or among one another. Cells may be designed simplistically, such as a set of cubical boxes, or in as detailed a manner as a nuclear reactor, complete with fuel and control rods. Along with cell positioning, an assignment of material density is also possible.

MCNP6 input parameters also govern the material composition for all cells, allowing the user to define any medium by its atomic composition. These data affect neutron transport through calculations of mean free path and reaction rate densities, as discussed earlier. Additionally, the atomic structure of each material greatly alters the calculations of particle scattering angle, absorption, and energy deposition. The radiation source may also be defined therein, including its shape, location, radiation type, and emitted particle energies. This includes manipulation of initial particle direction and energy spectrum. Lastly, MCNP6 allows the user to tailor the results, incorporating directions for how and what specific data the code displays.

MCNP6 also offers a number of variance reduction features built into the program. These represent established techniques and fall under the broad categories of population control, modified sampling methods, and partially deterministic methods [26]. For a complete definition of each technique, readers are encouraged to consult the MCNP6 User's Manual; however, each feature is designed to allow users to obtain more precise and computationally efficient results. Nevertheless, despite these hard-coded variance reduction techniques, other user-implemented forms of variance reduction may also be employed by users.

For example, one technique to reduce variance from an isotropic point source at great distance from a detector is to funnel the emitted particles into a directional cone

pointed toward the detector. This enables a significantly greater count rate per particle created, thereby driving down the variance of the computation. In so doing, however, the number of radiation quanta, *S*, emitted by the source in the direction of the detector becomes artificially inflated and an adjustment must be made to the measured count number, N [21]. The equation governing this relationship is

$$N = S\frac{\Omega}{4\pi}\varepsilon_i \tag{2.10}$$

where

Ω is the solid angle subtended by the column, and

ε_i is the intrinsic efficiency of the detector.

For the purposes of MCNP6, ε_i may be assumed to equal one; however, a calculation of the solid angle is nevertheless required to provide an accurate value of *N*. Figure 2 provides an illustration of the solid angle for a detector of area, A, at a distance, d, from the source.

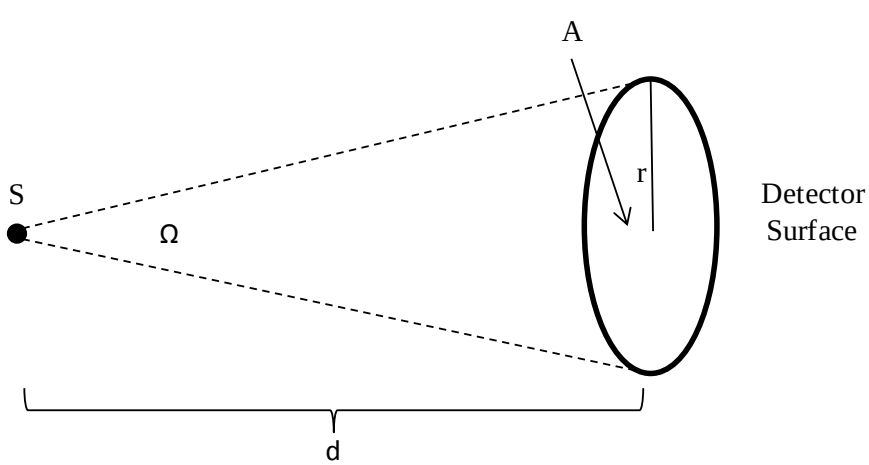

Figure 2. An illustration of the relationship between the solid angle, Ω, and the detector surface area, A, sublimated by the source as a function of distance, d [22]. (Adapted from Knoll, pg. 120)

When the distance between the source and detector greatly surpasses the radius of the detector area (i.e. d >> r), the calculation of the solid angle reduces to

$$\Omega = \frac{A}{d^2}. \tag{2.11}$$

As such, the adjusted calculation for the number of detected particles becomes

$$N = S\frac{A}{d^2}\frac{1}{4\pi}. \tag{2.12}$$

Therefore, the use of Equation (2.12) provides the necessary adjustment to the number of detected particles whenever an isotropic source is modeled as a collimated conical source for the purposes of variance reduction. This formula may be extended to calculations of particle flux, as well, since flux is simply a particle count per unit area. Not surprisingly, MCNP6 can automatically perform the same calculations from Equations (2.10)-(2.12). To do so, the user specifies that request on the source definition card by assigning the particle weight to the inverse of the solid angle, or "WGT=1/fsa2."

Summary

This chapter provided the theoretical basis and relevant background information on the tools and techniques employed throughout this research. Greater information on the specific application of these tools is provided in later chapters, as well as relevant portions of theory.

III. Computational Replication of Benchmark Experiment

Chapter Overview

The exercises described in this chapter were conducted to familiarize the researcher with the two primary computational tools leveraged later in this research: MCNP6 and MAXED. Specifically, modeling and unfolding benchmark spectra facilitated both a refinement of the computational methodologies and a validation of these tools for later experimentation. Consequently, however, the conclusions drawn from these exercises, such as assessments of NPF, are not completed with the same degree of academic rigor as the results presented later in this work. Instead, these values represent only estimations to justify continued use of MCNP6 and MAXED for later calculations of NPF conducted within this research.

Benchmark Experiment

In 1984, an experiment sponsored by the US Army Combat Systems Test Activity sought to determine the effects of borated polyethylene (BP) lining on neutron and gamma ray penetration through iron. Entitled "Radiation Protection-Factor Measurements of a Lined Iron Box in Simulated Fission and Fusion Tactical Nuclear Environments," the author, Craig R. Heimbach, ultimately determined that different layers of BP shielding provided different RPF values depending on the source of the incident neutrons, either from fission or fusion [28]. More importantly, the author also intended his experimental results to provide a benchmark for comparison against future computational results from radiation transport codes, as the excerpt below explains.

> The shield chosen for the study was an iron box with liners of various thicknesses of borated polyethylene. Such a box has already been used at the APRF reactor to measure radiation protection factors for fission neutrons. This box has the advantage of providing results directly applicable to armored vehicles, and is also simple enough in shape to serve as a benchmark against which vehicle protection factor computer codes can be tested without making approximations in the geometry of the model. [28]

Using this historical data, an attempt was made to validate estimates of neutron flux and NPF provided from MCNP6 calculations. In doing so, the geometry, neutron energy, and materials were modeled in MCNP6, based upon those described in the experiment. The results of this computation are presented herein, as well as their comparison against the results collected experimentally in 1984.

Experimental Setup, 1984

Measurements of neutron flux, kerma, and RPF were recorded in April and May of 1984 at the Etablissement Technique Central de l'Armement (ETCA), in France, utilizing a hollow iron box with outer edges of 61 cm and a wall thickness of 2.5 cm. A deuterium–tritium (D-T) neutron accelerator served as the source for all incident particles, producing a beam of mono-energetic neutrons of 14.1 MeV. This reaction process is illustrated as

$$ {}^{2}_{1}\mathrm{D} + {}^{3}_{1}\mathrm{T} = {}^{4}_{2}\mathrm{He} + {}^{1}_{0}\mathrm{n}\ (14.064\ \mathrm{MeV})\,. \tag{3.1} $$

The neutron accelerator was situated atop a large tower, raised 14 meters above the ground to replicate the experimental conditions used previously at the APRF. The iron box was then positioned two-meters off the ground on a raised steel platform at a horizontal distance of 402 meters from the neutron source. During each measurement,

the accelerator emitted a maximum of 5.0×10^{11} neutrons per second, with approximately 2.0×10^{8} neutrons produced per detector count. These high-energy neutrons were emitted as a horizontal beam directed towards the iron box, which left a vertical gap of 12 meters between the source beam and detector. Consequently, due to the distances involved, the accelerator behaved much more like an isotropic source than that of a beam. Figure 3 provides a simplified illustration of the experimental configuration used in 1984.

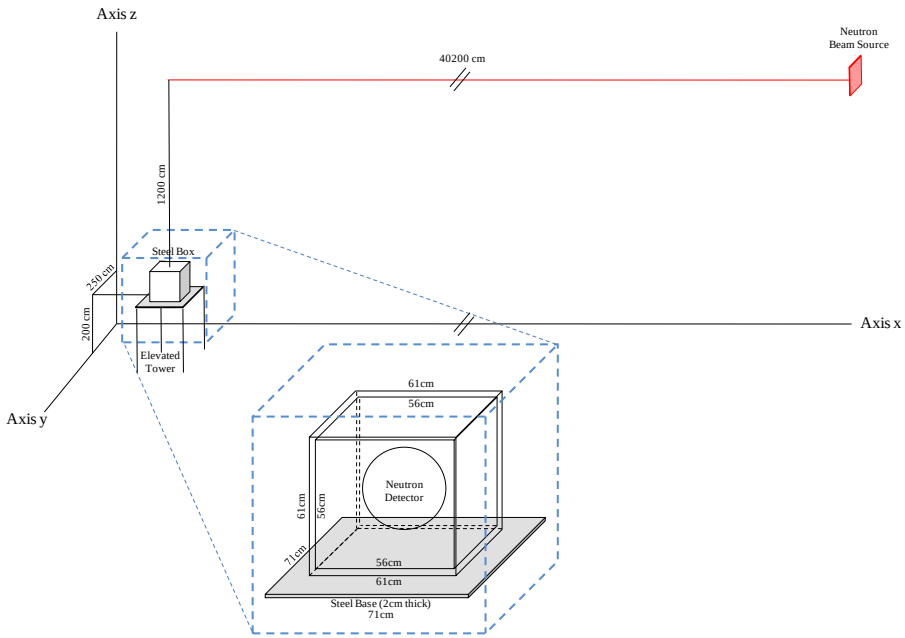

Figure 3. Graphic depiction of the experimental setup employed in 1984 at the ETCA. A D-T accelerator directed a beam of 14 MeV neutrons approximately 12 meters above a stationary iron box target. Within the target, a set of neutron detectors was utilized to measure the neutron flux within the box, which was later compared to free-field measurements taken simultaneously outside the box.

Neutron Detector

To measure the neutron flux and spectrum for this experiment, Heimbach employed a Bonner Sphere Spectrometer (BSS), as described earlier. Measurements were recorded both within the iron box and in its absence, which constituted the "free-

field" measurement. Additionally, measurements were taken using various thicknesses of polyethylene; however, these results were not incorporated into this validation of MCNP6.

Source Monitor

A source monitor records the count rate of particles emitted by the source during each measurement. In 1984, a boron-lined proportional counter reportedly served as the source monitor for the D-T accelerator used at the ETCA. Although unspecified in the literature, the type employed was assumed to be a ^{3}He proportional counter, which interacts with neutrons through a ^{3}He (n,p) reaction. Commonly utilized in slow neutron spectroscopy, the ^{3}He proportional counter suffers from very low cross sections for neutron interaction above 764 keV. Additionally, at those energy levels the chances increase substantially that other competing reactions may also take place, thereby negatively affecting data collection. These factors severely limit the efficiency of ^{3}He detector for fast-neutron spectroscopy; however, they can be overcome. One common technique involves exposing the proportional counter to a known high-energy neutron spectrum and calculating a function to normalize neutron counts for energy regions of low sensitivity. While this practice can significantly improve neutron detection across a wide energy spectrum, the published experimental design provided no information on whether, or how, such a technique was employed at the ETCA in 1984.

Miscellaneous Detectors

Additionally, a 16-liter tissue-equivalent ion chamber and a gamma-ray ion chamber were among the other types of detectors leveraged during the 1984 experiment. The purpose of the tissue-equivalent ion chamber was to measure the total kerma per unit

of time. Using the neutron count rate data from the proportional counter, this enabled a calculation of dose-rate per source neutron. The device was constructed out of tissue-equivalent plastic and housed a tissue-equivalent gas to enable a more precise determination of total tissue kerma from both neutrons and gamma rays. The gamma-ray ion chamber utilized high pressure argon gas, which enabled measurements of the dose rate due to source neutrons, as well; however, this ion chamber also detected the secondary gamma rays produced from the high-energy neutron beam.

Simulation of the Benchmark Experiment

MCNP6 Input Cards and Geometry

In order to recreate the benchmark experiment of 1984, two input cards were created for MCNP6, which are included in Appendix A. The first input file models an iron box, identical in dimensions to that reported in the benchmark experiment. The box is positioned on a 2 cm thick steel plate, which serves to replicate the top of the metal tower upon which it rested. As such, these objects are suspended two meters above the bottom of the problem, below which all neutrons are considered escaped particles. With walls 2.5 cm thick, the box itself is hollow; however, centered within the box cavity is a polyethylene sphere with a radius of 15.25 cm, which serves two purposes for this experiment. First, the size and material type replicate the largest sphere of the BSS detector. Secondly, by utilizing the F4 Tally to measure neutron flux throughout a given volume, the sphere serves as the detector for the purposes of this computational experiment.

The source is modeled at a distance of 402 meters, as reported in the experimental literature. However, instead of placing an isotropic source at a height of 14 meters, the source is instead placed level with the target iron box and replicated as a beam. This is done for variance reduction purposes due to the immense distance separating the source and iron box in comparison to the detector size. Consequently, in order to properly adjust the measured detector flux, the solid angle was calculated using Equation (2.11):

$$\Omega = \frac{A}{d^2} = 4.521\mathrm{E}^{-7} \tag{3.2}$$

The final geometry for the computational model measuring neutron flux within the iron box is shown below:

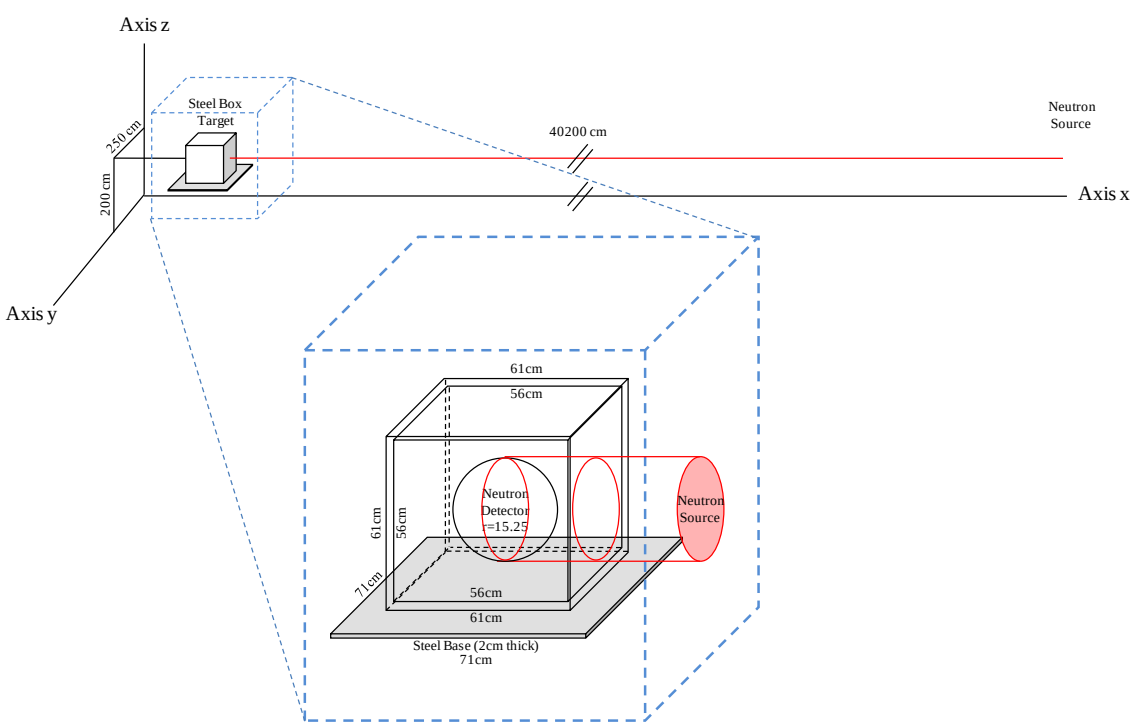

Figure 4. Diagram of the modeled dimensions used by MCNP6 to calculate the neutron flux within the iron box at a distance of 402 meters from the source.

Similarly, a second input card was written to model and measure the free-field neutron spectrum for comparison against the field measured within the iron box. In this calculation, the iron box was removed completely, leaving only air between the 14.1 MeV source neutron beam and the polyethylene sphere of 15.25 cm radius. A consistent radius was selected to replicate both the solid angle and the size of the BSS detector used in the model of the iron box. This provided a comparable perpendicular detector area of 730.62 cm^2 and an identical value for the solid angle, Ω. The steel plate beneath the sphere remained, which again represented the top of the tower upon which the detector rested. Figure 5 provides a diagram of the detector configuration used to model the free-field neutron flux. The MCNP6 solutions to the neutron flux spectra within the iron box and for the free-field are provided in Appendix B.

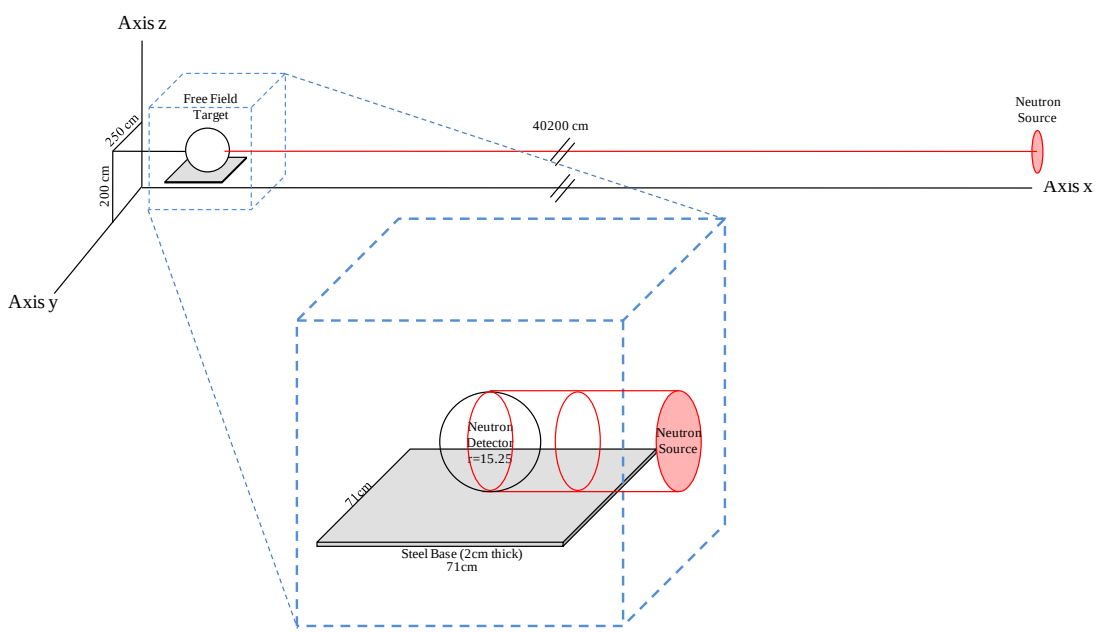

Figure 5. A diagram of the MCNP6 model executed for a measurement of neutron flux in a free-field environment. The iron box was removed and the shape of the incident neutron beam was altered to enable this calculation.

MAXED Software Employment

Additionally, MAXED software was utilized to unfold the measurements recorded via BSS detection in 1984. The published data were replicated as input files for the MAXED program, including the detector count rates (*CR*), the provided *a priori* spectrum, and the published response functions for each sphere used to unfold the spectra. Of note, certain data required for the proper functioning of MAXED were absent from the 1984 report, including the fractional (CR_{Frac}) and absolute (CR_{Abs}) uncertainties for each detector configuration, as well as the *R*-value, which includes the uncertainty of the measured data due to other causes. In place of these omitted data, sample values presented in the MAXED User's Manual were placed in their stead to facilitate spectrum deconvolution.

Based upon the published data and assumed uncertainties, MAXED initially returned solutions failing to converge. Interestingly, the MAXED manual made no mention of a cadmium-lined shell as part of the Bonner Sphere assembly, and once the data from the shell containing the cadmium lining were removed from the MAXED input file, both spectra converged to values far more consistent with those reported in the experiment. Tables 1 and 2 provide the values input into MAXED for spectra unfolding.

Table 1. Experimental data measured on 24 April 1984 and input into MAXED software for free field spectrum unfolding.

Detector	CR	CR_{Frac}	CR_{Abs}	R
Bare	2.12E-12	0.53	1.12E-14	2.9
2	4.32E-12	0.30	1.30E-14	2.0
3	6.69E-12	0.30	2.01E-14	2.0
5	8.65E-12	0.23	1.99E-14	1.2
8	7.17E-12	0.32	2.29E-14	1.3
10	5.44E-12	0.13	7.07E-15	1.3
12	4.06E-12	0.20	8.12E-15	1.6

Table 2. Experimental data measured on 26 April 1984 and input into MAXED software for iron box spectrum unfolding.

Detector	CR	CR_{Frac}	CR_{Abs}	R
Bare	7.49E-13	0.53	3.97E-15	2.9
2	4.07E-13	0.41	1.67E-15	4.0
3	2.37E-12	0.30	7.11E-15	2.0
5	5.21E-12	0.30	1.56E-14	2.0
8	9.08E-12	0.23	2.09E-14	1.2
10	7.18E-12	0.32	2.30E-14	1.3
12	4.88E-12	0.13	6.34E-15	1.3

MAXED utilizes a statistical χ^2 test to quantify the statistical significance of the solution spectrum. Statistical significance is obtained automatically if the χ^2 per degree of freedom (df) value falls below 1.0. In the case of the free-field spectra, the χ^2/df equaled 1.70. Nevertheless, the total computed χ^2-value of 10.2 for 6 degrees of freedom still falls below the critical value of 10.65 for an α=0.10, which indicates significance. Additionally, the χ^2/df returned by MAXED for the iron box spectrum was 0.81, thereby indicating significance. Based upon the results provided by MAXED, which are included in Appendix C, both solutions are statistically significant based upon the measured data and associated uncertainties.

Comparison of Results

The results produced by both MCNP6 and MAXED provide reasonable agreement with the data reported from the 1984 experiment. Specifically, the experimentally measured flux spectra resulted in a NPF of 1.41 for the iron box, whereas the same spectra modeled using MCNP6 returned a NPF of 1.35. This is a relative difference of less than 5%, which represents a significant agreement. Additionally,

MAXED unfolding of the free-field and box spectra produced flux values within 6% and 23%, respectively, relative to the experimental data from 1984. These results suggest that both MCNP6 and MAXED accurately replicate the neutron field present at the ETCA in 1984. These findings support the further use of both tools and the employed methodologies in future research.

Experimental Results

The benchmark experiment conducted in 1984 measured the neutron flux present inside and outside of an iron box exposed to a field of 14.1 MeV mono-energetic neutrons. The measurements obtained using a BSS in both environments were unfolded through unidentified methods and published as a function of $E\,\phi(E)$ with units of n/(cm^2-sn). These spectra are provided in Figure 6, but the task of replicating the reported results computationally becomes challenging without more detailed information on the methods of detection and spectra unfolding.

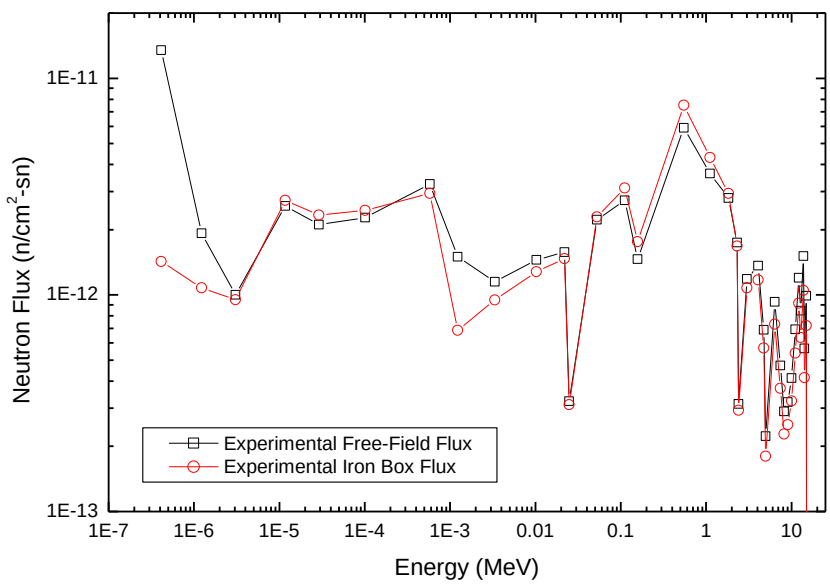

Figure 6. Plot of the experimentally determined neutron flux energy spectra in units of n/cm^2-source neutron. Data points extracted from Heimbach results [28].

Based upon this spectra comparison, Heimbach concluded that the iron box acted principally to reduce the thermal neutron flux in the experiment [28]. Beyond this analysis, a calculation of neutron protection factor (NPF) is also possible using these measurements. Specifically, an application of Equation (1.2) to the summed values of total neutron flux per energy bin can provide an estimate of the NPF. Of note, however, these values are only estimates of NPF and do not incorporate dose. This implies the effects on biological systems due to differences in neutron energy are ignored in this estimation; however, these contributions lessen if the compared values of NPF are based upon spectra possessing similar flux structure. This calculation produces an experimental NPF assessment of 1.41 for the steel box, which provides a critical point of comparison against the values of neutron flux determined computationally.

Computational Results

The simulated neutron flux measured both within the iron box, as well as for the free-field environment, was first adjusted based upon the solid angle for each of the two detectors. This calculation utilized Equation (2.11) and produced a solid angle, Ω, for both detectors of 4.521×10^{-7}, as explained above. The solid angle was then incorporated into Equation (2.12), thereby producing a conversion factor of 3.598×10^{-8} steridians, as shown in Equation (3.3).

$$N = S\frac{\Omega}{4\pi} = S(3.598\mathrm{E}^{-8}) \tag{3.3}$$

This conversion factor was multiplied against the values for the neutron flux, which produced the data provided in Figure 7.

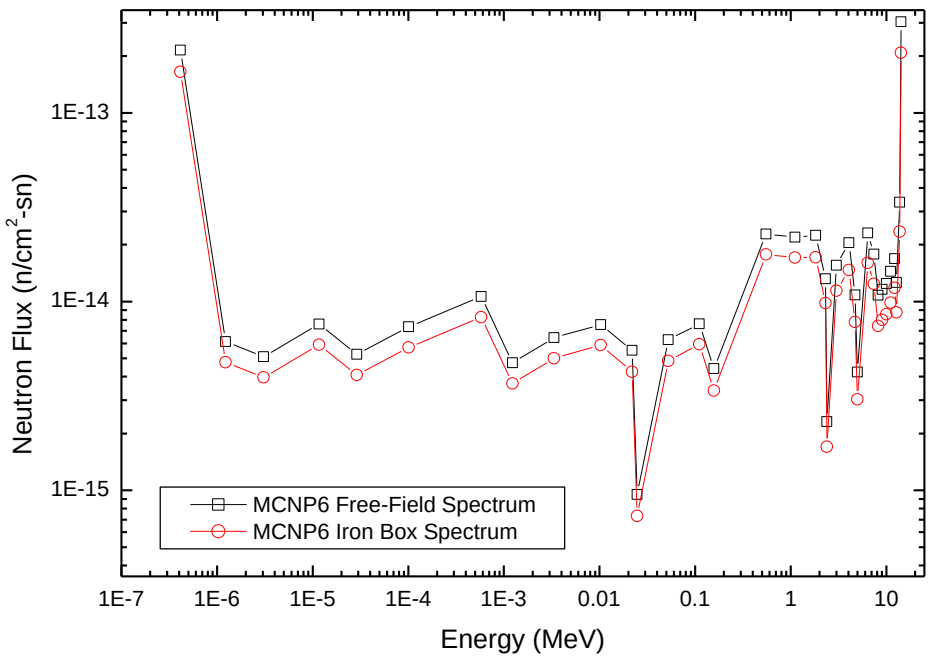

Figure 7. Computed neutron flux spectra from MCNP6, adjusted for the solid angle of each detector.

For each of the two computational experiments, the MCNP6 simulated a total emission of 100 million neutrons. This number of source particles drove the relative error for each energy bin below 1% for both the iron box and the free-field measurements. Both tests passed all ten statistical checks of tally fluctuation used by MCNP6 to ensure the experiments met the standard criteria expected for relative error, variance of the variance (VoV), figure of merit (FOM), and probability density function. As in the case of the experimental data, the ratio of neutron flux modeled within the box and for the free-field can be used to calculate an estimate of NPF, which produced a MCNP6 assessment of 1.35 for the NPF offered by the iron box.

Results Compared

Despite discrepancies between the experimental and computational values of flux per source neutron, a significant portion of the data appears in good agreement. For

example, although the values for neutron flux generated by MCNP6 differ by two orders of magnitude, the spectra within the free-field and iron box matched in many regards. Specifically, the oscillations of the spectra, which represent the neutron interactions with the polyethylene moderator, match almost exactly. When the respective spectra are scaled appropriately and overlapped, Figures 8 and 9 demonstrate the commonalities evident between the experimentally and computationally-derived flux spectra for both the iron box and free field.

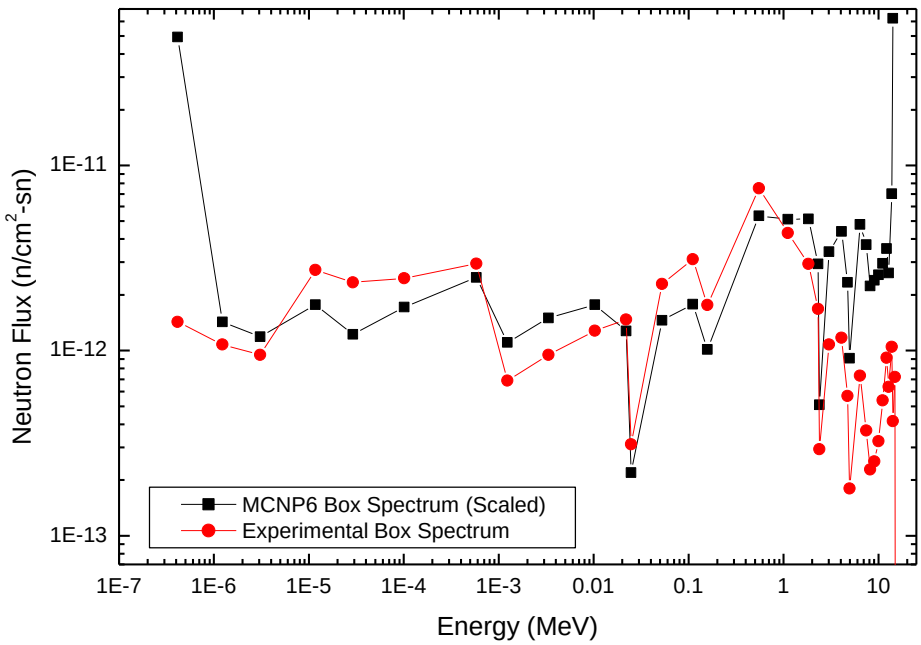

Figure 8. Experimental and computational neutron spectra from within the iron box, with the experimental data extracted from the Heimbach results [28]. Spectra were emitted by a 14.1 MeV neutron source at a distance of 402 meters and measured using polyethylene moderators.

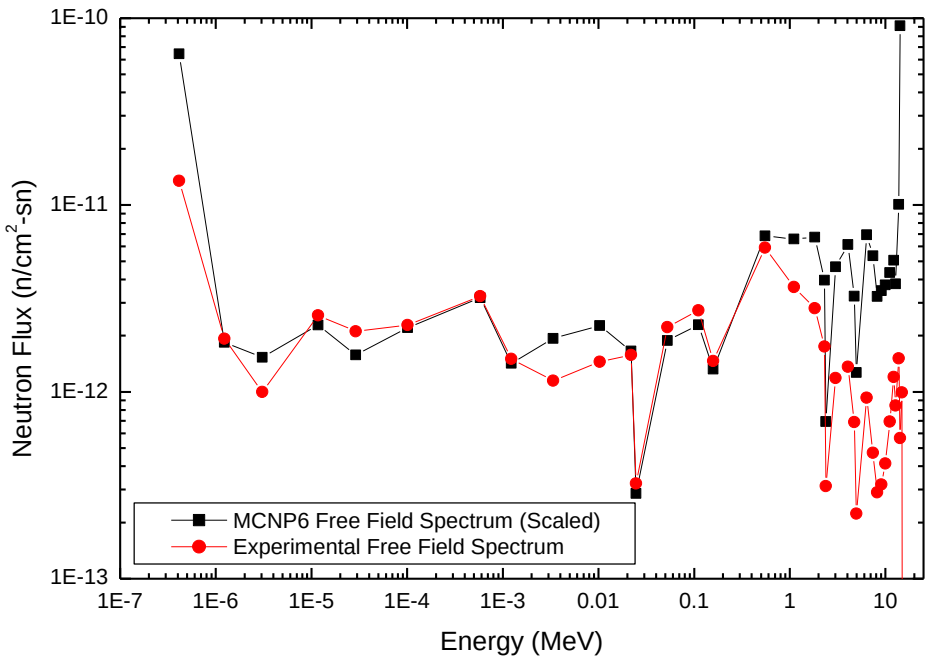

Figure 9. Free-field neutron spectra results, both experimental and computational, with experimental data extracted from Heimbach results [28]. Spectra were emitted by a 14.1 MeV neutron source at a distance of approximately 402 meters and measured using polyethylene moderators.

Based upon this comparison, the possibility exists that an unidentified and undocumented scaling factor of 100 was applied to the data obtained in 1984. Unfortunately, that experiment lacked detailed documentation concerning the manipulation of the data, which might account for this difference. Nevertheless, the fact that the MCNP6 data accurately recreates the shape of the reported neutron spectra in both cases suggests MCNP6 provides a reasonable approximation for this data.

Additionally, although the 1984 benchmark experiment provided no explanation for how the neutron spectra were unfolded using the provided BSS response functions, the MAXED software provided a reasonable estimate for the neutron spectra even when estimated values for the absolute and percentage uncertainties were applied. Figures 10

and 11 demonstrate the agreement between the published neutron spectra, those unfolded by unidentified means, and those unfolded using the MAXED software.

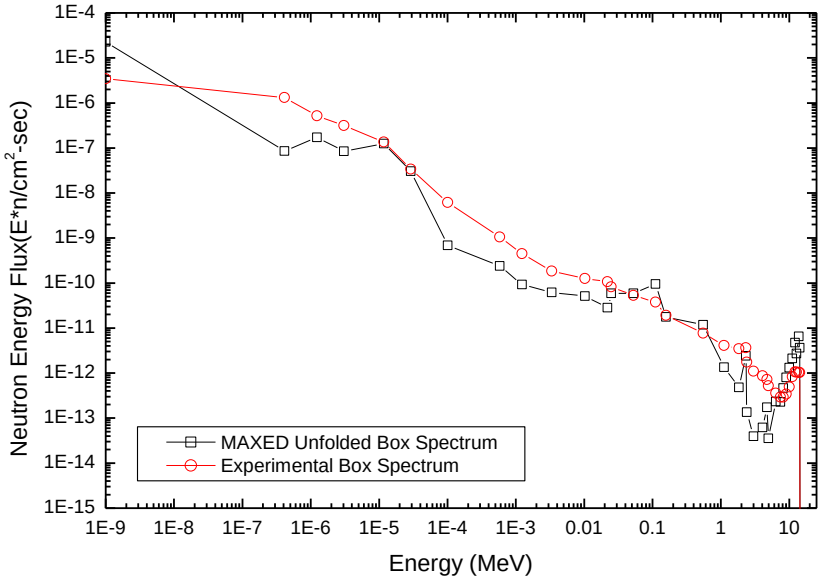

Figure 10. Comparison of the MAXED-generated and experimentally determined neutron flux spectra within the iron box. The spectra were generated based upon the reported BSS count rates and detector response functions provided in the benchmark experiment of 1984 [28].

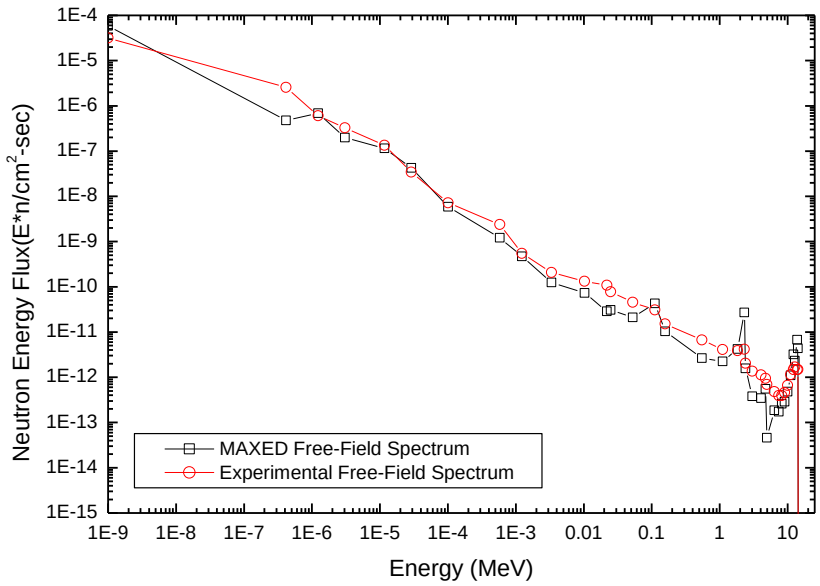

Figure 11. Comparison of the MAXED-generated and experimentally determined neutron flux spectra for the free-field environment. The spectra were generated based upon the reported BSS count rates and detector response functions provided in the benchmark experiment of 1984 [28].

Both MAXED spectra demonstrate good overall agreement with the spectra reported in the benchmark experiment. Specifically, the free field spectrum returned values differing by less than 6% from the experimental data. Unfortunately, MAXED values computed for the box spectrum produced differences of more than 23% relative error when compared to the experimental values. Due to the lack of data critical to the refinement of these spectra, a more accurate calculation may not be possible.

Lastly, the comparison of the neutron flux spectra for the free-field and iron box demonstrates a remarkable agreement between the experimentally reported data and those replicated computationally by MCNP6. In fact, MCNP6 results for the iron box NPF are in almost perfect agreement with those experimentally determined. Through the application of Equation (1.2), it can be shown that MCNP6 calculations for the NPF of the iron box fall within 5% of those determined experimentally. The NPF ratio represents the most important data analysis from this comparison, and the fact that these results stand in such excellent agreement strongly supports further investigation of MCNP6 for applications in assigning vehicle protection factors to military vehicles.

Summary

The significant conclusion drawn from this experiment is that historical data on neutron transport were accurately replicated using MCNP6, and a validation of the software was completed through comparisons of the computational and experimental results. The demonstrated accuracy of MCNP6 in computing the NPF for this example is a direct result of its ability to model particle interactions, thereby producing accurate neutron flux spectra. Additionally, despite the use of arbitrary error values, MAXED

returned unfolded spectra in relatively good agreement with the published values. Therefore, MCNP6 and MAXED appear promising in their ability to provide reliable data for more complicated experiments.

IV. Experimental Methods

Chapter Overview

This chapter describes the setup and execution of the principle experiment used for this research, one designed to validate MCNP6 for NPF assessments using simplified geometries and materials. Additionally, this chapter also provides a firm methodology to support future efforts in validating MCNP6 for other components of RPF assignment. Ancillary experiments conducted in support of these objectives are also described in this chapter, including a detailed methodology for the calculation of new BSS response functions using MCNP6 and the experimental characterization of a plutonium-beryllium (^{239}PuBe) source.

Bonner Sphere Response Functions

The purpose of this research was to utilize MCNP6 to replicate and improve upon the Bonner sphere response functions published in the benchmark study conducted by Vladimir Mares and Hans Schraube in 1994 [29]. Monte Carlo codes such as MCNP have been leveraged for this purpose before, and comparisons of these computational solutions against experimental measurements have shown excellent agreement [24].

As explained earlier, response functions are essential for spectrum deconvolution, or unfolding, when using a BSS; the response functions, which together comprise a response matrix, are represented by $R_{j,g}$ in Equation (2.9). Therefore, all BSS spectrum unfolding software, including MAXED, relies upon a user-provided response matrix to derive the optimal flux spectrum solution from this equation. The results of this

experiment are included in this chapter, with the response functions produced by MCNP6 incorporated into the MAXED program for all subsequent spectrum unfolding described in this document.

The response functions were modeled using MCNP6 to assist in the verification of the software, as well as due to the practical limitations preventing their experimental determination. Specifically, the shortage of mono-energetic neutron sources from thermal to multiple MeV energies necessitates the use of such computational methods. For the purposes of this experiment, the response functions were calculated using energies from thermal to fast, or 1.0×10^{-08} to 25.12 MeV. Furthermore, due to the use of a 4x4 mm LiI(Eu) scintillator in the following experiments, this same detector configuration was utilized in the modeling of the response functions. The final response matrix includes the bare scintillator, as well as the 2, 3, 5, 8, 10 and 12-inch diameter spheres.

Material Design

Although standard LiI(Eu) scintillators consist of ^{6}Li, ^{7}Li, and ^{127}I, as well as trace amounts of Eu, the modeled crystal was a combination of only ^{6}Li and ^{127}I. This was based upon the MCNP4 input used by Mares and Schraube [29] and provides a set of isotopes with cross sections for neutron absorption shown in Figure 12. Neutrons reaching the LiI(Eu) crystal are absorbed by this combination of nuclei; however, for this research, the sole interest rests in the neutron absorption by ^{6}Li.

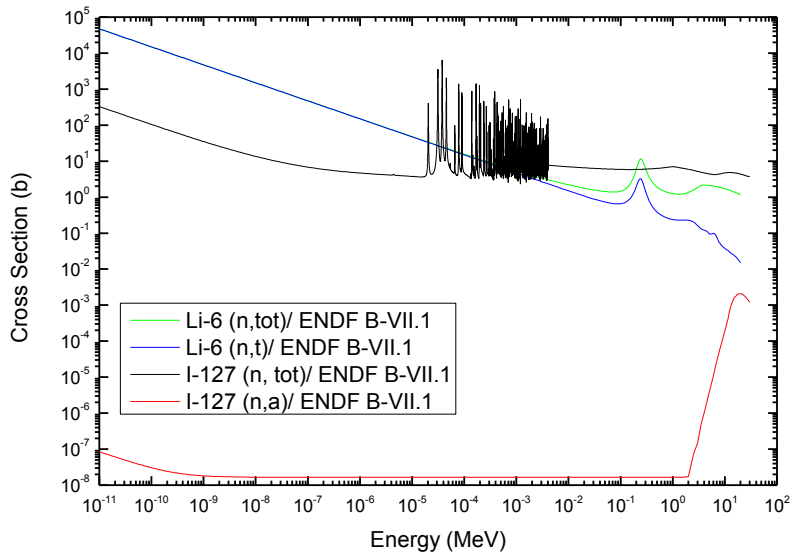

Figure 12. ENDF/B-VII neutron absorption cross sections of ^{6}Li and ^{127}I. This plot serves to graphically illustrate the energy range of neutron absorptions in the MCNP6 model [30].

The literature provided an assumed crystal density of 3.84 g/cm^3, and a weight fraction in MCNP6 of 5.18% ^{6}Li and 94.82% ^{127}I. Based upon this knowledge, the atomic number density, N, can be determined from the equation

$$N = \frac{\rho N_A}{M}, \tag{4.1}$$

in which ρ is the crystal density, N_A is Avogadro's number, and M is the molar mass. Using the associated molar mass of 132.919 g/mol, the final atomic number density may be derived as

$$N = \frac{\rho N_A}{M} = 1.74E22(atoms/cm^3), \tag{4.2}$$

which is consistent with the value derived by Mares and Schraube [29]. Lastly, the density of the polyethylene spheres was assumed to be 0.95 g/cm^3, in accordance with the literature.

Constants of Proportionality

MCNP6 uses a tally multiplier card, or FM card, to multiply any tallied flux by any cross section to produce nearly all reaction rates [25]. Therefore, the FM card is used to calculate any quantity of the form

$$R(E) = C\int \phi(E)\sigma(n,\alpha)dE\,, \tag{4.3}$$

where *R(E)* is the detector response, $\phi(E)$ is the energy dependent neutron flux (particles/ cm^2), and σ represents the MCNP6 cross-section library reaction numbers. This equation provides the $R_j(E)$ component to Equation (2.8), with MCNP6 solving the integration in Equation (4.3) with Monte Carlo methods. This, however, leaves the program lacking the arbitrary scalar quantity used for normalization, which is known as the constant of proportionality, *C*. This value is defined by the material and geometric properties of the experimental environment and was produced for each detector configuration, *i*, using the equation

$$C_i = NA_{Source}V_{Scintillator}\frac{1}{10^{24}}(barns/cm^2)\,, \tag{4.4}$$

where *N* is the atomic number density, A_{source} is the surface area of the disk source, and $V_{scintillator}$ is the volume of the scintillator. The calculated values for these constants are provided in Table 3.

Table 3. Calculated constants of proportionality used in MCNP6 BSS response function modeling.

Detector	Constant of Proportionality
Bare	1.400E-04
2in	1.774E-02
3in	3.990E-02
5in	1.109E-01
8in	2.838E-01
10in	4.435E-01
12in	6.386E-01

Equation (4.4) provided the input data for the tally multiplier card in MCNP6, FM4 (C_i 7 105), where C_i is the detector constant of proportionality, 7 is the crystal material number, and 105 is associated to the (n,t) reaction of ^{6}Li, which only occurs during neutron absorption [27]. Therefore, the response functions are a total count of only neutron absorptions within the ^{6}Li of the crystal scintillator.

Model Design

Within MCNP6, the scintillator crystal was modeled as a 4x4 mm^2 right circular cylinder (RCC) suspended in vacuum inside a 14x16 mm^2 aluminum RCC with wall thicknesses of 4 mm. Each detector configuration was irradiated with a parallel beam of mono-energetic neutrons produced by a circular disk of equal diameter to that of the moderating sphere.

When computing each of the six moderating sphere response functions, the aluminum RCC and the LiI(Eu) RCC crystal were modeled as described above with the circular faces of both RCCs facing the neutron source, as shown in Figure 13. The light pipe, however, was not considered in these instances due to its similar moderating properties to that of the polyethylene [29].

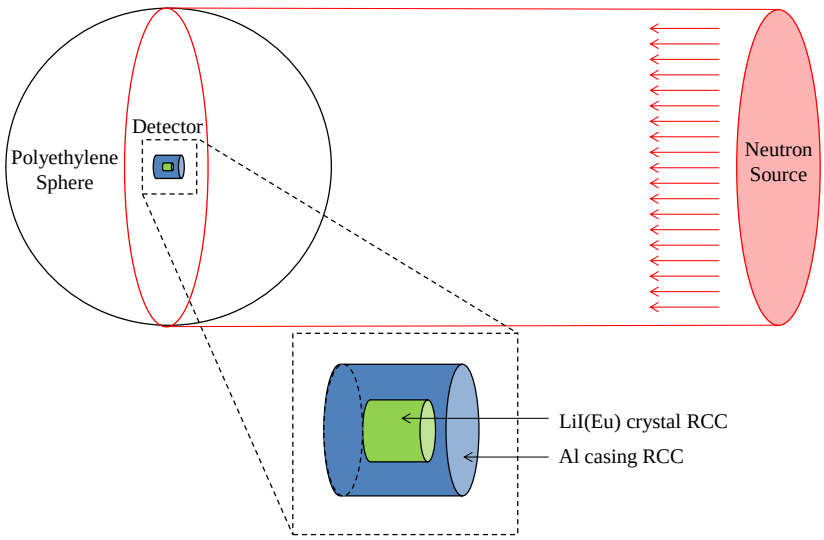

Figure 13. Diagram of the computational model used by MCNP6 to reproduce the response functions for each moderated sphere. Of note, the light pipe is absent from this model.

In the case of the bare detector, the orientation of the crystal was rotated by 90° so that the square-shaped cross section of both crystal and aluminum RCC faced the neutron source. In this configuration, the disk-shaped neutron source was replaced by one of square 4x4 mm^2 dimensions directed toward the crystal. Additionally, because neutrons scattering off the geometry of the light pipe substantially affect the detector response, a modeled light pipe was also added to account for this phenomenon.

Lastly, a thermal neutron scattering treatment was used to account for chemical binding and crystalline structure effects from polyethylene using the S(α,β) treatment offered by MCNP6. Importance sampling was utilized through the design of concentric polyethylene spheres to reduce variance in the model, particle tallies for each response function reduced uncertainties below 4% for every energy level. Example MCNP6 input cards for the bare and 12-inch detector configurations are included in Appendix D.

BSS Response Matrix Results

The MCNP6 model returned a response matrix which differed from the Mares and Schraube data by a factor of two. The application of the older ENDF VI reaction library, upon which Mares and Schraube is based [29], failed to significantly alter the new response matrix results. The conclusion to be drawn from this exercise is that updates within the MCNP code between versions MCNP4 and MCNP6 may be responsible for this discrepancy. Figure 14 displays the MCNP6-generated response matrix, while Figures 15-18 display a sample of the Mares and Schraube data compared against MCNP6 results after applying a scaling factor of two.

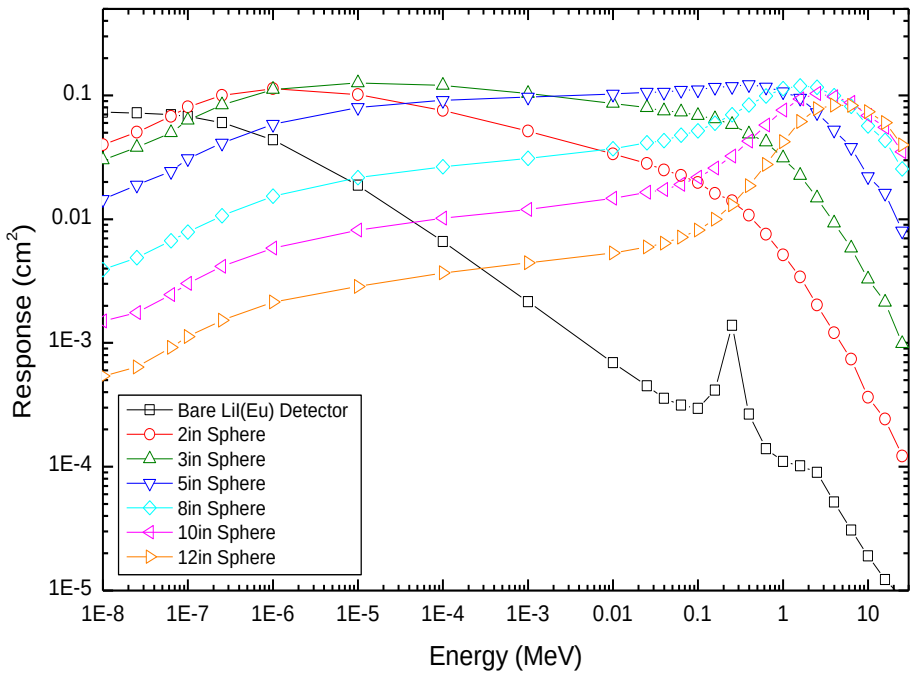

Figure 14. BSS response matrix derived using MCNP6, based upon inputs parameters described by Mares and Schraube [29].

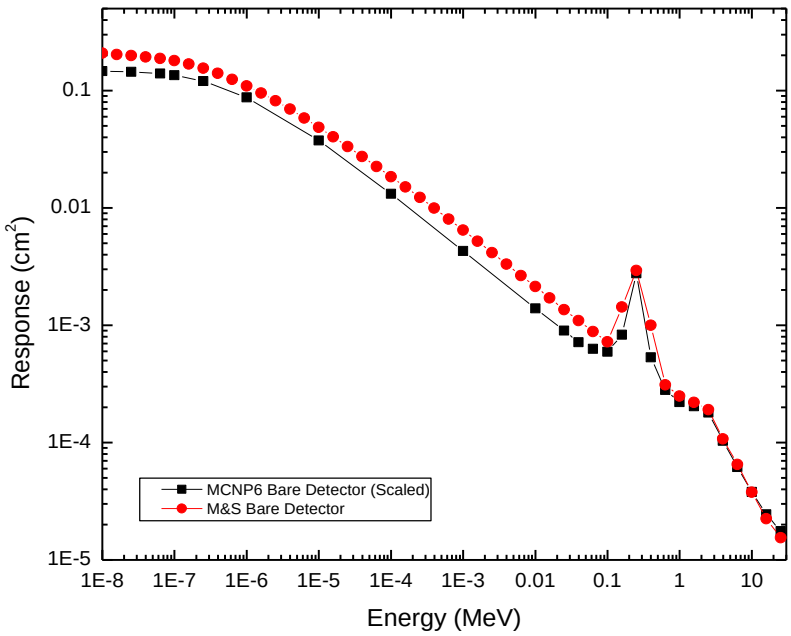

Figure 15. Comparison of Mares and Schraube (M&S) BSS response function for the bare scintillator against the scaled MCNP6-generated data for the same. A minor difference between the two persists across the 1.00E-08 to 1.00E-01 MeV energy range.

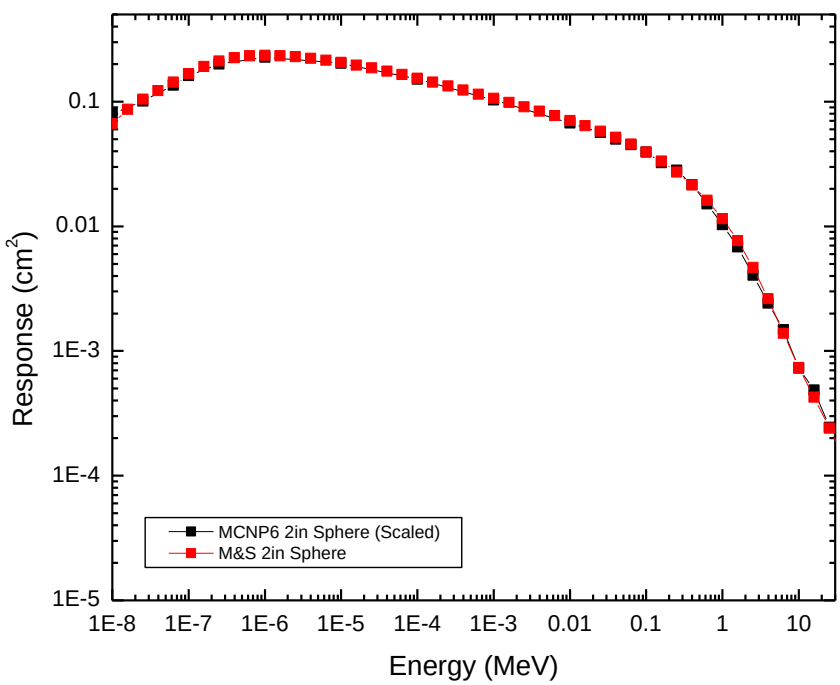

Figure 16. Comparison of Mares and Schraube (M&S) BSS response function for the 2-inch diameter sphere against the scaled MCNP6-generated data for the same.

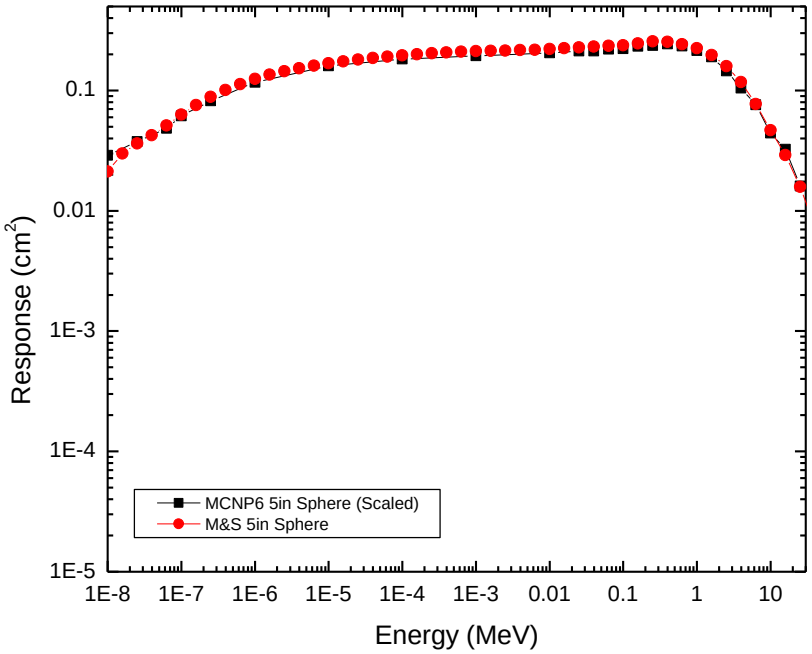

Figure 17. Comparison of Mares and Schraube (M&S) BSS response function for the 5-inch diameter sphere against the scaled MCNP6-generated data for the same.

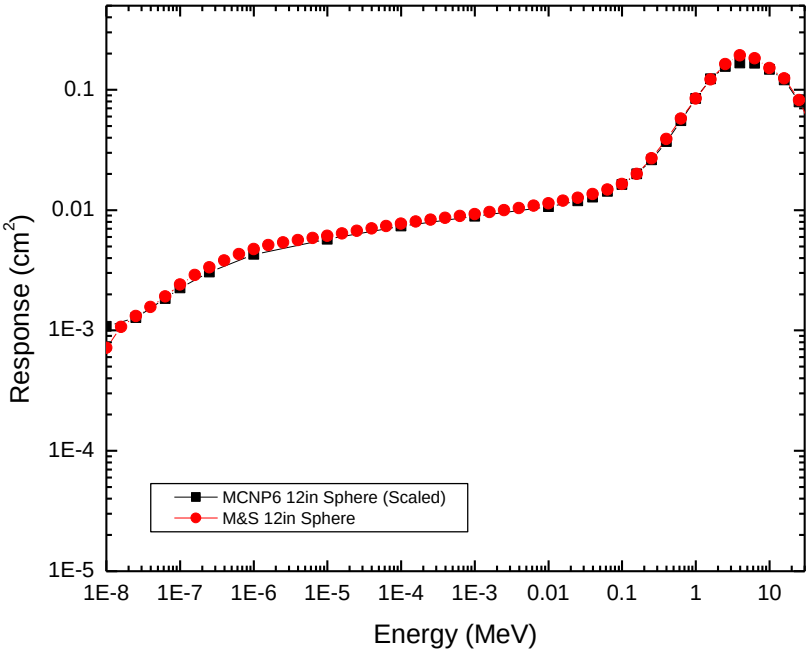

Figure 18. Comparison of Mares and Schraube (M&S) BSS response function for the 12-inch diameter sphere against the scaled MCNP6-generated data for the same.

In the case of the bare detector (Figure 15), a minor difference in value can be seen between the 1.0×10^{-08} and 1.0×10^{-01} MeV energy range. The exact cause for this discrepancy remains unknown, despite the return of identical results using both ENDF VI and VII. As discussed earlier, the difference in values for this detector configuration may be attributed to changes in the internal code libraries between MCNP4C and MCNP6. Regardless of the source, a future argument might be made that the MCNP6 data more closely mirrors the ^{6}Li neutron absorption cross section plot (Figure 12) than the data provided by Mares and Schraube, especially over the absorption peak between 1.0×10^{-01} and 6.31×10^{-01} MeV.

In order to quantify the goodness of fit between the MCNP6 response functions and the 1994 Mares & Schraube data, a χ^2 test was performed. This involved adopting the hypothesis that both response matrices were statistically identical and any deviations in value between the two occur as a result of random fluctuations. To evaluate the hypothesis, the observed values for each response function (O) were compared with the theoretical or expected values (E) using Equation (4.5) [31],

$$\chi^2 = \sum_{i=1}^{k} \frac{(O-E)^2}{E}. \tag{4.5}$$

In the case of this experiment, observed values were drawn from each MCNP6 response function and the respective Mares & Schraube responses constituted the theoretical values. The k-value in Equation (4.5) represented the number of energy groups compared, in this case a value of 26. Only the response values corresponding with these 26 energy bins were compared in this analysis, which terminated at an upper

limit of 25.51 MeV. Using Equation (4.5), calculations of the χ^2 values for both the scaled and unscaled MCNP6 response matrix data are provided in Table 4.

Table 4. Calculated χ^2 values for each detector configuration using MCNP6.

Detector	χ2-scaled	χ2-unscaled
Bare	7.4789E-02	4.4379E-01
2in	5.2026E-03	4.6860E-01
3in	1.2123E-02	7.9543E-01
5in	1.9360E-02	1.1125E+00
8in	1.1315E-02	7.7458E-01
10in	8.2164E-03	5.3874E-01
12in	6.3488E-03	3.7395E-01

As evident in Table 4, the calculated χ^2 values for each detector configuration fall far short of the 34.38 critical value for 25 degrees of freedom and an alpha of 0.10. Therefore, based upon the calculated χ^2 values for each detector, this analysis strongly suggests an acceptance of the null hypothesis. Any minor differences between our experimental MCNP6 response matrix and the data published by Mares & Schraube in 1994 can be attributed to chance fluctuations.

In conclusion, these results firmly justify the incorporation of the unscaled MCNP6 response functions in future applications of MAXED spectrum unfolding within this research, as well as for other applications of BSS response. The MCNP6-derived response function data may be found in Appendix E.

MAXED Files

This section describes the four types of input files used by the MAXED program and explains how the files were used to support the experimental design. This section also describes the maximum entropy principle and algorithm used by MAXED in

accomplishing spectrum unfolding. In all cases, MAXED was operated using the "Few Channel" approach because the number of expected measurements fell far below its maximum of 100, and the energy bins numbered much less than 1000.

Input Files

The four MAXED input files include the control, measured data, response function, and default spectrum files. MAXED is written in FORTRAN 90 and may be run using either a control file or from the prompt. For the purposes of simplicity, as well as reproducibility, a control file consisting of ten records was created for each experiment. These records specify the parameters required by MAXED to run successfully and are described in Table 5.

Table 5. MAXED control file records.

Record	Description	Example Values
1	Name and location of the measured data file	Data.ibu
2	Name and location of the response function file	RF.fmt
3	Name of the output file	Output.flu
4	Name of the default spectrum file	DS.flu
5	Highest energy of the solution spectrum	6.31 or 12.00 MeV
6	Requested final χ^2 per degree of freedom	1.0
7	Temperature and reduction factor	1.0, 0.85
8	Energy bin structure, Solution bins	2.0, 1.0
9	Scaling option for default spectrum	0.0
10	Scaling option for MAXED	0.0

Records 1-4 are arbitrary and based upon the desires of the user; however, the file type is very particular. Control files themselves are written in a "*.inp" format and will function in no other form. Record 5 determines the uppermost limit for the output file; in the case of the D-D spectrum this was set to 6.31 MeV, and in the case of the ^{239}PuBe source this was set to 12.00 MeV. Record 6 enables the user to request χ^2 values of less

than one, which is always optimal. Previous versions of MAXED did not offer this option and uniformly set the value equal to one. Record 7 is used by the simulated annealing subroutine within MAXED, and the values of 1.0 and 0.85 are highly recommended in the MAXED User's Manual [23]. The 8th record allows the user to select the energy bin structure of the output spectrum. In all cases, use of the default spectrum energy bins and an output in units of $d\phi/dE$ (flux/ bin) was selected, so an input of 2.0, 1.0 was used. The two final records enable spectrum scaling using a binary input of 1.0 for "yes" and 0.0 for "no," first for the default spectrum and lastly for the output spectrum. In all cases, 0.0 was selected because spectrum scaling was to be handled manually outside the confines of the MAXED program.

The second file MAXED requires for spectrum deconvolution is the measured data file, which provides all the experimental data and associated uncertainties from using the BSS and LiI(Eu) scintillator. This information is listed in three principal records, with the third entry consisting of seven items. This final record repeats itself for each different moderator configuration used in the experiment. The formats for these files, as well as example values used in the experiment, are shown below in Table 6.

Table 6. MAXED measured data file records.

Record	Description	Example Values
1	Name of the input data file	Input
2	Number of measurements	7
3a	Eight character identification	Bare, 2in, etc.
3b	Moderator diameter (inches)	0, 2, etc.
3c	Measured count rate (c/s)	6.57, 14.23, etc.
3d	Uncertainty due to statistics (absolute)	0.02713, 0.06133, etc.
3e	Uncertainty due to statistics (percentage)	0.413, 0431, etc.
3f	Other uncertainties (FWHM)	2.63, 2.2, etc.
3g	A "flag" to include or exclude a measurement	1-7

The third MAXED input file is the response function file, which details both the energy bins and corresponding responses for the bare detector and each moderating sphere. There are seven records in this input file, with the seventh record repeating to account for each specific response function. Table 7 provided descriptions of each of these records.

Table 7. MAXED response function file records.

Record	Description	Example Values
1	Header (user specified)	Input
2	Header (user specified)	7
3	Number of energy bins and units of energy	27, 1(MeV)
4	Response function energy bin edges	1.00E-08, 2.518E-08, etc.
5	Dummy variable, meaningless	0
6	Number of response functions	7.0000E+00
7a	Response function identification	0Bare, 2in, 3in, etc.
7b	Units of response	1.00E+00 cm^2
7c	The specific response values	7.3079E-02, 7.2247E-02, etc.

The final input file used by MAXED is the default spectrum, which serves as the *a priori* information against which all the possible solution spectra generated by MAXED are compared. This is especially important in the Few Channel setting, where the number of detector configurations is much smaller than the number of energy bins, resulting in an under-defined system of equations. The records used for the default spectrum input file are described in Table 8.

Table 8. MAXED default spectrum input file records.

Record	Description	Example Values
1	Header (user specified)	DS
2	Default spectrum form, Energy units	2 (Fluence rate/bin), 1 (MeV)
3	Dummy variable, Num. bins (x2), Max energy	2, 23, 23, 6.31 (MeV)
4	Energy bin edges, Magnitude	1.00E-08, etc., 0

The MAXED Algorithm

MAXED uses a maximum entropy algorithm to derive the optimal spectrum from a variety of possible solutions. This can be more simplistically defined as a set of input parameters, a set of output parameters, and the equations relating those quantities [23, 27], where k represents the specific detector from $1\ldots m$, i is a specific energy bin from $1\ldots n$, and $m<n$. Based upon these conditions, the unfolding leads to a set of parameters (λ,γ) that satisfy the following two equations

$$N_k + \varepsilon_k = \sum_i R_{k,i} f_i \,, \tag{4.6}$$

and

$$\sum_k \frac{\varepsilon_k^2}{\sigma_k^2} = \Omega \,, \tag{4.7}$$

where

N_k is the measured counts,

ε_k is the difference between the measured and expected value for detector k,

σ_k is the estimate of the measurement error,

f_i is the solution spectrum,

$R_{k,i}$ is the response for detector k and

Ω is a parameter that fixes the χ^2 of the solution (user defined).

Both equations set the constraints on the overall entropy equation. Equation (4.6) correlates the measured data to the associated response function and solution spectrum, while allowing for measurement error. Equation (4.7) constrains the ε_k by assuming that

the χ^2 of the solution is the value defined by the user. Based upon these conditions, the entropy, S, can be written as

$$S = \sum_f (f_i \ln(\frac{f_i}{f_i^{DEF}}) + f_i^{DEF} - f_i), \tag{4.8}$$

where f_i^{DEF} is equal to the default spectrum value for the i-th energy group. The maximization of Equation (4.8) results in the following two equations,

$$f_i = f_i^{DEF} \exp(-\sum_k (\lambda_k + \frac{\gamma}{\sigma_k}) R_{k,i}), \tag{4.9}$$

and

$$\varepsilon_k = \frac{\lambda_k \sigma_k^2}{2} \sqrt{\frac{4\Omega}{\sum_j (\lambda_j \sigma_j)^2}}. \tag{4.10}$$

These equations enable a solution to be determined for λ_k, and a maximization of the potential function $F(\lambda_k)$ is possible using the simulated annealing expressions in MAXED. Since the maximum entropy solution can be written in closed form, Equations (4.6) and (4.7), as well as Equation (4.9) and (4.10), may be used to calculate the effect of small changes in the input parameters [27].

^{239}PuBe Source Characterization

Source

The source used for this experiment was AFIT source number 00300, a 4.89 Ci ^{239}PuBe sample created on 23 June 1960. The 79.79 gram source was manufactured by Monsanto and assigned a serial number of M-580. The source is housed in a cylindrical

aluminum casing attached to long aluminum rod, which was used for source placement and manipulation.

Experimental Setup

Measurements were recorded in the basement of Building 470 on WPAFB using the small source handling room, which is encased by approximately 24 inches of concrete shielding on every side. During measurements, the cylindrical source was positioned flat on a thin plastic table with the length of the casing facing toward the detector. Thin pieces of aluminum set on each side and at its end prevented the source from rolling on the table and allowed for consistent placement during each measurement.

For this portion of the experiment, measurements were recorded using the BSS transport cart to support the detector, and the LiI(Eu) scintillator was placed at a distance of exactly one meter from the ^{239}PuBe source. Figure 19 provides a picture of the transport cart configuration with the bare scintillator in the upright position.

Figure 19. Sample setup of the BSS using the transport cart as a measurement apparatus with the bare scintillator atop the cart.

The specific types of equipment utilized in this experiment are listed below in Table 9, as well as the serial numbers of the exact items used. The LiI(Eu) detector was connected to a preamplifier to provide it with power, as well as to transmit its measurements through the linear amplifier to the ADCAM and on to the laptop for data analysis. Figure 20 provides a line and block chart showing how all the instrumentation was connected, and Table 10 lists the specific settings used on the power supply and linear amplifier.

Table 9. Instruments used to record measurements for the ^{239}PuBe spectrum characterization.

Instrument	Model	Serial Number
Bonner sphere spectrometer (BSS)	Ludlum	6306
LiI(Eu) scintillator and light pipe	Ludlum 42-5	PR300004
NIMBox	ORTEC	60096
Preamplifier	ORTEC 142IH	2012
High voltage power supply	Canberra, 3102D	875
Linear amplifier	ORTEC 572	4745
ADCAM MCB	ORTEC 926	6165198
Laptop with ORTEC Gamma Vision	Gateway	N/A

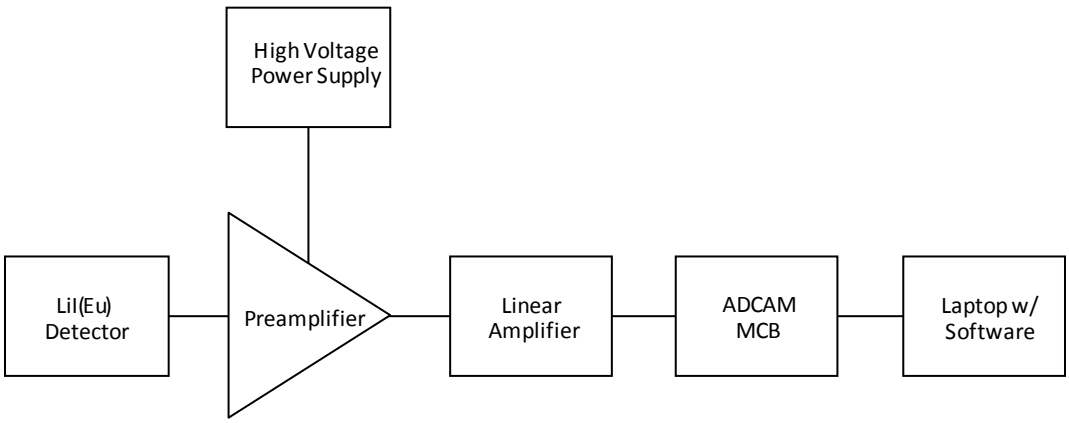

Figure 20. Detection system electronic setup utilized during the ^{239}PuBe spectrum characterization measurements.

Table 10. MAXED default spectrum input file records.

Equipment	Model	Setting(s)
High Voltage Power Supply	Canberra 3102D	650V
Linear Amplifier	Ortec 572	Gain= 1.00
		CG= 20
		Shaping Time= 2 μsec

Measurements were recorded through the ADCAM MCB using ORTEC Gamma Vision software, and response curves were recorded for post processing analysis. All seven detector configurations were utilized, including the bare scintillator and the 2, 3, 5, 8, 10, and 12 inch spheres. The gross number of counts recorded under each alpha peak was set at 65,000 to allow for sufficient statistical certainty in the results. Following the $1/\sqrt{(N)}$ uncertainty, this implies that 65,000 gross counts will result in a count rate uncertainty of ~0.4%, which is considered acceptable.

Modeling in MCNP6

The MCNP6 model for this experiment consisted of a cubical room, with concrete walls set to a thickness of two feet. The source was defined as isotropic, and the LiI(Eu) detector was modeled at a distance of exactly one meter from the source. Figure 21 provides a diagram of the model based upon the MCNP6 input cards, although the point source representing the ^{239}PuBe cylinder is not visible.

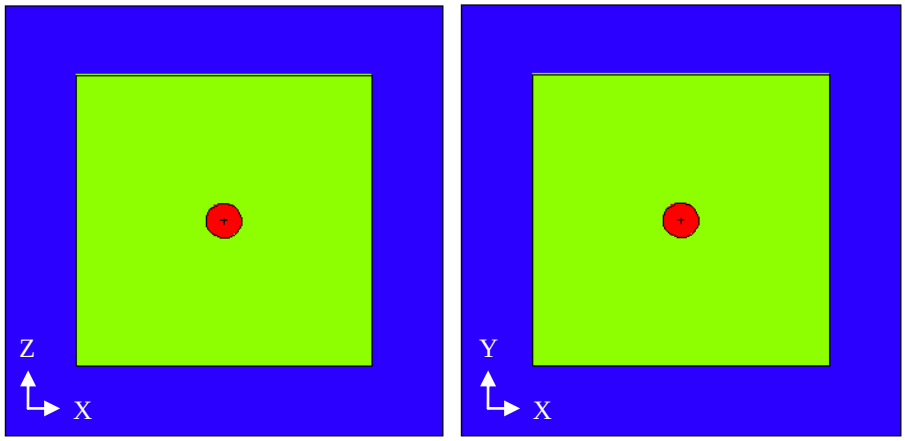

Figure 21. Computational model of the 12 inch Bonner sphere (red) within the source chamber, here modeled as a cube (XZ and XY coordinates, respectively). The isotropic ^{239}PuBe source cannot be seen; however, it is modeled at a range of exactly one meter from the crystal. The red circle is the polyethylene sphere, and the dot represents the aluminum RCC containing the LiI(Eu) crystal.

An F4 tally was used to determine the average neutron flux within the crystal, and concentric spherical layers of polyethylene increased the importance of neutrons traveling toward the detector. The source was modeled using both SI and SP definitions to account for the variable intensity and probability of the emitted neutrons, respectively. The MCNP6 input file used in this experiment is included in Appendix F.

Neutron Protection Factor (NPF) Experiment

Source

The Adelphi Technology DD108 Neutron Generator located in Building 194 of WPAFB served as the neutron source for the steel box and free field measurements recorded in this experiment. This device, as with many similar systems, utilizes a deuterium-deuterium fusion reaction to produce 2.45 MeV neutrons nearly isotropically from the target chamber. This reaction can be described using the equation

$$ {}^{2}_{1}\mathrm{H} + {}^{2}_{1}\mathrm{H} \rightarrow {}^{3}_{2}\mathrm{He}\ (0.82\ \mathrm{MeV})\ +\ {}^{1}_{0}\mathrm{n}\ (2.45\mathrm{MeV})\,, \qquad (4.11) $$

with the reaction products being a triton and a free neutron. This particular reaction is popular in scientific research for a number of reasons. First, due to the relatively low coulomb barrier between the deuterons, once a build-up of deuterons accumulates on the titanium target, the remaining incident deuterons require very little acceleration to create fusion. This means the power requirements for this type of system are low, usually only between 100-300 kV, so the neutrons produced are essentially mono-energetic. Second, the emitted neutrons are easily moderated and/or shielded, especially when compared to the more energetic D+T reaction, which produces neutrons with energies of 14.1 MeV. Figure 22 provides a picture of the accelerator head, where the deuterons are accelerated into the titanium target.

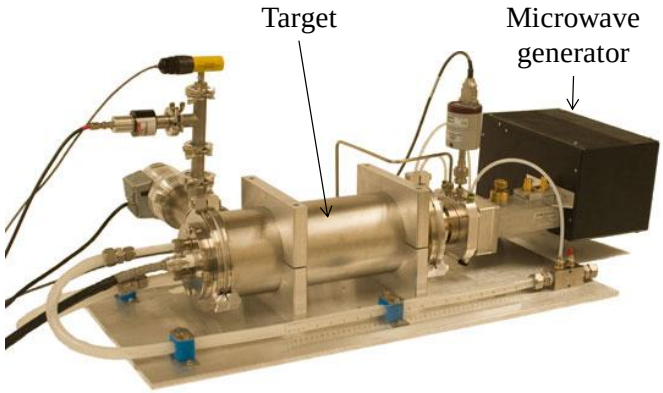

Figure 22. Adelphi Technology DD108 Neutron Generator accelerator head, which was used to create a neutron source of 2.45 MeV at a rate of approximately 3x10^{7} neutrons per second on pulse mode.

The entire generator consists of three main parts: the accelerator head (Figure 22), the power supply and control rack, and a separate heat exchanger to pump coolant into the system. The control rack consists of a 2 kW high-voltage power supply along with

gauges and interface controls to monitor and adjust the vacuum and gas flow. A computer program controls the entire system and may be operated on either continuous or pulsed modes. Pulse mode operation affords the user a variety of selectable parameters, such as pulse length, rise and fall times, dwell time, etc. Figure 23 illustrates these major system components.

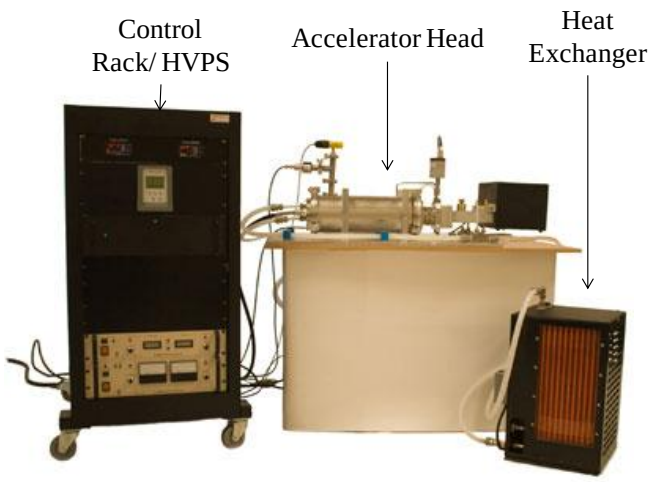

Figure 23. Depiction of the Adelphi Technology DD108 Neutron Generator control rack, accelerator head, and heat exchanger.

The Adelphi generator produces a maximum of $1x10^8$ neutrons per second when operated in continuous mode. For the purposes of this experiment, however, the system was operated in pulse mode to meet WPAFB radiation safety requirements for dose rates. The specific operating criteria employed for this experiment are listed in Table 11.

Table 11. Adelphi Technology DD108 operating settings for this experiment.

Setting	Value
Operating mode	Pulse
Pulse width	300 milliseconds
Accelerator voltage	100 kV
Beam current	4 mA
Neutron yield	~ $3x10^7$ n/sec
Repetition Rate	1 Hz

Experimental Setup, Steel Box

This research focused on recreating the benchmark radiation transport tests of the 1950's-1990's [13, 28, 31], thereby including the use of a metal cube constructed of iron, ^{56}Fe, or steel. The cubical geometry was meant to simulate, in a very simplistic sense, the shielding afforded by military vehicles and thereby enables a calculation of NPF. Furthermore, the material selected for the box fabrication offers an extremely predictable response to neutron interactions based upon the known cross sections for neutron interactions with iron.

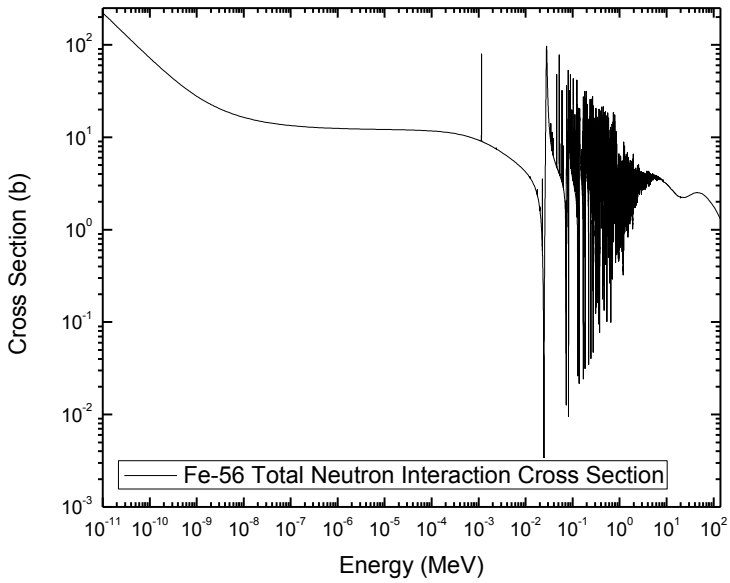

Figure 24. A plot of the total neutron interaction cross section with ^{56}Fe, as provided by the Evaluated Nuclear Data File (ENDF) [32].

Combined, these factors enable a set of controlled circumstances ideal for both experimental and computational measurements of neutron flux inside and outside the iron case. Future testing may incorporate greater complexity in terms of geometries and materials; however, prudence and experience dictate a crawl, walk, run approach to this verification and validation of MCNP6.

Instructions detailing the setup of the steel box testing apparatus are contained within the NSERC Steel Box Construction SOP, which describes the proper assembly and disassembly procedures used to ensure consistent testing conditions for each experimental measurement [33]. Specifically, the SOP details how each of the aluminum frame components and steel plates must be assembled to best replicate the position and orientation used during previous experimental measurements. Aluminum was selected as the frame material due its relatively low microscopic cross section for fast and epithermal neutron absorption, 2.99×10^{-3} and 4.53×10^{-3} barns respectively.

During the experiment, the steel box was positioned with the three-inch diameter hole through the steel facing upwards, as shown in the Figure 25 schematic.

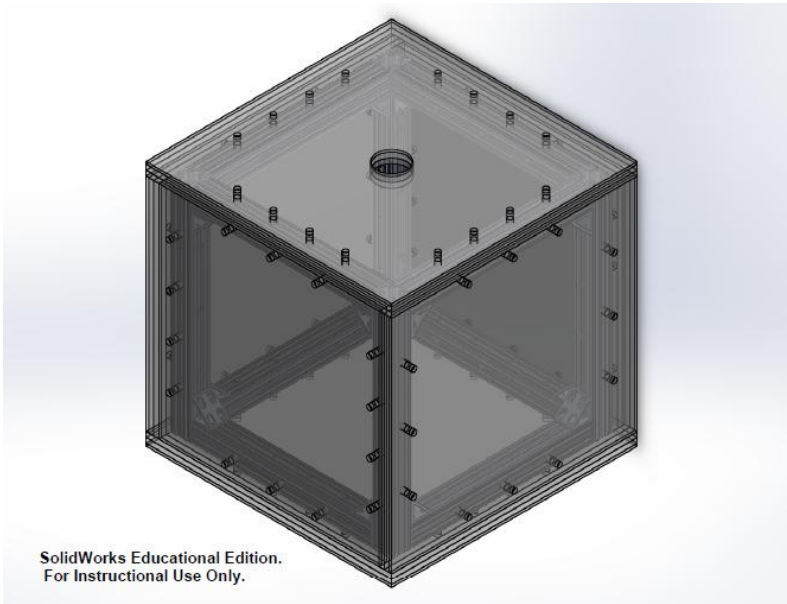

Figure 25. Representation of the NSERC steel box testing apparatus, here shown with the scintillator opening in the upward position. The steel plates are bolted to an aluminum frame during measurements.

The hole allowed the emplacement of the LiI(Eu) scintillator light pipe and cables connecting the detector to the preamplifier. The steel box was positioned on the wood

surfaced laboratory table at a distance of 24.13 cm from the accelerator head of the DD108 Neutron Generator. A large percentage of the 2.45 MeV neutrons produced were expected to strike the steel of the box, allowing measurements of the internal and external neutron flux. Figure 26 offers a simplified diagram of the box setup in relation to the accelerator, excluding the four inches of borated polyethylene (BP) shielding on all sides. The purpose of the surrounding BP was to moderate neutrons as they escaped the steel box, as well as to prevent any neutrons from reentering the steel box after scattering off the concrete walls of the accelerator room.

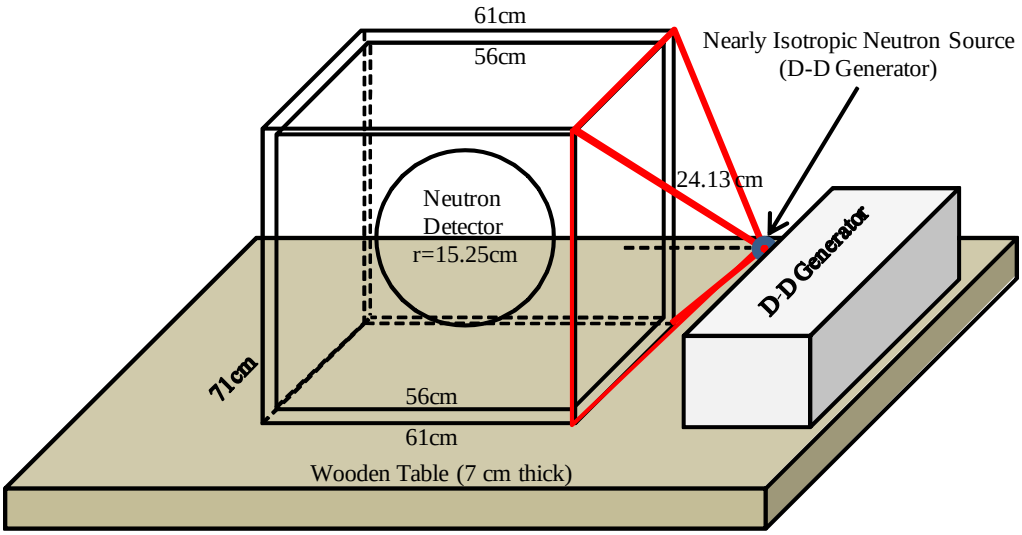

Figure 26. A simplified version of the experimental setup, illustrating the placement of the steel box and BSS spheres in relation to the DD108 accelerator. This diagram does not include the 2ftx2ftx4in blocks of borated polyethylene which surrounded the entire setup.

Based upon physical constraints of the neutron shielding, one entire face of the box was removed between all measurements to allow for the replacement of different BSS spheres. This involved the removal of twelve bolts, in addition to the steel plates. A picture of the open box is shown below in Figure 27.

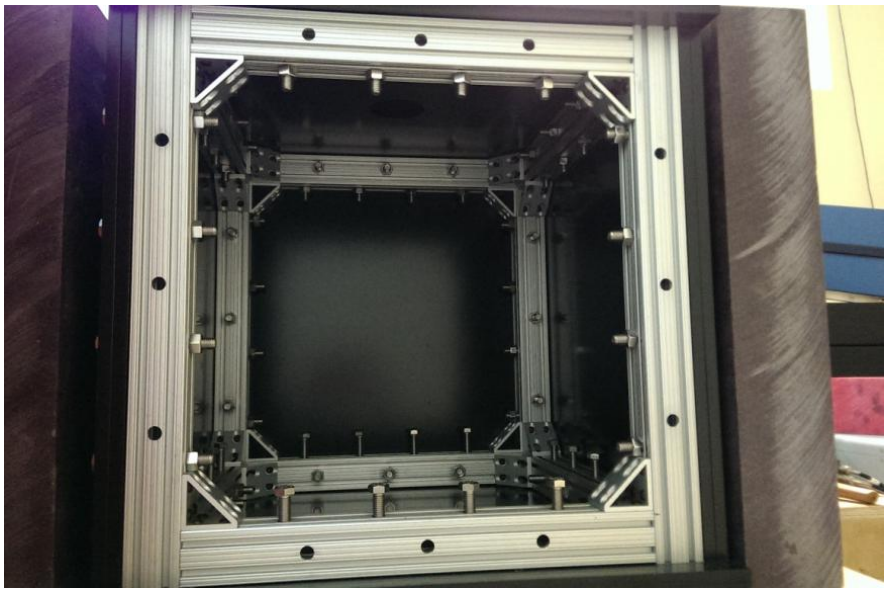

Figure 27. Photo showing the empty steel box with one side missing for BSS detector emplacement. The scintillator and cabling hole can be seen in the top. The DD108 accelerator target plate is located 10.5" beyond the far steel plates.

Experimental Setup, Internal Equipment

Within the steel box, a 6x6 inch SEOH aluminum laboratory jack was utilized to center each of the Bonner spheres within the steel box. The lab jack was first centered within the steel box using two diagonal lines drawn from opposite corners on the inside of the bottom steel plate. By placing all four of the lab jack's square corners on the four diagonal lines, the jack was able to be rapidly centered within the x,y-coordinates of the steel box. A top-down diagram of this is shown in Figure 28.

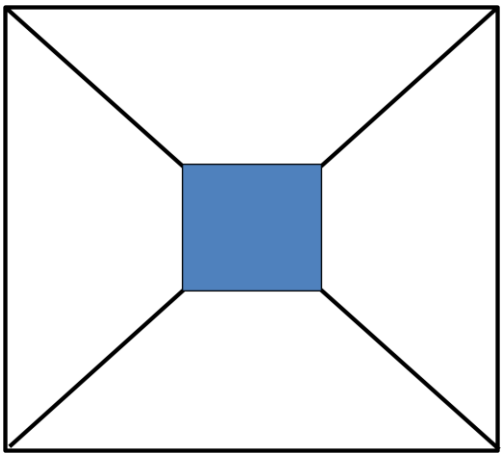

Figure 28. Top-down diagram of the diagonal guidelines used to center the SEOH lab jack (in blue) centered on the bottom plate within the steel box. By aligning all four corners of the lab jack along these diagonal guidelines, the jack was centered within the steel box quickly and accurately in the x,y-coordinate plane.

Once the lab jack was centered on the bottom plate, the spheres were then stabilized and centered in the z-coordinate before measurements were recorded. On top of the lab jack, three one-inch tall aluminum stability rings of different diameters were utilized to support the six different spheres, so each ring was designed to optimally support two sphere diameters. In order to quickly center the stability rings on the lab jack, outlines of these rings were traced onto the top of the lab jack, as well as markers on the rings to ensure consistent emplacement was adhered to during every measurement.

Once each sphere was placed upon its specific stability ring, a small bubble level was used to ensure the scintillator was positioned vertically in the z-coordinate direction. The use of the level on the light pipe helped to maintain a consistent crystal orientation with respect to the source for each measurement. Figure 29 provides an example of the experimental setup described, with the lab jack, 12 inch moderator sphere, and scintillation detector removed to demonstrate their positioning inside the steel box.

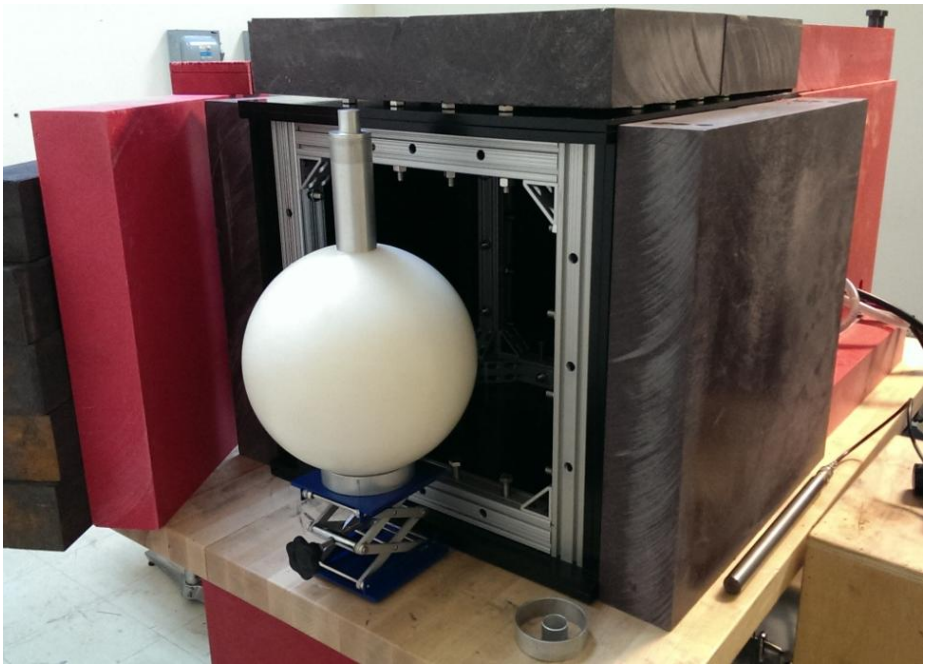

Figure 29. Demonstration of the experimental setup, removed from the box. The 12-inch Bonner sphere is resting on its stability ring atop the SEOH lab jack with the LiI(Eu) scintillator oriented vertically.

Next, the lab jack was adjusted to the premeasured position for the specific diameter sphere, which ensured the LiI(Eu) crystal was centered within the steel box in the z-coordinate. These pre-measured heights for the lab jack were measured prior, with marks placed on the lab jack to correspond to these specific heights. For measurements utilizing only the bare scintillator, the lab jack was raised to the designated height of 27.2 cm, which centered the LiI(Eu) crystal at 28.0 cm in the z-coordinate, the exact center of the box in the z-coordinate.

Experimental Setup, Free-Field

To facilitate the neutron spectroscopy of the free-field environment, these measurements were duplicated, except for the presence of the steel box. For this second

set of measurements, a 2.51 cm thick section of wood supported the SEOH jack, thereby maintaining consistent vertical height of the BSS within the borated polyethylene shielding. Additionally, the material selected offered minimal cross-sectional probability for neutron absorption and scatter, thereby maintaining the integrity of the free field. Lastly, due to the absence of the steel box, the BP shielding on either side of the detector was collapsed to support the top layer of shielding. A schematic of this experimental design is provided later in Figure 32. All other configurations and methodologies remain identical to those employed for measurements of the neutron spectrum within the steel box

Experimental Setup, Electronic Equipment

Figure 30 provides a general diagram of the electronics utilized for this experiment. The first step consisted of connecting all the equipment and using the oscilloscope to ensure proper functioning. Once all the electronic equipment was verified operational, the detector was connected and the bias turned on. The settings for the equipment mirror those described for the ^{239}PuBe source characterization in Table 10.

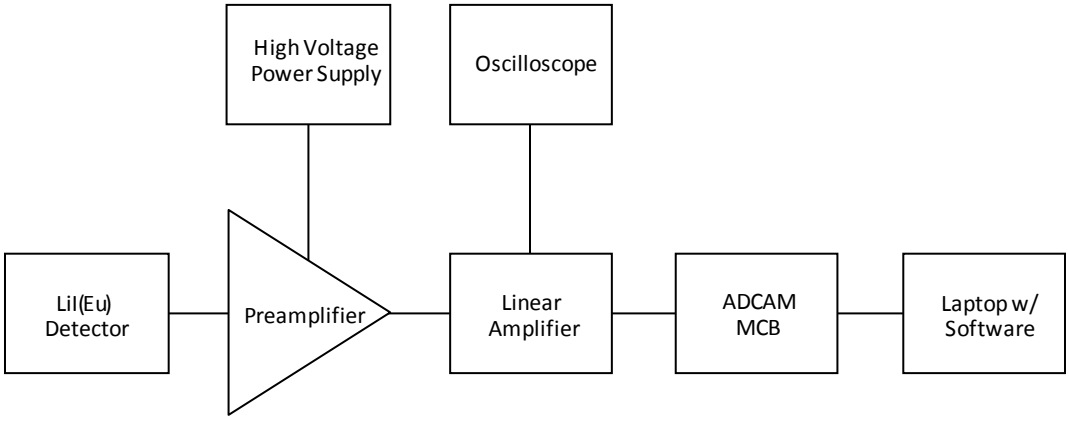

Figure 30. Detection system electronic setup utilized during all measurements of the DD108 spectrum within the steel box and for the free-field.

Measurements were recorded for all seven configurations within the steel box and for the free field using ORTEC Gamma Vision software. The saved spectra enabled post-processing and ROI adjustment, which affected the count rates and statistical uncertainty of the results. A gross number of 65,000 counts recorded under the alpha peak for each detector configuration allowed the statistical certainty for each count rate to approach ~0.4%. These measurements concluded the entire experimental portion of this research, with the exception of the data analysis via MAXED unfolding software and comparison against the MCNP6 models.

MCNP6 Modeling

The MCNP6 model for this experiment consisted of the steel box, the wooden table upon which it rested, the BP shielding (to account for neutron scattering) and a vacuum-filled aluminum tube to replicate the neutron accelerator head. A diagram of the MCNP6 model for the steel box computation is provided below in Figure 31 for visualization purposes.

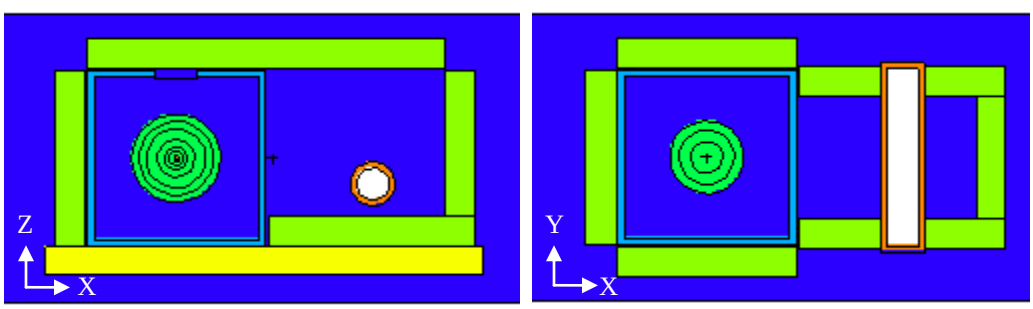

Figure 31. Depiction of the MCNP6 model used to computationally derive the expected flux spectrum present within the steel box from the DD108 Neutron Generator. The two images represent the XZ and XY axes, respectively. The image on the right shows in white the cross section of the vacuum-filled aluminum cylinder which forms a part of the DD108 accelerator head. The isotropic source is centered therein. The scintillator was modeled using the parameters reported by Mares & Schraube (1994), which were also used in determining the BSS response matrix using MCNP6.

The steel box was modeled as a rectangular parallel-piped object with external sides of 61 cm and internal dimensions of 56 cm, which produced a uniform wall thickness of 2.5 cm. The detectors were modeled as concentric spheres of polyethylene with densities of 0.95 g/cm^3. Importance weights were attached to each sphere as a variance reduction measure, as well as to reduce computational time.

Just as in the case of the steel box, the source location and neutron energy modeled for the free-field remained unchanged; the only modification to the computational design consisted of removing the steel box and a minor change to the BP wall locations. As in the case of the physical experiment, the BP walls on either side of the moderator spheres were moved inward to replicate free field experimental design. Figure 32 illustrates this new configuration in two dimensions, as it was modeled in MCNP6. The MCNP6 input files used to model the neutron flux spectra for the free-field and box are provided in Appendix G

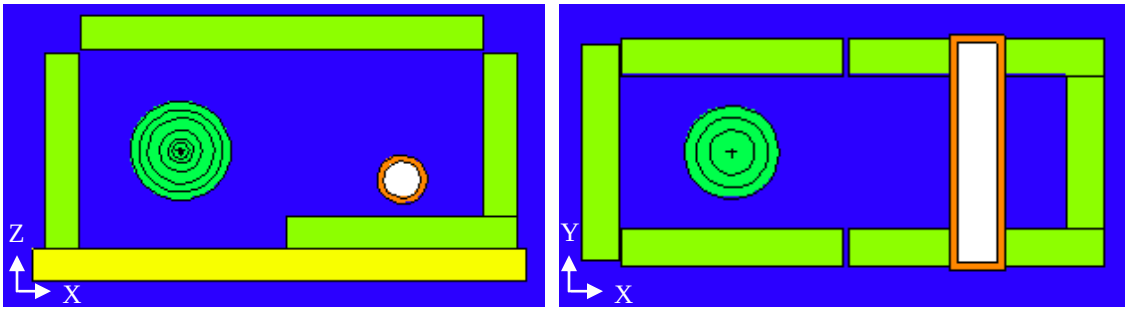

Figure 32. Diagram of the MCNP6 model used to compute the neutron flux spectrum for the free-field based on the DD108 Neutron Generator. The two images represent the XZ and XY axes, respectively.

The scintillator detector was modeled in the same manner as published by Mares and Schraube in 1994. As such, it utilized a vacuum-filled aluminum RCC of 1.4x1.6 cm^2 to house the 4x4 mm^2 LiI crystal. The crystal was modeled using 5.18% ^{6}Li and

94.82% ^{127}I with a density of 3.84 g/cm^3. A schematic of the RCC scintillator model is shown below in Figure 33.

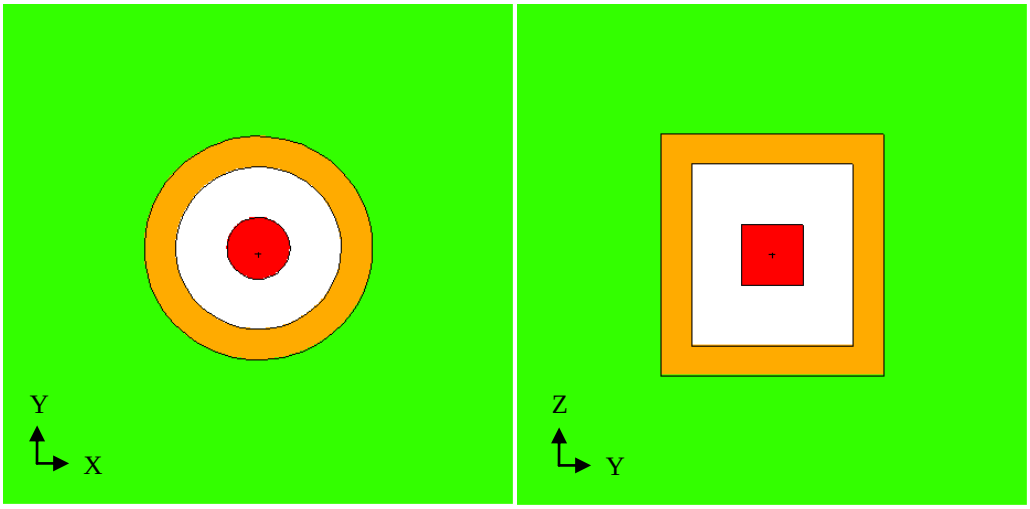

Figure 33. A schematic of the LiI(Eu) crystal modeled in MCNP6 using the technique employed by Mares and Schraube (1994). The images represent the YX and YZ orientations, respectively. Here the crystal is modeled as a RCC (red) in the center of the image surrounded by a vacuum (white). Another aluminum RCC (orange) encases the vacuum with sides 4mm thick. The entire structure is surrounded by polyethylene (green), as part of the BSS moderating spheres.

All data recorded for the neutron spectra were gathered using an F4 average neutron flux tally for the scintillator crystal. These values were measured using the same energy bin structure as used previously for computation of the BSS response matrix. Also, thermal neutron scattering treatment was leveraged to account for chemical binding and crystalline structure effects from the polyethylene using the S(α,β) treatment. Once completed, these values served as the *a priori* information submitted to MAXED as the default spectra for this experiment. This technique is valid due to the excellent consistencies in spectrum structure previously demonstrated by the comparison of MCNP6 flux estimates with the 1984 benchmark experimental data.

V. Results & Analysis

Chapter Overview

The results of the principle experiments for this research, as well as a verification of BSS count rates, are provided in this chapter. The MCNP6 model of the ^{239}PuBe source is compared against the experimental spectrum measured by BSS and unfolded using MAXED software. This comparison further verified the experimental methodology, as well as validated the ability of MCNP6 to accurately model complex neutron spectra. Additionally, the neutron lethargy spectra measured for the steel box and free-field are analyzed against their respective MCNP6 models, and a comparison is performed of the computational and experimental assessments of the steel box NPF. These data represent the culmination of this research effort, one designed to further the verification and validation of MCNP6 for use in RPF assessments of military vehicles.

BSS Count Rate Verification

In order to ensure the veracity of the data collected from the BSS, an initial count rate survey was conducted to verify the results matched those published in literature for this type of detector. The experimental design for this test was identical to that employed during measurements of the neutron spectrum within the steel box. The recorded count rates were normalized based upon the size of the spheres and compared to data published by Mares and Schraube for a neutron source of 2.5 MeV, very similar in energy to the 2.45 MeV neutrons produced in this experiment [29]. Figure 34 provides a comparison of these experimental count rates against those published by Mares and Schraube (1994).

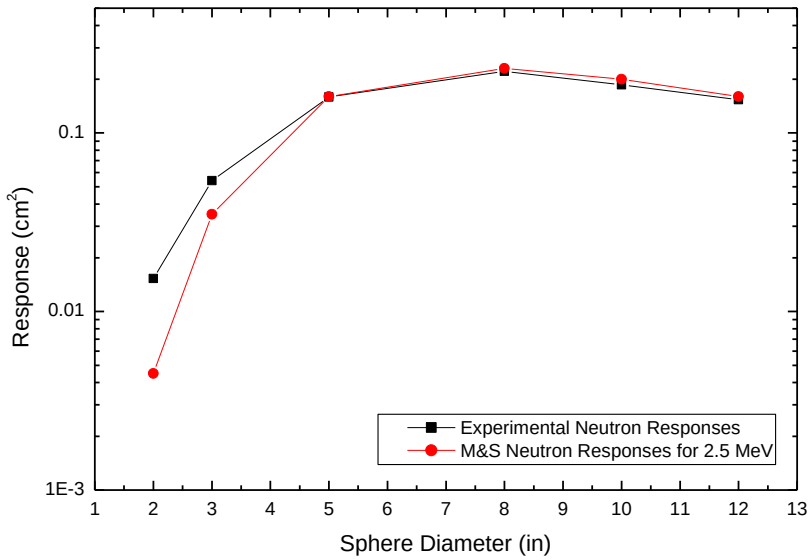

Figure 34. A plot of the initial count rate survey of the BSS compared to data published by Mares and Schraube (1994) [29]. The count rates match closely with notable exceptions for the smaller-diameter spheres. These discrepancies can be largely attributed to the scattering effects of the borated polyethylene shielding which encapsulated the box and accelerator during this experiment.

These measured values appear as expected due to both the difference in incident neutron energies, as well as the presence of shielding material. Specifically, the slightly lower energy source used in the experiment should favor higher responses for the smaller spheres and lower responses in the larger ones. However, the bulk of the discrepancy witnessed from the 2 and 3 inch spheres likely arises from the scattering effects of neutrons off the BP shielding, which encapsulated both the accelerator and the steel box. As expected, the contributions from these lower-energy scattering events diminish for the larger moderating spheres, a feature of the measured data which further supports this explanation of the discrepancy's origin. Based upon this analysis, the BSS was assessed as functioning correctly.

Spectra Results for the ^{239}PuBe Source

MCNP6 Model of the ^{239}PuBe Spectrum

As discussed in the experimental design portion of this paper, the ^{239}PuBe source was modeled at a distance of one meter from the LiI(Eu) detector crystal with an isotropic distribution of neutrons. This configuration resulted in the MCNP6 flux spectrum shown in Figure 35, normalized to one source neutron.

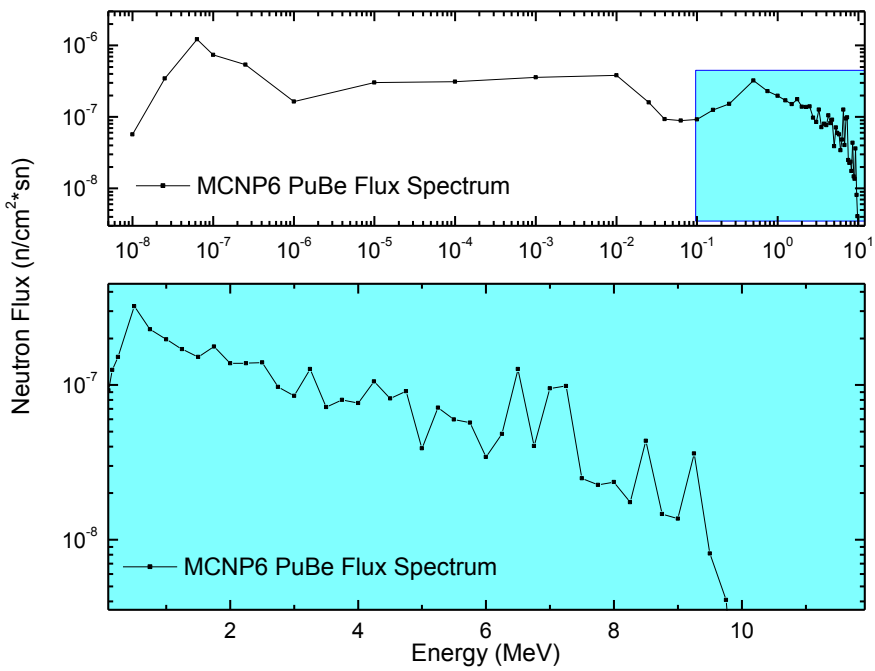

Figure 35. The MCNP6-generated flux spectrum of the AFIT ^{239}PuBe source. This flux spectrum was generated using an extremely simplistic geometry for the source chamber; however, the oscillations at the upper energy levels suggest the fundamental source structures are maintained.

Since MAXED software operates in units of neutron flux, this output spectrum served as the *a priori* data inserted into MAXED for experimental spectrum unfolding. However, to better evaluate the effects of the geometry on neutron scattering, it is often useful to analyze flux in terms of lethargy flux. The lethargy, *U*, of a given neutron is defined as

$$U = \ln\left(\frac{E_o}{E}\right), \tag{5.1}$$

where E is the neutron energy and E_o is the upper neutron energy. This equation is commonly used in nuclear reactor analysis to gauge the average logarithmic energy loss of elastically scattered neutrons [25]. Neutron lethargy flux may be described as

$$\text{Lethargy Flux} = \frac{\phi_g}{U_g} = \frac{\phi_g}{\ln\left(\frac{E_g}{E_{g-1}}\right)} \left(\frac{n}{cm^2 * \Delta U * s}\right). \tag{5.2}$$

This equation normalizes the MCNP6 flux tallies into group fluxes per unit lethargy, which provides values more representative of the number of neutrons recorded at each energy level. Once Equation (5.2) is applied to the MCNP6 flux tally, the resultant spectrum adopts a more conventional shape, as shown in Figure 36, with the largest energy peaks at 6.5 and 7.0 MeV.

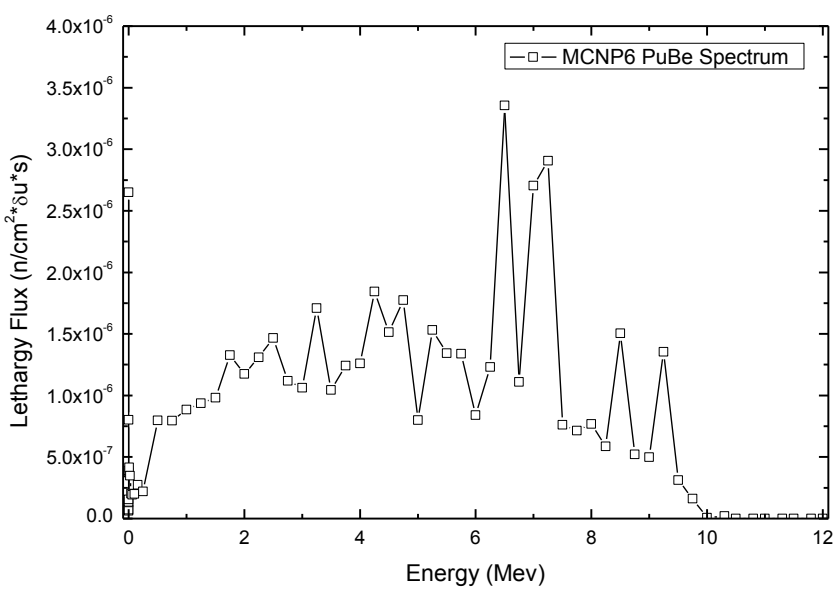

Figure 36. Once the MCNP6-generated flux spectrum is modified to plot in units of lethargy flux, three energy peaks occur at 4 6.5 MeV and 7.0 MeV.

Experimental Results for the ^{239}PuBe Spectrum

Based on the different BSS detector configurations, seven different alpha peaks were recorded using the GammaVision software. Digitally recorded measurements, such as the example provided in Figure 37, enable programs like GammaVision to rapidly calculate the number of counts, count rate, and the associated uncertainty. These data, however, depend greatly upon the user-adopted region of interest (ROI).

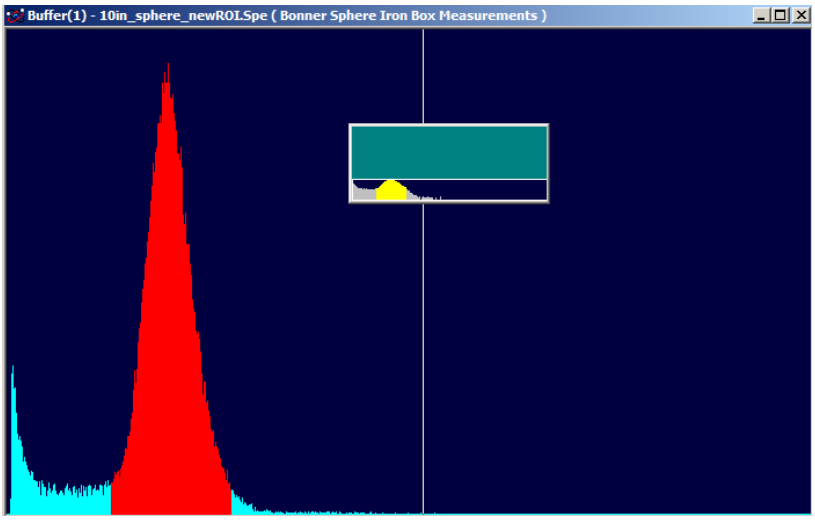

Figure 37. GammaVision output from experimental measurements using a BSS. The large peak on the right-hand side represents the alpha peak, the count distribution associated with the (n,α) absorption reaction in the ^{6}Li crystal.

Based upon the prescribed ROI, the number of counts (N), count rate (*CR*), and absolute uncertainty (σ), for the number of counts were recorded digitally, and pulse processing was later refined. A final width of 270 channels was adopted for every pulse and centered on the channel containing the most counts. Table 12 provides a list of the experimentally recorded results based upon this ROI definition.

Table 12. Experimental measurement values adopted based upon pulse processing from GammaVision. A pulse width of 270 channels was used to capture each pulse.

Detector	N	σ	*CR* (cts/sec)	Channels
Bare	52294	660	5.27	200-470
2in	52192	666	8.77	212-482
3in	52403	663	13.03	217-487
5in	52117	681	18.77	217-487
8in	51036	694	15.97	232-502
10in	50231	712	11.04	229-499
12in	50714	704	8.68	215-485

These recorded count rates are consistent with the expected values published in literature [30, 26]. From these values, count rate error and associated error may be calculated. For each measurement, the fractional uncertainty of the count, N, is equal to the fractional uncertainty of the count rate, CR_{Frac}, which can be determined using

$$CR_{Frac} = \frac{1}{\sqrt{\mathrm{N}}}. \tag{5.3}$$

Due to the high number of net counts for each measurement, these uncertainty values are approximately 0.4% in this experiment; however, MAXED also requires these values input in terms of the absolute error of the count rate, CR_{Abs}. Additionally, the error associated with the subtraction of background counts by GammaVision manifests itself as error in the total area integrated under the alpha peak. This is accounted for as another source of experimental error, *R*, which is provided as fractional error using the equation

$$R = \frac{2(\sigma)}{\mathrm{N}}, \tag{5.4}$$

and these calculations resulted in values ranging from 2% to 3% relative error.

Each value of error described above is required for MAXED spectrum unfolding, and Table 13 provides the consolidated list of experimental data and associated error compiled for the ^{239}PuBe source and input into MAXED for spectrum deconvolution.

Table 13. Final experimental data input into MAXED software for ^{239}PuBe spectrum deconvolution.

Detector	*CR*	CR_{Frac}	CR_{Abs}	*R*
Bare	5.27	0.437	2.305E-02	2.52
2	8.77	0.438	3.839E-02	2.55
3	13.03	0.437	5.692E-02	2.53
5	18.77	0.438	8.222E-02	2.61
8	15.97	0.443	7.069E-02	2.72
10	11.04	0.446	4.926E-02	2.83
12	8.68	0.444	3.854E-02	2.78

Figure 38 provides the MAXED output flux spectrum plotted in units of lethargy flux. The exact values, as well as the associated MAXED output files, are provided in Appendix H.

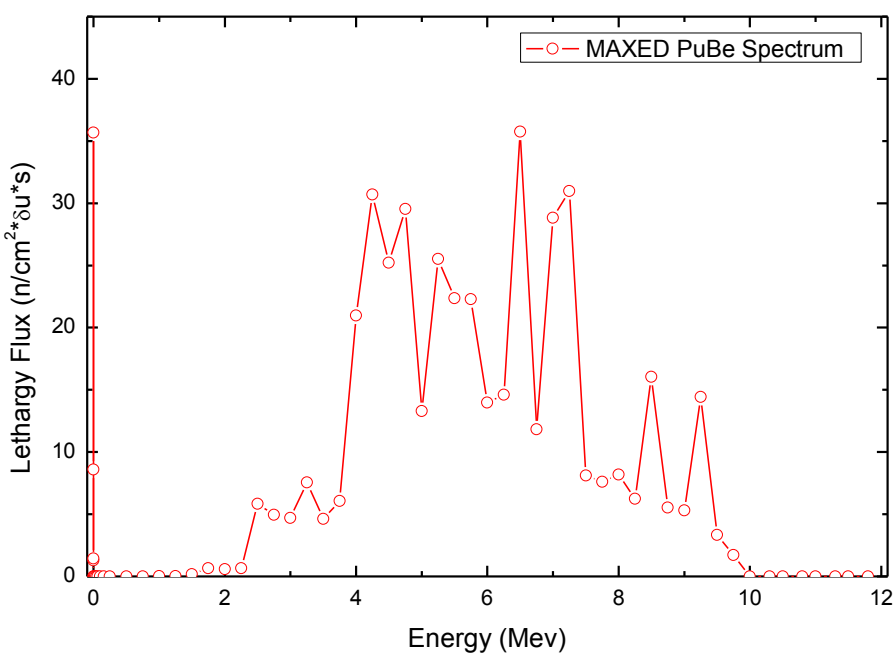

Figure 38. MAXED output of the experimentally measured ^{239}PuBe flux spectrum plotted in units of lethargy flux.

Comparison of the Computational and Experimental ^{239}PuBe Spectra

To maximize the goodness of fit between the experimental and computational ^{239}PuBe spectra, a scaling factor of 1.0×10^7 was applied to the MCNP6 lethargy flux spectrum. A comparison of the two spectra is provided in Figure 39, which demonstrates a strong agreement between the computational and experimental results. Additionally, MAXED returned a χ^2-value of 0.97 per degree of freedom from the spectrum deconvolution. Since any value below 1.0 supports retention of the null hypothesis, this unequivocally supports the significance of this solution spectrum.

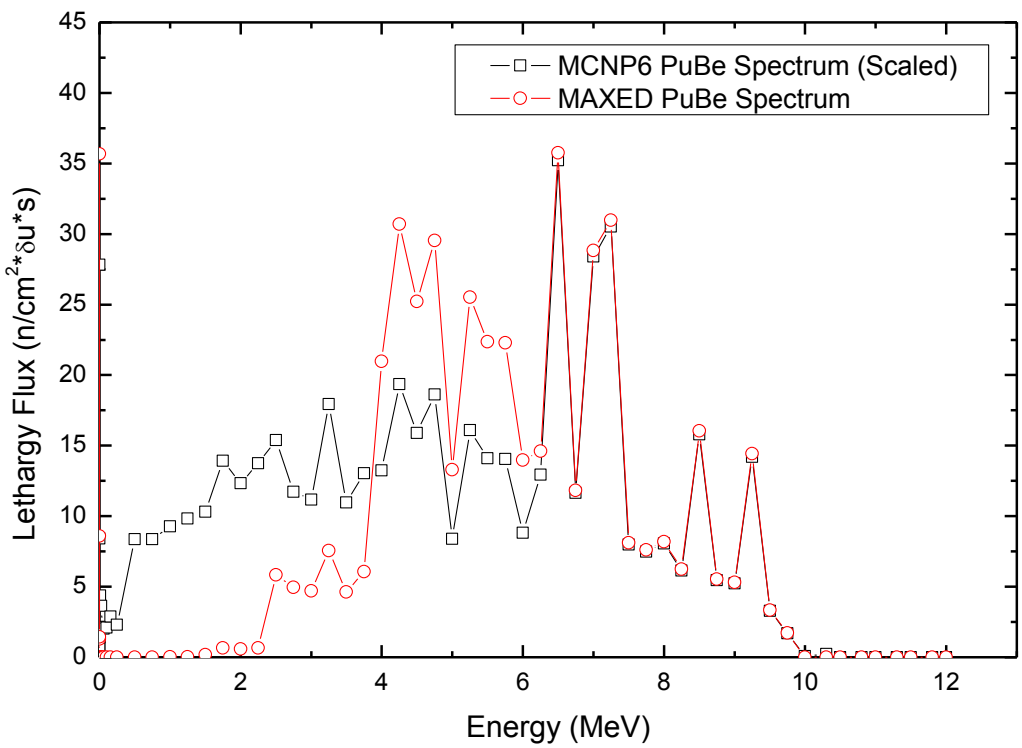

Figure 39. Comparison of the computational and experimentally-determined ^{239}PuBe spectra in units of neutron lethargy flux. The spectra show good structural agreement at energies between 4-6 Mev and excellent agreement at values above 6 MeV.

In other words, the maximum entropy solution generated by MAXED fits the measured BSS data within the documented experimental error, which validates the

experimental methodology for complex neutron spectra. The values of neutron flux estimated by MCNP6 for the ^{239}PuBe source are included in Appendix I.

Spectra Results for the Steel Box

MCNP6 Results for the Steel Box Spectrum

Based upon the model of the AFIT D-D accelerator described earlier, MCNP6 computed the neutron flux spectrum shown in Figure 40. The spectrum appears similar to the one produced by MCNP6 for the ^{239}PuBe source, with a notable lack of high energy oscillations. This is to be expected, since the D-D source is mono-energetic at 2.45 MeV. Sufficient particle tallies were executed to ensure the MCNP6 results passed all ten statistical tests, thereby reducing the relative error of the total flux below 1%. Figure 41 provides a plot of the lethargy flux based upon the MCNP6 spectrum.

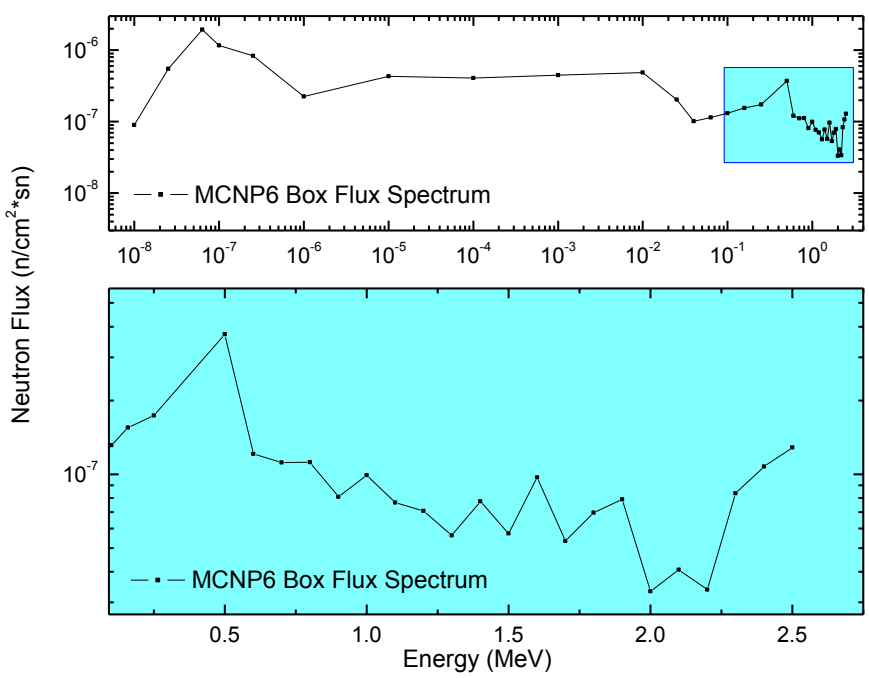

Figure 40. MCNP6 neutron flux spectrum output for BSS measurements using a LiI(Eu) scintillator within the 61 cm sided steel box. This spectrum was computed based upon the configuration of the steel box, detector, and 2.45 MeV D-D accelerator source located in the Building 194 on WPAFB.

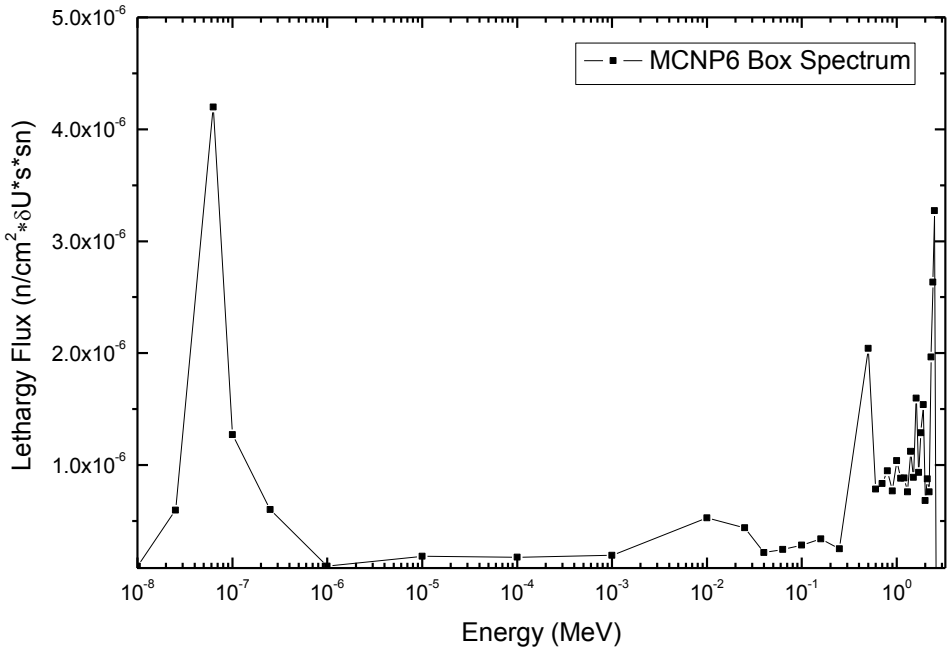

Figure 41. Lethargy flux derived computationally using the flux spectrum from MCNP6. These data are based upon a D-D accelerator source measured within the 61 cm sided steel box and appear reasonable, since significant portions of neutron lethargy appear at thermal and 2.5 MeV energies.

The data presented in Figure 41 appear reasonable due to the significance of the neutron lethargy at both thermal and 2.5 MeV energies. The structures between these two peaks may be characterized as products of the experimental geometry and materials. This includes the high degree of neutron scattering off the BP shielding, as well as neutron scattering due to air. MCNP6 values for neutron flux within the steel box are published in Appendix J.

Experimental Results for the Steel Box Spectrum

Based on the seven separate detector configurations, the different alpha peak measurements were recorded within the steel box using the GammaVision software (see Figure 37 for an example of the output). Just as in the case of the ^{239}PuBe source, the digitally recorded measurements enabled automatic calculations of the count numbers,

count rates, and the associated uncertainties. However, for the steel box measurements, the alpha peak appeared relatively stationary across a set spectrum of channels, so a standard ROI was set from channel 208-608. This provided 400 channels for the GammaVision software to consider for data and error analysis. The final experimental values for the steel box measurements are listed below in Table 14.

Table 14. Experimental measurement recorded within the steel box. The values were based on pulse processing from GammaVision and the adoption of a specific 400 channel ROI applied to each.

Detector	N	σ	*CR* (cts/sec)
Bare	53784	707	11.89
2in	58666	593	67.12
3in	58800	600	150.00
5in	58103	642	270.25
8in	58454	614	248.74
10in	56925	681	165.96
12in	57551	638	107.77

Utilizing these experimental values, the data and associated errors listed in Table 15 were compiled from the steel box measurements and input into MAXED for spectrum unfolding, along with the MCNP6 *a priori* data plotted in Figure 40.

Table 15. Final experimental data input into MAXED for steel box spectrum deconvolution.

Detector	*CR*	CR_{Frac}	CR_{Abs}	*R*
Bare	11.89	0.431	5.127E-02	2.63
2	67.12	0.413	2.771E-01	2.02
3	150.00	0.412	6.186E-01	2.04
5	270.25	0.415	1.121E+00	2.21
8	248.74	0.414	1.029E+00	2.1
10	165.96	0.419	6.956E-01	2.39
12	107.77	0.417	4.492E-01	2.22

Figure 42 displays the MAXED solution spectrum based upon the steel box measurements in units of lethargy flux. The exact values, as well as the associated MAXED output files, are provided in Appendix K.

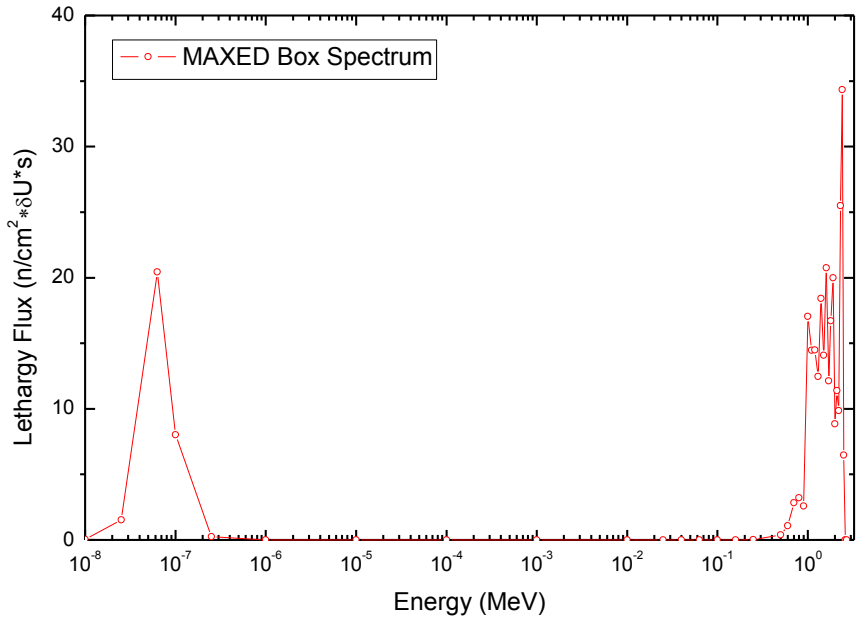

Figure 42. Plot of the lethargy flux derived experimentally from BSS measurements and MAXED spectrum unfolding. These data appear reasonable, since significant portions of the neutron lethargy appears at thermal and 2.5 MeV energies.

As in the case of the ^{239}PuBe lethargy flux spectrum, the MAXED output appears extremely reasonable due to the greatest presence of deposited energy at both thermal and 2.45 MeV energies. These data suggest that the BSS responded correctly to the presence of the neutron flux emitted by the AFIT D-D accelerator.

Comparison of the Steel Box Spectra

Using a scaling factor of 1.0×10^{7}, a comparison of the two lethargy plots can be made visually, as shown in Figure 43. The degree of agreement between the two spectra at both high and low neutron energies demonstrates the accuracy of MCNP6 at modeling particle spectra and interactions with matter.

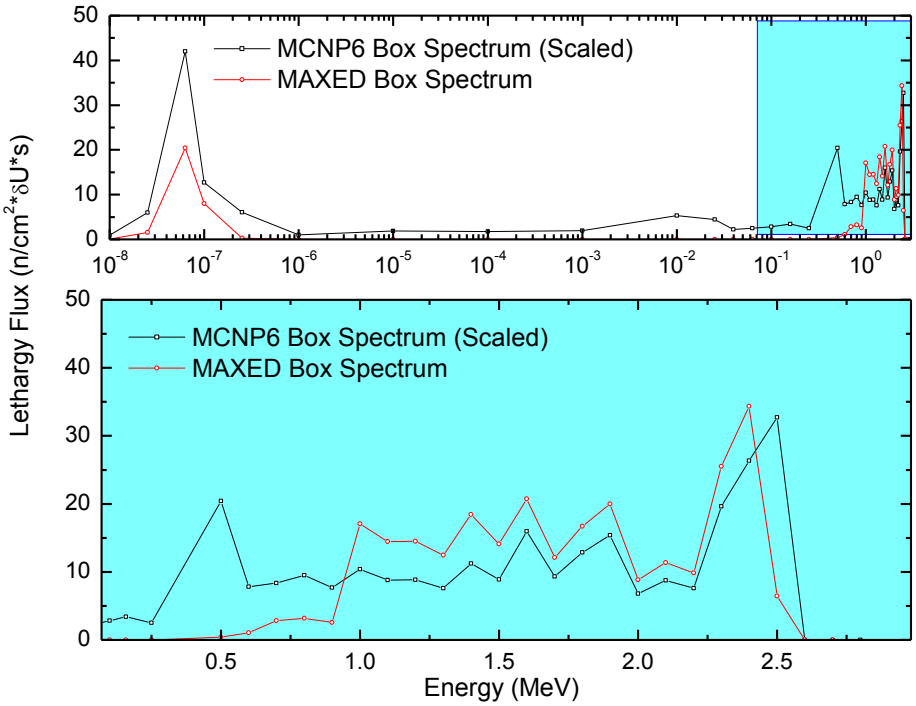

Figure 43. Comparison plot of the computational and experimental lethargy flux spectra. These data are based upon a D-D accelerator source measured within the 61cm sided steel box and appear in good agreement.

Of note, the absence of lethargy flux structures in the MAXED spectrum across the intermediate energy region is indicative of the poor resolution inherent in the BSS for those areas. Therefore, it could be argued that MCNP6 may offer a more accurate lethargy spectrum than that provided by the BSS through MAXED unfolding. Despite this difference in structure, the unfolded MAXED lethargy spectrum agrees with the expected result for experiment, specifically that a greater number of neutrons should be detected at 2.45 MeV than at thermal energies. This result typically occurs when utilizing moderated detectors; however, this does not diminish the possibility that MCNP6 may offer a more accurate neutron lethargy flux spectrum.

Regardless, the MAXED output resulted in a χ^2-value of 0.86 per degree of freedom. As discussed previously, this value strongly supports retention of the null

hypothesis and implies a statistically significant agreement exists between the MAXED-generated solution and the measured data. This result also continues to support MCNP6 as a reliable and accurate source for *a priori* data.

Spectra Results for the Free-Field

MCNP6 Results for the Free-Field Spectrum

Normalized to one source neutron, Figure 44 displays the free-field flux spectrum computed by MCNP6. The spectrum appears very similar to that modeled within the steel box, with the exception that the values for flux are greater in the free-field. This result was expected, since the cross sections for steel provided in Figure 24 suggest a nearly uniform attenuation across the energy region plotted. The values of the free-field neutron spectrum and associated error computed by MCNP6 are provided in Appendix L.

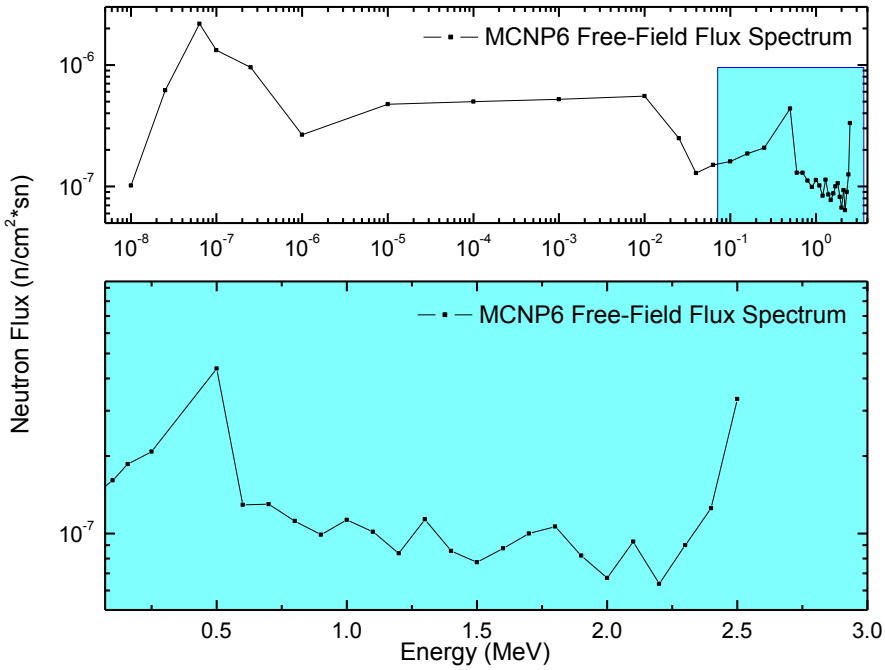

Figure 44. MCNP6 neutron flux spectrum estimate for BSS measurements using a LiI(Eu) scintillator in the free field. This source spectrum was modeled upon a 2.45 MeV D-D accelerator source located in the AFIT Building 194 on WPAFB.

Utilizing the conversion from flux to lethargy flux, as described in Equation (5.2), Figure 45 provides a depiction of the calculated lethargy flux from the MCNP6 free-field computation. Similar to the MCNP6 box spectrum, lethargy appears greatest at thermal and 2.5 MeV energies, which is expected when measuring a D-D accelerator source.

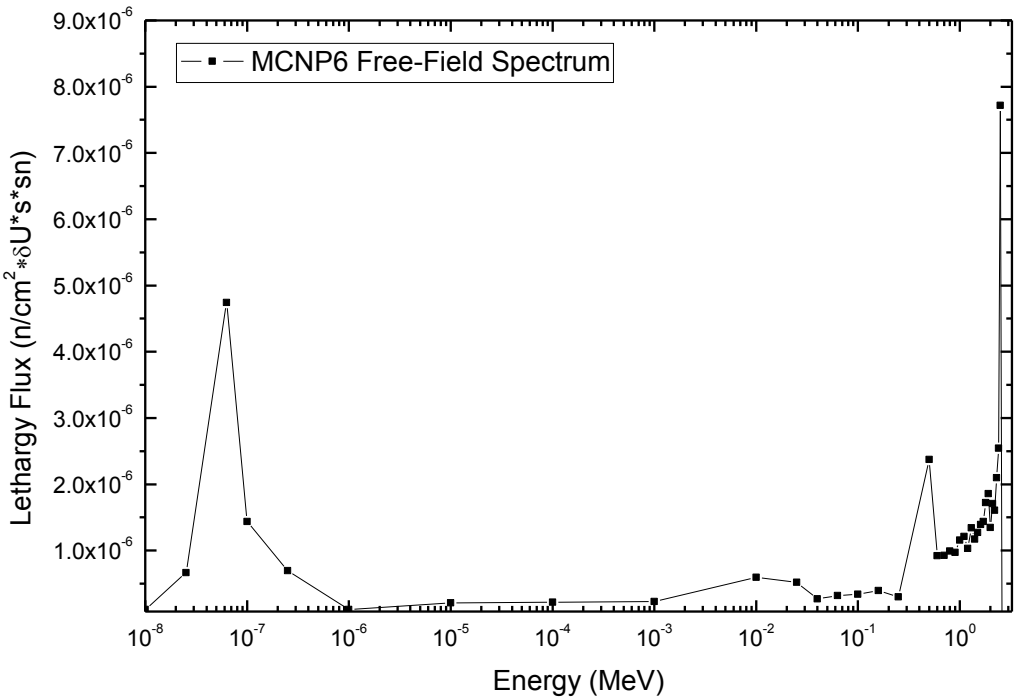

Figure 45. Lethargy flux derived computationally using the free field flux spectrum from MCNP6. These data appear reasonable due to the close similarity with the lethargy spectrum calculated from within the steel box.

Experimental Results for the Free-Field Spectrum

The seven alpha peak measurements of the free-field environment were each recorded using the GammaVision software, which also provided automatic calculations of the count area, count rates, and associated uncertainties. As in the case of the steel box measurements, the alpha peaks recorded for the free-field appeared relatively stationary across a set spectrum of channels. Therefore, a standard ROI was set from channel 225 to channel 525, which provided 300 channels to consider for data calculation and error

analysis. The pertinent values recorded from these measurements of the free-field spectrum are listed below in Table 16.

Table 16. Experimental measurement recorded for the free-field environment. The values were based on pulse processing from GammaVision and utilized a specific 300 channel ROI for each.

Detector	N	σ	*CR* (cts/sec)
Bare	61081	606	21.68
2in	59000	594	98.01
3in	59473	575	209.21
5in	58250	623	360.41
8in	58950	596	338.37
10in	58600	610	241.41
12in	57450	653	157.15

Utilizing these experimental data, the values listed in Table 17 were calculated and input into MAXED for spectrum deconvolution of the free-field neutron flux spectrum.

Table 17. Final experimental data input into MAXED for free-field spectrum deconvolution.

Detector	*CR*	CR_{Frac}	CR_{Abs}	*R*
Bare	21.68	0.431	9.344E-02	1.98
2	98.01	0.413	4.048E-01	2.01
3	209.21	0.412	8.620E-01	1.93
5	360.41	0.415	1.492E+00	2.13
8	338.37	0.414	1.401E+00	2.02
10	241.41	0.419	1.012E+00	2.08
12	157.15	0.417	6.553E-01	2.27

Figure 46 provides the resultant MAXED output for the flux spectrum of the free-field environment in units of lethargy flux. The output data points, as well as the associated MAXED output file, are provided in Appendix M.

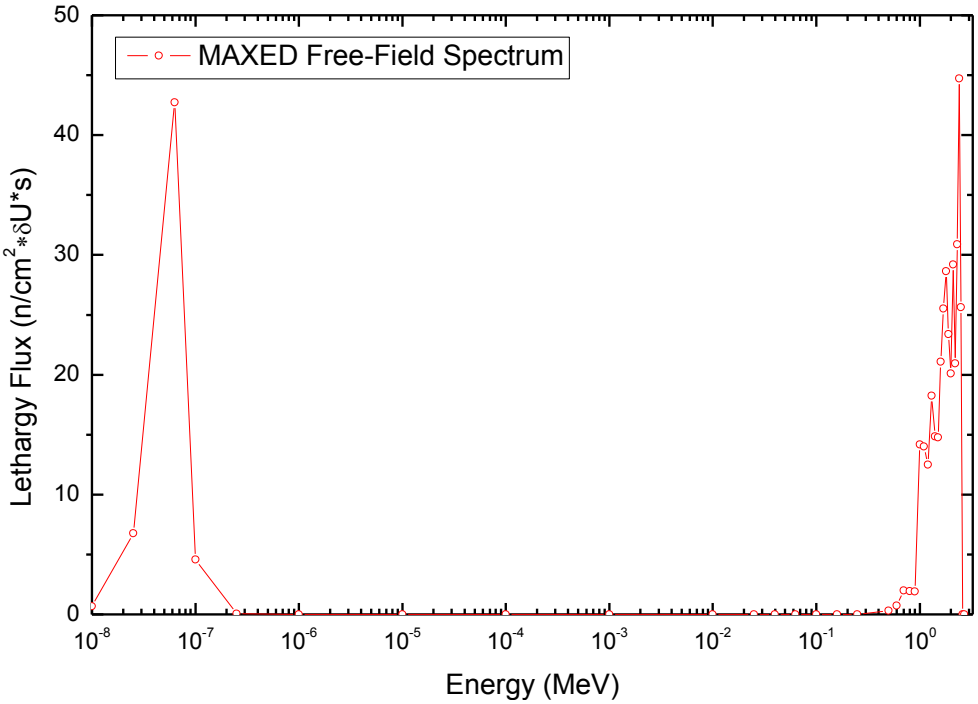

Figure 46. Lethargy flux measured experimentally for the free-field neutron spectrum using BSS measurements and MAXED spectrum unfolding.

Again, the experimentally-derived MAXED solution appears extremely reasonable due to the presence of structures at both thermal and 2.45 MeV energies. This suggests the BSS responded correctly to the presence of the neutron flux emitted by the AFIT D-D accelerator and recorded the neutrons as they down-scattered from 2.45 MeV.

Comparison of the Free-Field Spectra

After scaling by a factor of 5.0×10^{6}, a comparison of both lethargy plots can occur, as shown in Figure 47. This graphic illustrates significant agreement in lethargy flux structure exists across the entire energy range; however, notably discrepancies in intensity are evident between 1 to 2.45 MeV. This can only be attributed to the presence of high-energy neutrons that failed to down-scatter in the manner anticipated by MCNP6. Additionally, the absence of structure in the MAXED spectrum between 1.0×10^{-6} and 0.1

MeV is possibly due to the limited resolution of the BSS. As discussed earlier, this may imply MCNP6 provides a more accurate spectrum in this region; however, more analysis must occur to explain the slight discord of intensity evident at the higher energy levels. Despite these differences, the spectra are in clearly otherwise in agreement.

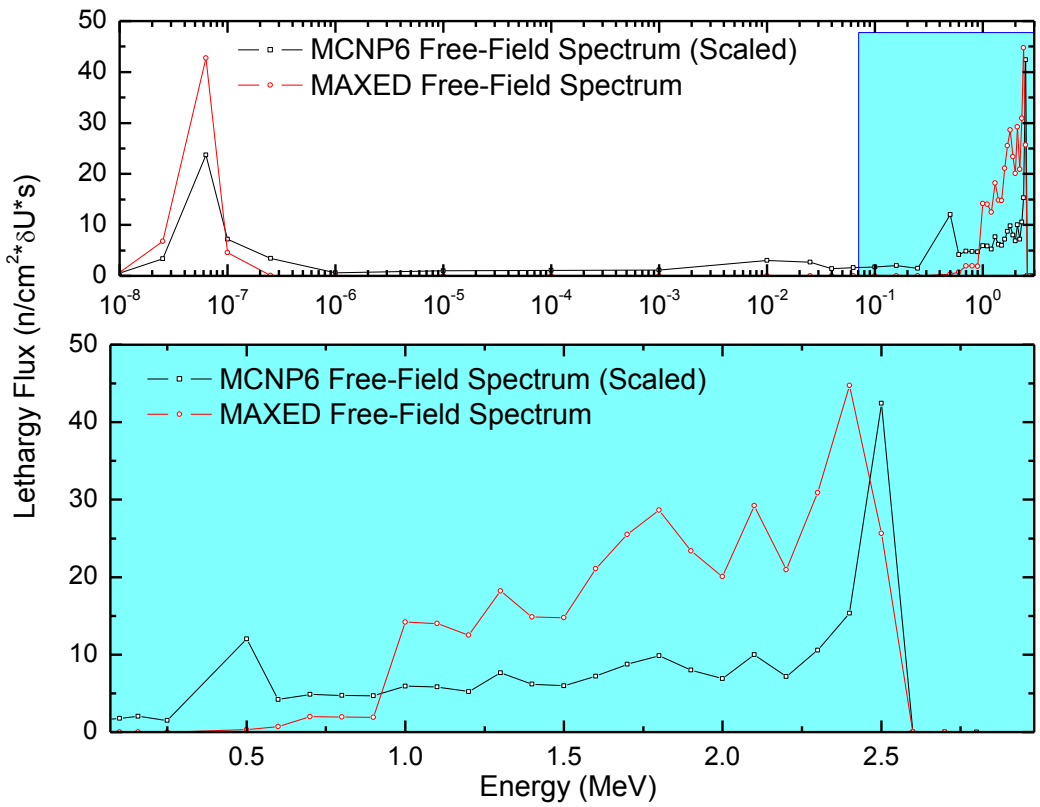

Figure 47. Comparison of the computational and experimental lethargy flux spectra for the free-field environment. These data are based upon a D-D source and appear in good, overall agreement.

For the free-field spectrum unfolding, MAXED provided a χ^2-value of 0.91 per degree of freedom, indicating the retention of the null hypothesis and a statistically significant agreement with the recorded measurements and *a priori*. This result continues to validate the use of MAXED and MCNP6 as reliable and accurate computational tools for measuring neutron flux. At this point in the research, an evaluation of the experimental versus computational NPF assessments can finally occur.

NPF Comparison Using Experimental and Computational Data

This final section addresses the calculation of the steel box NPF based upon the previously discussed computational and experimental results. Ultimately, these final numbers carry the greatest importance in determining whether MCNP6 provides accurate assessments for RPF upon which future applications for military vehicles might be based.

In order to accomplish this task, each calculated flux spectra must be converted into an ambient dose equivalent (*H*(10)*) value consistent with the provisions established by the International Commission on Radiological Protection (ICRP). *H*(10)* is defined as the dose equivalent for each point in an expanding and aligned radiation field that would be measured at a depth of 10 mm within an International Commission on Radiological Units (ICRU) sphere of tissue-equivalent material [34]. This definition, however, is a bit of a misnomer due to the assumption of "unidirectional flux," which itself is a contradiction, since flux is a quantity devoid of individual particle directionality. Furthermore, the flux energy distribution is considered consistent for both the radiation field and the point of *H*(10)* measurement, which implies that *H*(10)* is the dose a person would receive at a specific location had they not been present in the first place. Nevertheless, *H*(10)* still represents the best estimate for the expected dose from radiation and is described in special units of Sieverts (Sv), which represent J/kg [35].

The conversion from particle flux to *H*(10)* is accomplished via the equation

$$H^*(10)(E_i) = h_\phi(E_i)\phi(E_i)\,, \tag{5.5}$$

where $h_\phi(E_i)$ represents the ambient dose equivalent conversion factor, or weighting, of the radiation per energy bin, E_i. More specifically, $h_\phi(E_i)$ is defined as a function of the radiation's biological effects, both direct and indirect, when absorbed as a dose in human tissue [35]. Therefore, for *n* number of energy bins, this implies that the total ambient dose equivalent from a neutron flux spectrum can be determined as the sum of all the component doses, or

$$H^*(10) = \sum_{i=1}^{n} H^*(10)(E_i)\Delta E_i \ . \tag{5.6}$$

Calculated values for $h_\phi(E_i)$ published in 2005 by Veinot and Hertel [35] were used in this experiment to convert the measured neutron flux spectra into *H*(10)* in units of pSv cm^2. These conversion coefficients incorporate the most recent guidance provided by the ICRP Publication 60 and the ICRU Report 49, based upon tissue-equivalent materials.

Using these coefficients, the flux spectra for both the steel box and free field were re-binned to align with the flux bin widths published by Veinot and Hertel (2005). In doing so, flux values were summed in instances where more than one flux bin fell within the coefficient bins prescribed by the authors. This provided a total flux for the entire coefficient bin prior to multiplication of the conversion value and final *H*(10)* summation, as per Equation (5.6). Similarly, values of relative error provided by MCNP6 for each energy bin were propagated using every level within each coefficient bin before multiplication by the conversion value. To reduce the associated uncertainty of this final calculation, the MCNP6 spectra were refined using larger particle tallies,

which are provided in Appendix N. These values of absolute error for each energy bin were subsequently summed to provide the total *H*(10)* absolute error for each MCNP6 spectrum. Unfortunately, MAXED software does not produce relative error estimates for maximum entropy solutions. Consequently, for the purposes of error analysis, a conservative estimate of 10% relative error was applied to the both experimental calculations of *H*(10)* derived using the MAXED solution spectra.

Both MCNP6 and MAXED-generated flux spectra were evaluated using this methodology, and the total ambient dose equivalent results are provided in Table 18. Of note, the *H*(10)* values for the MCNP6 box and free-field spectra are calculated in values of pSv cm^2 per source neutron because MCNP6 computes flux spectra normalized to one source neutron.

Table 18. *H*(10)* results for each spectra measured in the experiment, including calculations of absolute error, *ε*. MAXED values are in units of pSv cm^2, while MCNP6 values are in pSv cm^2/ sn.

Method	Box		Free-Field	
	H(10)*	*ε*	*H*(10)*	*ε*
MAXED	7.474E+03	7.474E+02	9.505E+03	9.505E+02
MCNP6	9.796E-04	1.598E-04	1.236E-03	1.886E-04

Utilizing Equation (1.2), final calculations for the NPF of the steel box are now possible for both the computational and experimental results. Additionally, using the equations for error propagation provided in Knoll [22], final uncertainties can also be calculated for these results. For both the MAXED and MCNP6 *H*(10)* values, units cancel and result in the ratios provided in Table 19.

Table 19. NPF ratios for both the computational (MCNP6) and experimental (MAXED) results.

Method	NPF ± *ε*
Experimental (BSS and MAXED)	1.272 ± .18
Computational (MCNP6)	1.262 ± .28

These final assessments of the steel box NPF differ by a relative error of less than 1%, well within the associated error for both results. Based upon past research, where comparisons of RPF values typically fluctuated between 20% to 50% [6, 8, 10], these results demonstrate an exceptionally high degree of accuracy on the part of MCNP6 in modeling this important relationship. Furthermore, by utilizing a NPF based on statistically significant MAXED-generated flux spectra, the MCNP6-derived NPF assessment may be considered significantly close to the true NPF value.

The slightly higher value of NPF derived from the MAXED solution spectra may be attributed to the poor resolution of the BSS across intermediate energy levels. As addressed earlier, the failure of the BSS to replicate many of the flux structures across that energy region, as witnessed in all MCNP6 and MAXED spectra comparisons, may help explain the slight discrepancy in the final results of NPF. Although largely speculation at this point, the possibility exists that MCNP6 may provide a more accurate estimate of NPF than achievable through BSS measurement.

Regardless of the source of relative error, the clear demonstration that statistically significant agreement exists between NPF ratios derived via experimentation and MCNP6 computation unequivocally supports further research into validating MCNP6 for RPF assignment. The research described herein initiates that process by definitively proving the validity of using MCNP6 to estimate NPF values for simplified geometries and materials. Despite this progress, however, a great deal more research must now occur.

VI. Conclusions

The results from each component of this research support further investigation into the validation of MCNP6 for assigning RPF values to military vehicles. Using a benchmark experiment from 1984, MCNP6 successfully replicated the neutron flux spectra from a mono-energetic 14.1 MeV source measured both within and surrounding a hollow iron box. The computational and experimental estimates of NPF, based upon the flux spectra, differed fractionally by less than 5%, which indicated a significant agreement existed between the results.

Additionally, the application of MCNP6 to generate updated BSS response functions, which are required for MAXED spectral deconvolution, likewise produced statistically significant agreement with published data. MCNP6 was also utilized to characterize the complex neutron emissions from a 4.78 Ci ^{239}PuBe source, returning a spectrum validated by BSS measurements and MAXED unfolding.

Lastly, the code was also implemented for estimations of the neutron flux spectra present within a steel box and for the free-field using a mono-energetic neutron flux emitted by a D-D neutron accelerator. As in the case of the ^{239}PuBe source, both solution spectra were validated as statistically significant through χ^2 analysis with MAXED unfolding. Using *H*(10)* conversion coefficients, calculations for the measured NPF of the steel box returned values with less than 1% variation from those computed by MCNP6. These results, therefore, verify and validate MCNP6 computations of neutron flux, as well as subsequent assessments of NPF for simple geometries and materials.

Despite the strength of these results, the challenge inherent in validating MCNP6 for RPF assessments of military vehicles remains complex and lengthy. Although this paper supports the use of MCNP6 in determining NPF, future research into different forms of radiation, such as gamma rays, must also transpire. Furthermore, the simple geometry and materials incorporated in this research limit the extrapolation of these results. Therefore, although these findings appear promising, future experiments to further validate MCNP6 must now take place.

Future research efforts, for example, may incorporate more complex geometries, such as large, compartmentalized boxes more similar to internal vehicle spaces. Additionally, other experiments incorporating a more complex set of materials must also be employed. Such materials could be expected to more closely approximate the density and radiation response characteristics of materials commonly used in military vehicle design, such as ballistic shielding. Lastly, future research must expand beyond just the neutron flux; it must incorporate both neutron and gamma contributions to *H*(10)*. Only after rigorous investigation into these and other areas is concluded will a final validation of MCNP6 occur for the purposes of RPF assessment.

In conclusion, to accomplish the ultimate objective of MCNP6 validation for RPF assessment, experimental and computational methods must both be applied to many different problems simultaneously. This research represents the first small step in this effort by validating MCNP6 for NPF assessment using simple geometries and materials. Future efforts, therefore, must build off these important results and expand upon the validated methodology described herein.

Appendix A. MCNP6 Input Cards for Benchmark Experiment

MCNP6 Input Card (Iron Box)

```
c cell cards
100     1     -0.001205  -10 20 50 imp:n=1          $ air in world (rpp)
200     2     -7.82      -20 30  imp:n=1            $ iron shield (rpp)
300     1     -0.001205  -30 40  imp:n=1            $ air in shielded box
400     3     -0.96      -40     imp:n=1            $ detector
500     2     -7.82      -50     imp:n=1            $ tower platform
999     0                 10     imp:n=0            $ rest of the world

c surface cards
10   rpp   0 40500   -250 250   0 500              $ problem bounding surface
20   rpp   40200  40261   -30.5 30.5  169.5 230.5  $ steel box
30   rpp   40202.5 40258.5   -28 28   172 228      $ air inside steel box
40   s     40230.5 0 200 15.25                      $ detector sphere, r=15.25
50   rpp   40195  40266   -35.5 35.5  167.5 169.4999 $ steel tower top

c material specification
m1   07014 0.8   8016 0.2                           $ air
m2   26000 0.977170  6012  0.022831                 $ shield, carbon steel
m3   01001 -0.09677   6012 -0.38710   8016 -0.51613 $ polyethylene
mode n
SDEF POS=.01 0 200 AXS=1 0 0 EXT=0 RAD=d1           $ monodirectional disk source, r=15.25
     PAR=n ERG=14 VEC=1 0 0 DIR=1  ARA=730
SI1  0.0 15.25
SP1 -21 1
nps 50000000                                        $ number of neutrons generated (50 million)
f4:n 400                                            $ flux area detector, cell 400 (detector)
e4   1.0E-09 4.14E-07 1.23E-06 3.06E-06 1.171E-05 2.9E-05
     1.01E-04 5.8E-04 1.23E-03 3.35E-03 .0103 .0219 .0248
     0.0525 0.111 0.1579 0.55 1.11 1.83 2.31 2.39 3.01 4.07
     4.72 4.97 6.38 7.41 8.19 9.05 10 11.1 12.2 12.8 13.8
     14.2 14.9 16.9 19.6
```

MCNP6 Input Card (Free-Field)

```
c cell cards
100     1     -0.001205  -10 20 30 imp:n=1          $ air in world (rpp)
200     3     -0.96      -20     imp:n=1            $ area (rpp)
300     2     -7.82      -30     imp:n=1            $ air in shielded box
999     0                 10     imp:n=0            $ rest of the world

c surface cards
10   rpp   0 40500   -250 250   0 500              $ problem bounding surface
20   s     40230.5 0 200 15.25                      $ detector sphere, r=15.25cm
30   rpp   40195  40266   -35.5 35.5  162.5 165    $ steel tower top

c material specification
m1   07014 0.784   8016 0.216                       $ air
m2   26000 0.977170  6012  0.022831                 $ shield, carbon steel
m3   01001 -0.09677   6012 -0.38710   8016 -0.51613 $ polyethylene
mode n
SDEF POS=.01 0 200 AXS=1 0 0 EXT=0 RAD=d1           $ monodirectional disk source
     PAR=n ERG=14 VEC=1 0 0 DIR=1  ARA=730
SI1  0.0 15.25
SP1 -21 1
nps 50000000                                        $ number of neutrons generated
f4:n 200                                            $ flux area detector, cell 200 (detector)
e4   1.0E-09 4.14E-07 1.23E-06 3.06E-06 1.171E-05 2.9E-05
     1.01E-04 5.8E-04 1.23E-03 3.35E-03 .0103 .0219 .0248
     0.0525 0.111 0.1579 0.55 1.11 1.83 2.31 2.39 3.01 4.07
     4.72 4.97 6.38 7.41 8.19 9.05 10 11.1 12.2 12.8 13.8
     14.2 14.9 16.9 19.6
```

Appendix B. MCNP6 Neutron Spectra Results for Benchmark Experiment

Energy (MeV)	Box Flux Spectrum	Free-Field Flux Spectrum
1.00000E-09	6.3270E-10	8.2874E-10
4.14000E-07	8.9916E-07	1.1735E-06
1.23000E-06	2.6023E-08	3.3486E-08
3.06000E-06	2.1620E-08	2.7863E-08
1.17100E-05	3.2219E-08	4.1482E-08
2.90000E-05	2.2283E-08	2.8685E-08
1.01000E-04	3.1225E-08	4.0081E-08
5.80000E-04	4.5136E-08	5.7938E-08
1.23000E-03	2.0125E-08	2.5833E-08
3.35000E-03	2.7296E-08	3.5104E-08
1.03000E-02	3.2130E-08	4.1190E-08
2.19000E-02	2.3180E-08	3.0109E-08
2.48000E-02	3.9889E-09	5.1931E-09
5.25000E-02	2.6484E-08	3.4227E-08
1.11000E-01	3.2398E-08	4.1615E-08
1.57900E-01	1.8423E-08	2.4038E-08
5.50000E-01	9.7046E-08	1.2436E-07
1.11000E+00	9.3281E-08	1.1955E-07
1.83000E+00	9.3470E-08	1.2242E-07
2.31000E+00	5.3455E-08	7.2065E-08
2.39000E+00	9.2775E-09	1.2593E-08
3.01000E+00	6.2210E-08	8.4996E-08
4.07000E+00	8.0105E-08	1.1185E-07
4.72000E+00	4.2492E-08	5.9202E-08
4.97000E+00	1.6537E-08	2.3087E-08
6.38000E+00	8.7435E-08	1.2615E-07
7.41000E+00	6.7817E-08	9.7329E-08
8.19000E+00	4.0551E-08	5.8856E-08
9.05000E+00	4.3592E-08	6.3242E-08
1.00000E+01	4.6686E-08	6.8004E-08
1.11000E+01	5.3822E-08	7.8952E-08
1.22000E+01	6.4561E-08	9.2157E-08
1.28000E+01	4.7768E-08	6.8771E-08
1.38000E+01	1.2803E-07	1.8342E-07
1.42000E+01	1.1336E-06	1.6572E-06
1.49000E+01	0.0000E+00	0.0000E+00
1.69000E+01	0.0000E+00	0.0000E+00

Appendix C. MAXED Results for the Benchmark Experiment

Free-Field MAXED Unfolding Results:

```
Deconvolution Using the MAXED (Maximum Entropy) Algorithm
=========================================================

File with Input Data :  024_Exp.ibu

File with Default Spectrum         :  c:\U_M_G\FC\$inp\def_spec\ExpSp_1.flu
Default Spectrum Fluence Format    : fluence rate per bin
Energy of Default Sp.  in Units of : MeV

File with Response Function        :  c:\U_M_G\FC\$inp\response\NRF_Exp.fmt
Response Functions     in Units of :     cm^2
Energy of Final Spect. in Units of : MeV

Chi-squared P.D.F. Using the Default Spectrum     = ********
Final Chi-squared P.D.F.                          =  111.576
NOTE: Chi-squared Per Degree of Freedom was set to:    1.700


*** RESULTS FOR THE FINAL SPECTRUM: ***

     DN              M             C      (C-M)/S      (C-M)/M
      1   2.120000E-12  3.268910E-12    18.38306      0.54194
      2  -4.740000E-13  4.675016E-13    -0.34096     -0.01371
      3   4.320000E-12  4.377028E-12     0.65274      0.01320
      4   6.690000E-12  5.778853E-12    -6.73443     -0.13620
      5   8.650000E-12  7.327899E-12   -12.50931     -0.15284
      6   7.170000E-12  5.969262E-12   -12.50868     -0.16747
      7   5.440000E-12  4.902297E-12    -7.56553     -0.09884
      8   4.060000E-12  3.719001E-12    -5.20884     -0.08399

Note 1: DN = detector number
        M = measured count rate
        C = calculated count rate
        S = estimated standard uncertainty
Note 2: M<0 indicates data not used for the deconvolution
```

Iron Box MAXED Unfolding Results:

```
Deconvolution Using the MAXED (Maximum Entropy) Algorithm
=========================================================

File with Input Data :  026_Exp.ibu

File with Default Spectrum         :  c:\U_M_G\FC\$inp\def_spec\ExpSp_1.flu
Default Spectrum Fluence Format    : fluence rate per bin
Energy of Default Sp.  in Units of : MeV

File with Response Function        :  c:\U_M_G\FC\$inp\response\NRF_Exp.fmt
Response Functions     in Units of :     cm^2
Energy of Final Spect. in Units of : MeV

Chi-squared P.D.F. Using the Default Spectrum     = ********
Final Chi-squared P.D.F.                          =  127.108
NOTE: Chi-squared Per Degree of Freedom was set to:    0.810


*** RESULTS FOR THE FINAL SPECTRUM: ***

     DN              M             C      (C-M)/S      (C-M)/M
      1   7.490000E-13  1.333060E-12    26.45109      0.77979
      2   4.070000E-13  2.396624E-13   -10.22515     -0.41115
      3   2.370000E-12  2.264767E-12    -2.19555     -0.04440
      4   5.210000E-12  4.422584E-12    -7.47317     -0.15114
      5   9.080000E-12  8.075838E-12    -9.05113     -0.11059
      6   7.180000E-12  6.677290E-12    -5.22968     -0.07002
      7   4.880000E-12  5.208677E-12     5.15519      0.06735
      8   3.610000E-12  3.846323E-12     4.01677      0.06546
```

MAXED Unfolded Spectra

Energy (MeV)	Box Flux Spectrum	Free-Field Flux Spectrum
1.00000E-09	1.4008E-07	3.8311E-06
4.14000E-07	2.1635E-07	3.3882E-08
1.23000E-06	2.3965E-07	1.5844E-07
3.06000E-06	1.1143E-07	6.2129E-08
1.17100E-05	5.7355E-07	2.8043E-07
2.90000E-05	4.4668E-08	1.6642E-07
1.01000E-04	2.8555E-09	2.1388E-08
5.80000E-04	5.1538E-10	1.6461E-10
1.23000E-03	6.4133E-11	8.1266E-10
3.35000E-03	1.2620E-11	1.1184E-10
1.03000E-02	8.1453E-12	4.0959E-11
2.19000E-02	3.0584E-12	1.3422E-11
2.48000E-02	7.4895E-12	1.6850E-11
5.25000E-02	8.5763E-12	1.0285E-11
1.11000E-01	1.5124E-11	1.7410E-11
1.57900E-01	4.9320E-12	5.0689E-12
5.50000E-01	1.4404E-11	9.4543E-12
1.11000E+00	1.1478E-12	5.8373E-12
1.83000E+00	2.2411E-13	5.0445E-12
2.31000E+00	1.0420E-12	2.9124E-11
2.39000E+00	5.6424E-14	2.1773E-12
3.01000E+00	1.5927E-14	3.0713E-13
4.07000E+00	2.9917E-14	3.2364E-13
4.72000E+00	9.6718E-14	7.2244E-13
4.97000E+00	2.7537E-14	9.2936E-14
6.38000E+00	2.2213E-13	4.8569E-13
7.41000E+00	2.3281E-13	4.7745E-13
8.19000E+00	5.4672E-13	8.6561E-13
9.05000E+00	1.1132E-12	1.2484E-12
1.00000E+01	1.8059E-12	1.9153E-12
1.11000E+01	2.3696E-12	2.7835E-12
1.22000E+01	4.6190E-12	5.9972E-12
1.28000E+01	2.3420E-12	3.3191E-12
1.38000E+01	5.0894E-12	7.7600E-12
1.42000E+01	2.6184E-12	4.2162E-12
1.49000E+01	2.0946E-36	3.5585E-36
1.69000E+01	0.0000E+00	0.0000E+00

Appendix D. MCNP6 Input Cards for BSS Response Functions

MCNP6 Card for the Bare Scintillator

```
c Based on Mares and Schraube (1994)
c cell cards
100     0                   -10 20     imp:n=1          $ Vaccuum in world (rpp)
200     2     -2.6989       -20 30     imp:n=1          $ Aluminum tube
300     0                   -30 40     imp:n=1          $ Vaccuum for the PMMA light pipe
400     1     -3.84         -40        imp:n=1          $ LiI(Eu) detector, modeled
999     0                    10        imp:n=0          $ Rest of the world (void)

c surface cards
10   rpp   0 100 -50 50   0 100                         $ Problem bounding surface
20   rcc   50 0 49.2  0 0 1.6  0.635                    $ Al rcc (perpendicular to beam)
30   rcc   50 0 49.4  0 0 1.2  0.535                    $ Vaccuum within the Al cylinder
40   rcc   50 0 49.8  0 0 0.4  0.2                      $ LiI(Eu) crystal (RCC r=2mm, ht=4mm)

c material specification
m1   03006.70c -0.0518  53127.70c -0.9482               $ LiI crystal composition
m2   13027.70c -1.0000                                  $ Al metal
mode n
SDEF POS=0.01 0 50 X=0 Y=d1 Z=d2                        $ Source Energy Distribution
     PAR=n ERG=1.0000E-08 VEC=1 0 0 DIR=1
SI1  -0.2 0.2
SP1  0 1
SI2  49.8 50.2
SP2  0 1
nps  300000                                             $ Number of neutrons generated
f4:n 400                                                $ Flux average in cell 500
FM4 (1.4e-4 1 105)                                      $ FM tally multiplier for (n,t) rxn in m3
```

MCNP6 Card for the 12 in Moderator Sphere

```
c cell cards
100     0                   -10 20     imp:n=1          $ Vaccuum in world (rpp)
200     3     -0.95         -20 21     imp:n=1          $ Poly Bonner Sphere
210     3     -0.95         -21 22     imp:n=4
220     3     -0.95         -22 23     imp:n=13
230     3     -0.95         -23 24     imp:n=82
240     3     -0.95         -24 25     imp:n=405
250     3     -0.95         -25 30     imp:n=1500
300     2     -2.6989       -30 40     imp:n=12000      $ Aluminum tube
400     0                   -40 50     imp:n=3000       $ Vaccuum in the tube
500     1     -3.84         -50        imp:n=50000      $ LiI(Eu) detector, modeled
999     0                    10        imp:n=0          $ Rest of the world (void)

c surface cards
10   rpp   0 100 -50 50   0 100                         $ Problem bounding surface
20   s     50 0 50  15.24                               $ Polyethelene spheres
21   s     50 0 50  12.7
22   s     50 0 50  10.15
23   s     50 0 50  6.35
24   s     50 0 50  3.81
25   s     50 0 50  2.54
30   rcc   49.2 0 50  1.6 0 0  0.725                    $ Al rcc (parallel to beam)
40   rcc   49.4 0 50  1.2 0 0  0.525                    $ Vaccuum in the Al cylinder
50   rcc   49.8 0 50  0.4 0 0  0.2                      $ LiI(Eu) crystal (RCC r=2mm, ht=4mm)

c material specification
m1   03006.70c -0.0518  53127.70c -0.9482               $ LiI crystal composition
m2   13027.70c -1.0000                                  $ Al metal
m3   01001.70c -0.143716 06012 -0.856284                $ Polyethylene
mode n
SDEF POS=0.01 0 50 AXS=1 0 0 EXT=0 RAD=d1               $ Source Energy Distribution
     PAR=n ERG=1.0000E-08 VEC=1 0 0 DIR=1  ARA=729.65
SI1  0.0 15.24
SP1 -21 1
nps  300000                                             $ Number of neutrons generated
f4:n 500                                                $ Flux average in cell 500
MT3 poly.10t                                            $ S(a,B) treatment for hydorgen in polyethylene
FM4 (0.6386 1 105)                                      $ FM tally multiplier for (n,t) rxn in m3 (LiI(Eu))
```

Appendix E. MCNP6-Generated BSS Response Functions

Energy Bins	Bare		2in		3in		5in		8in		10in		12in	
MeV	Response	ε	Response	ε	Response	ε	Response	ε	Response	ε	Response	ε	Response	ε
1.0000E-08	7.3079E-02	0.002	3.9907E-02	0.0096	3.0120E-02	0.0182	1.4466E-02	0.0264	3.9099E-03	0.0293	1.5028E-03	0.0287	5.4037E-04	0.0307
2.5120E-08	7.2247E-02	0.002	5.0502E-02	0.0086	3.7938E-02	0.0164	1.8854E-02	0.0237	4.8771E-03	0.0262	1.7580E-03	0.0258	6.3944E-04	0.0286
6.3100E-08	6.9844E-02	0.002	6.7800E-02	0.0075	4.9911E-02	0.0145	2.4279E-02	0.021	6.6752E-03	0.0229	2.4578E-03	0.0223	9.2014E-04	0.0243
1.0000E-07	6.7591E-02	0.002	8.0872E-02	0.0069	6.2956E-02	0.0129	3.0806E-02	0.0189	7.8552E-03	0.0208	3.0184E-03	0.0203	1.1243E-03	0.0223
2.5120E-07	6.0182E-02	0.002	9.9750E-02	0.0062	8.3796E-02	0.0114	4.1107E-02	0.0164	1.0667E-02	0.0178	4.1487E-03	0.0174	1.5283E-03	0.019
1.0000E-06	4.3725E-02	0.001	1.1346E-01	0.0058	1.1199E-01	0.0099	5.8339E-02	0.0143	1.5337E-02	0.0152	5.8363E-03	0.0148	2.1413E-03	0.016
1.0000E-05	1.8752E-02	8E-04	1.0142E-01	0.006	1.2641E-01	0.0094	7.9836E-02	0.0126	2.1662E-02	0.0131	8.1576E-03	0.0126	2.8637E-03	0.0138
1.0000E-04	6.5833E-03	7E-04	7.5804E-02	0.0068	1.2023E-01	0.0097	9.1061E-02	0.0121	2.6479E-02	0.0121	1.0171E-02	0.0116	3.6882E-03	0.0124
1.0000E-03	2.1499E-03	6E-04	5.1565E-02	0.0082	1.0374E-01	0.0104	9.6819E-02	0.0117	3.0960E-02	0.0115	1.1985E-02	0.0108	4.4421E-03	0.0115
1.0000E-02	6.9408E-04	6E-04	3.3684E-02	0.0101	8.6471E-02	0.0114	1.0263E-01	0.0116	3.7088E-02	0.0107	1.4779E-02	0.01	5.3334E-03	0.0107
2.5120E-02	4.4962E-04	6E-04	2.8196E-02	0.011	7.9456E-02	0.0117	1.0642E-01	0.0114	4.1369E-02	0.0105	1.6493E-02	0.0096	5.9517E-03	0.0102
3.9810E-02	3.5732E-04	7E-04	2.4987E-02	0.0116	7.4774E-02	0.0121	1.0607E-01	0.0114	4.3148E-02	0.0103	1.7357E-02	0.0094	6.3976E-03	0.01
6.3100E-02	3.1509E-04	6E-04	2.2538E-02	0.0123	7.3417E-02	0.0123	1.1009E-01	0.0112	4.7623E-02	0.0098	1.9129E-02	0.0091	7.1512E-03	0.0096
1.0000E-01	2.9648E-04	6E-04	1.9728E-02	0.0132	6.8600E-02	0.0127	1.1124E-01	0.0111	5.1674E-02	0.0095	2.1765E-02	0.0087	8.1586E-03	0.009
1.5850E-01	4.1476E-04	8E-04	1.6145E-02	0.0144	6.4564E-02	0.013	1.1660E-01	0.0109	5.9482E-02	0.009	2.5866E-02	0.0081	9.9885E-03	0.0084
2.5120E-01	1.3838E-03	6E-04	1.4091E-02	0.0152	5.8057E-02	0.0136	1.1793E-01	0.0108	6.9633E-02	0.0084	3.2395E-02	0.0074	1.3056E-02	0.0077
3.9810E-01	2.6662E-04	7E-04	1.0782E-02	0.0176	4.8588E-02	0.0149	1.2207E-01	0.0107	8.3838E-02	0.0078	4.2731E-02	0.0067	1.8567E-02	0.0068
6.3100E-01	1.4007E-04	7E-04	7.5478E-03	0.0207	4.2033E-02	0.0161	1.1686E-01	0.011	9.9173E-02	0.0072	5.7464E-02	0.006	2.7575E-02	0.006
1.0000E+00	1.1041E-04	7E-04	5.1432E-03	0.0251	3.1160E-02	0.0187	1.0752E-01	0.0114	1.1364E-01	0.0068	7.5853E-02	0.0054	4.2229E-02	0.0051
1.5850E+00	1.0190E-04	7E-04	3.4205E-03	0.0307	2.2527E-02	0.022	9.4873E-02	0.0122	1.1949E-01	0.0066	9.3716E-02	0.0049	6.1378E-02	0.0045
2.5120E+00	9.0153E-05	7E-04	2.0297E-03	0.0396	1.4835E-02	0.0271	7.2785E-02	0.0138	1.1628E-01	0.0067	1.0380E-01	0.0047	7.8172E-02	0.0041
3.9810E+00	5.1723E-05	0.001	1.2099E-03	0.0366	9.3005E-03	0.0343	5.2416E-02	0.0127	9.9524E-02	0.0073	9.7379E-02	0.0067	8.3129E-02	0.0075
6.3100E+00	3.0792E-05	0.001	7.4114E-04	0.046	5.8399E-03	0.0422	3.7953E-02	0.0149	8.1682E-02	0.008	8.7536E-02	0.007	8.2910E-02	0.0074
1.0000E+01	1.9001E-05	0.003	3.6405E-04	0.0651	3.2796E-03	0.0575	2.2152E-02	0.0193	5.6714E-02	0.0132	6.8812E-02	0.0131	7.3922E-02	0.0148
1.5850E+01	1.2217E-05	0.004	2.4233E-04	0.0826	2.1304E-03	0.0713	1.6255E-02	0.0226	4.3235E-02	0.0153	5.5268E-02	0.0146	6.0233E-02	0.0162
2.5120E+01	8.7654E-06	0.006	1.2206E-04	0.1074	9.8677E-04	0.0997	8.0351E-03	0.0312	2.5472E-02	0.0197	3.5116E-02	0.0184	3.9687E-02	0.019

Appendix F. MCNP6 Input Cards for Modeling ^{239}PuBe

```
c cell cards
100     1     -2.3        -10 20       imp:n=1            $ Concrete walls of world (rpp)
200     2     -0.001205   -20 31       imp:n=1            $ Air in world (rpp)
310     3     -0.95       -31 32       imp:n=20           $ Poly detector
320     3     -0.95       -32 33       imp:n=23           $ Poly detector
330     3     -0.95       -33 34       imp:n=32           $ Poly detector
340     3     -0.95       -34 35       imp:n=70           $ Poly detector
350     3     -0.95       -35 36       imp:n=200          $ Poly detector
360     3     -0.95       -36 40       imp:n=600          $ Poly detector
400     6     -2.6989     -40 41       imp:n=4450         $ Aluminum tube
410     0                 -41 42       imp:n=1200000      $ Vaccuum in the tube
420     7     -3.84       -42          imp:n=60000        $ LiI(Eu) detector, modeled
999     0                  10          imp:n=0            $ Rest of the world

c surface cards
10   rpp   -188 188  -188 188  -188 188                   $ World volume
20   rpp   -127 127  -127 127  -127 127                   $ Air within (0,0,0)
31   so    15.25                                          $ Poly detector (12" sphere)
32   so    12.7                                           $ Poly detector (10" sphere)
33   so    10.15                                          $ Poly detector (8" sphere)
34   so    6.35                                           $ Poly detector (5" sphere)
35   so    3.81                                           $ Poly detector (3" sphere)
36   so    2.54                                           $ Poly detector (2" sphere)
40   rcc   0 0 -0.8  0 0 1.6  0.725                       $ Al rcc (perpendicular to source)
41   rcc   0 0 -0.6  0 0 1.2  0.525                       $ Vaccuum in the Al cylinder
42   rcc   0 0 -0.2  0 0 0.4  0.2                         $ LiI(Eu) crystal (RCC r=2mm, ht=4mm)

c material specification
m1   1001 -0.022100 6012 -0.002484 8016 -0.574930         $ Ordinary concrete
     11023 -0.015208 12000 -0.001266 13027 -0.019953
     14000 -0.304627 19000 -0.010045 20000 -0.042951
     26000 -0.006435
m2   07014 -0.755268 06000 -0.000124                      $ Air
     08016 -0.231781 18000 -0.012827
m3   01001 -0.143716 06012 -0.856284                      $ Polyethylene (Bonner)
m6   13027 -1.000000                                      $ Al metal
m7   03006 -0.0518  53127 -0.9482                         $ LiI crystal composition
mode n
SDEF POS=-92 0 0 PAR=n ERG=D1
SI1  0 2.50E-01 5.00E-01 7.50E-01 1.00E+00 1.25E+00
     1.50E+00 1.75E+00 2.00E+00 2.25E+00 2.50E+00
     2.75E+00 3.00E+00 3.25E+00 3.50E+00 3.75E+00
     4.00E+00 4.25E+00 4.50E+00 4.75E+00 5.00E+00
     5.25E+00 5.50E+00 5.75E+00 6.00E+00 6.25E+00
     6.50E+00 6.75E+00 7.00E+00 7.25E+00 7.50E+00
     7.75E+00 8.00E+00 8.25E+00 8.50E+00 8.75E+00
     9.00E+00 9.25E+00 9.50E+00 9.75E+00 1.00E+01
     1.03E+01 1.05E+01 1.08E+01 1.10E+01 1.13E+01
     1.15E+01 1.18E+01 1.20E+01
SP1  0 2.43E-04 5.07E-03 1.32E-02 1.62E-02 1.61E-02
     1.42E-02 1.04E-02 1.47E-02 1.81E-02 2.04E-02
     2.61E-02 3.93E-02 4.87E-02 4.68E-02 4.46E-02
     4.16E-02 3.93E-02 3.75E-02 3.55E-02 3.31E-02
     2.76E-02 2.15E-02 1.88E-02 1.70E-02 1.42E-02
     1.89E-02 2.20E-02 2.25E-02 2.25E-02 2.24E-02
     2.19E-02 2.05E-02 1.86E-02 1.68E-02 1.56E-02
     1.48E-02 1.40E-02 1.21E-02 8.62E-03 5.44E-03
     3.24E-03 1.79E-03 5.45E-04 5.37E-05 6.02E-07
     1.11E-08 8.77E-09 6.92E-09
nps  22000000                                             $ Number of neutrons generated
F4:n 420                                                  $ Flux point detector with 15.25 cm radius
MT3 poly.10t                                              $ S(a,B) treatment for hydorgen in polyethylene
E4   1.0E-08 2.512e-8 6.31e-8 1e-7 2.51e-7 1e-6 1e-5
     1e-4 1e-3 1e-2 2.512e-2 3.981e-2 6.31e-2 1e-1
     1.585e-1 2.50E-01 5.00E-01 7.50E-01 1 1.25
     1.50E+00 1.75E+00 2.00E+00 2.25E+00 2.50E+00
     2.75E+00 3.00E+00 3.25E+00 3.50E+00 3.75E+00
     4.00E+00 4.25E+00 4.50E+00 4.75E+00 5.00E+00
     5.25E+00 5.50E+00 5.75E+00 6.00E+00 6.25E+00
     6.50E+00 6.75E+00 7.00E+00 7.25E+00 7.50E+00
     7.75E+00 8.00E+00 8.25E+00 8.50E+00 8.75E+00
     9.00E+00 9.25E+00 9.50E+00 9.75E+00 1.00E+01
     1.03E+01 1.05E+01 1.08E+01 1.10E+01 1.13E+01
     1.15E+01 1.18E+01 1.20E+01
```

Appendix G. MCNP6 Input Cards for Modeling the Steel Box and Free-Field

MCNP6 Steel Box Input Card

```
c cell cards
100     1     -0.001205  -10 20 51 52 53 54 55 56 57 58 59 60 61 imp:n=1   $ Air in world (rpp)
200     2     -7.82      -20 30 60    imp:n=1            $ Steel Box
300     1     -0.001205  -30 31 60    imp:n=1            $ Air in steel shield (box)
310     3     -0.95      -31 32       imp:n=20           $ Poly detector
320     3     -0.95      -32 33       imp:n=23           $ Poly detector
330     3     -0.95      -33 34       imp:n=32           $ Poly detector
340     3     -0.95      -34 35       imp:n=70           $ Poly detector
350     3     -0.95      -35 36       imp:n=200          $ Poly detector
360     3     -0.95      -36 40       imp:n=700          $ Poly detector
400     6     -2.6989    -40 41       imp:n=4450         $ Aluminum tube
410     0                -41 42       imp:n=1200000      $ Vaccuum in the tube
420     7     -3.84      -42          imp:n=60000        $ LiI(Eu) detector, modeled
510     4     -0.95      -51 61       imp:n=1            $ BP side
520     4     -0.95      -52 61       imp:n=1            $ BP side
530     4     -0.95      -53          imp:n=1            $ BP top
540     4     -0.95      -54          imp:n=1            $ BP bottom
550     4     -0.95      -55          imp:n=1            $ BP outer side
560     4     -0.95      -56          imp:n=1            $ BP outer side
570     4     -0.95      -57          imp:n=1            $ BP back
580     5     -0.705     -58          imp:n=1            $ Wooden table (Birch)
590     4     -0.95      -59          imp:n=1            $ BP behind source
600     1     -0.001205  -60          imp:n=1            $ Air in hole
610     6     -2.6989    -61 62       imp:n=1            $ Aluminum source tube
620     0                -62          imp:n=1            $ Vacuum in source tube
999     0                 10          imp:n=0            $ Rest of the world

c surface cards
10   rpp   -100 150  -50 50  -50 50                      $ World volume
20   rpp   -30.5 30.5  -30.5 30.5 -30.5 30.5             $ Steel box at (0,0,0)
30   rpp   -28 28  -28 28  -28 28                        $ Air in box
31   so    15.25                                         $ Poly detector (12" sphere)
32   so    12.7                                          $ Poly detector (10" sphere)
33   so    10.15                                         $ Poly detector (8" sphere)
34   so    6.35                                          $ Poly detector (5" sphere)
35   so    3.81                                          $ Poly detector (3" sphere)
36   so    2.54                                          $ Poly detector (2" sphere)
40   rcc   0 0 -0.8  0 0 1.6  0.725                      $ Al rcc (perpendicular to source)
41   rcc   0 0 -0.6  0 0 1.2  0.525                      $ Vaccuum in the Al cylinder
42   rcc   0 0 -0.2  0 0 0.4  0.2                        $ LiI(Eu) crystal (RCC r=2mm, ht=4mm)
51   rpp 31.8175 102.255 21.59 32.07 -30.5 30.5          $ 4" thick BP side shielding
52   rpp 31.8175 102.255 -32.07 -21.59 -30.5 30.5        $ 4" thick BP side shielding
53   rpp -30.5 91.78 -30.5 30.5 31.135 41.6125           $ Top BP shield, length of box
54   rpp 31.8175 102.255 -21.58 21.58 -30.5 -20.02       $ Bottom BP, under source
55   rpp -30.5 30.5 31.135 41.295 -30.5 30.5             $ BP Outer side
56   rpp -30.5 30.5 -41.295 -31.135 -30.5 30.5           $ BP Outer side
57   rpp -41.495 -31.135 -30.5 30.5 -30.5 30.5           $ BP Back
58   rpp -45 105 -45 45 -40 -30.5                        $ Wooden Table
59   rpp 92.095 102.255  -21.58 21.58 -20.02 30.5        $ BP Back behind source
60   rcc 0 0 27.5 0 0 3.5  7.12                          $ Hole through steel plate
61   rcc 67.3 -33 -8.91 0 66 0 7.62
62   rcc 67.3 -31 -8.91 0 62 0 5.62

c material specification
m1   07014 -0.755268 06000 -0.000124                     $ Air
     08016 -0.231781 18000 -0.012827
m2   26000 -0.977170 06012 -0.022831                     $ Shield, carbon steel
m3   01001 -0.143716 06012 -0.856284                     $ Polyethylene (Bonner)
m4   01001 -0.143716  06012 -0.806284  05010 -0.05      $ Borated polyethylene (Shield)
m5   01001 -0.057889 06012 -.482667  08016 -0.459444    $ Wood table
m6   13027 -1.000000                                     $ Al metal
m7   03006 -0.0518  53127 -0.9482                        $ LiI crystal composition
mode n
SDEF POS=67.3 0 -8.91 PAR=n ERG=2.45
nps  20000000                                            $ Number of neutrons generated
F4:n 420                                                 $ Flux point detector with 15.25 cm radius
MT3 poly.10t                                             $ S(a,B) treatment for hydorgen in polyethylene
MT4 poly.10t
E4   1.0E-08 2.512e-8 6.31e-8 1e-7 2.51e-7 1e-6 1e-5
      1e-4 1e-3 1e-2 2.512e-2 3.981e-2 6.31e-2 1e-1
      1.585e-1 2.50E-01 0.5 0.6 0.7 0.8 0.9 1.0 1.1 1.2
      1.3 1.4 1.5 1.6 1.7 1.8 1.9 2.0 2.1 2.2 2.3 2.4
      2.5 2.6 2.7 2.8
```

MCNP6 Free-Field Input Card

```
c cell cards
100     1     -0.001205  -10 31 51 52 53 54 55 56 57 58 59 61 imp:n=1   $ Air in world (rpp)
310     3     -0.95      -31 32       imp:n=20            $ Poly detector
320     3     -0.95      -32 33       imp:n=23            $ Poly detector
330     3     -0.95      -33 34       imp:n=32            $ Poly detector
340     3     -0.95      -34 35       imp:n=70            $ Poly detector
350     3     -0.95      -35 36       imp:n=200           $ Poly detector
360     3     -0.95      -36 40       imp:n=700           $ Poly detector
400     6     -2.6989    -40 41       imp:n=4450          $ Aluminum tube
410     0                -41 42       imp:n=1200000       $ Vaccuum in the tube
420     7     -3.84      -42          imp:n=60000         $ LiI(Eu) detector, modeled
510     4     -0.95      -51 61       imp:n=1             $ BP side
520     4     -0.95      -52 61       imp:n=1             $ BP side
530     4     -0.95      -53          imp:n=1             $ BP top
540     4     -0.95      -54          imp:n=1             $ BP bottom
550     4     -0.95      -55          imp:n=1             $ BP outer side
560     4     -0.95      -56          imp:n=1             $ BP outer side
570     4     -0.95      -57          imp:n=1             $ BP back
580     5     -0.705     -58          imp:n=1             $ Wooden table (Birch)
590     4     -0.95      -59          imp:n=1             $ BP behind source
610     6     -2.6989    -61 62       imp:n=1             $ Aluminum source tube
620     0                -62          imp:n=1             $ Vacuum in source tube
999     0                 10          imp:n=0             $ Rest of the world

c surface cards
10   rpp   -100 150  -50 50  -50 50                       $ World volume
31   so    15.25                                          $ Poly detector (12" sphere)
32   so    12.7                                           $ Poly detector (10" sphere)
33   so    10.15                                          $ Poly detector (8" sphere)
34   so    6.35                                           $ Poly detector (5" sphere)
35   so    3.81                                           $ Poly detector (3" sphere)
36   so    2.54                                           $ Poly detector (2" sphere)
40   rcc   0 0 -0.8  0 0 1.6  0.725                       $ Al rcc (perpendicular to source)
41   rcc   0 0 -0.6  0 0 1.2  0.525                       $ Vaccuum in the Al cylinder
42   rcc   0 0 -0.2  0 0 0.4  0.2                         $ LiI(Eu) crystal (RCC r=2mm, ht=4mm)
51   rpp 31.8175 102.255 21.59 32.07 -30.5 30.5           $ 4" thick BP side shielding
52   rpp 31.8175 102.255 -32.07 -21.59 -30.5 30.5         $ 4" thick BP side shielding
53   rpp -30.5 91.78 -30.5 30.5 31.135 41.6125            $ Top BP shield, length of box
54   rpp 31.8175 102.255 -21.58 21.58 -30.5 -20.02        $ Bottom BP, under source
55   rpp -30.5 30.5  21.59 32.07  -30.5 30.5              $ BP Outer side
56   rpp -30.5 30.5  -32.07 -21.59  -30.5 30.5            $ BP Outer side
57   rpp -41.495 -31.135 -30.5 30.5 -30.5 30.5            $ BP Back
58   rpp -45 105 -45 45 -40 -30.5                         $ Wooden Table
59   rpp 92.095 102.255  -21.58 21.58 -20.02 30.5         $ BP Back behind source
61   rcc 67.3 -33 -8.91 0 66 0 7.62
62   rcc 67.3 -31 -8.91 0 62 0 5.62

c material specification
m1   07014 -0.755268 06000 -0.000124                      $ Air
     08016 -0.231781 18000 -0.012827
m2   26000 -0.977170 06012 -0.022831                      $ Shield, carbon steel
m3   01001 -0.143716 06012 -0.856284                      $ Polyethylene (Bonner)
m4   01001 -0.143716  06012 -0.806284  05010 -0.05        $ Borated polyethylene (Shield)
m5   01001 -0.057889 06012 -.482667  08016 -0.459444      $ Wood table
m6   13027 -1.000000                                      $ Al metal
m7   03006 -0.0518  53127 -0.9482                         $ LiI crystal composition
mode n
SDEF POS=67.3 0 -8.91 PAR=n ERG=2.45
nps  20000000                                             $ Number of neutrons generated
F4:n 420                                                  $ Flux point detector with 15.25 cm radius
MT3 poly.10t                                              $ S(a,B) treatment for hydorgen in polyethylene
MT4 poly.10t
E4   1.0E-08 2.512e-8 6.31e-8 1e-7 2.51e-7 1e-6 1e-5
      1e-4 1e-3 1e-2 2.512e-2 3.981e-2 6.31e-2 1e-1
      1.585e-1 2.50E-01 0.5 0.6 0.7 0.8 0.9 1.0 1.1 1.2
      1.3 1.4 1.5 1.6 1.7 1.8 1.9 2.0 2.1 2.2 2.3 2.4
      2.5 2.6 2.7 2.8
```

Appendix H. MAXED Output and Spectrum for ^{239}PuBe Measurements

MAXED ^{239}PuBe Output

```
UMG package, version 3.3, release date: March 1, 2004

Deconvolution Using the MAXED (Maximum Entropy) Algorithm
==========================================================

File with Input Data :  AFIT_PuBeN.ibu

File with Default Spectrum         :  c:\U_M_G\FC\$inp\def_spec\AFIT_PuBen.flu
Default Spectrum Fluence Format    : fluence rate per bin
Energy of Default Sp.  in Units of : MeV

File with Response Function        :  c:\U_M_G\FC\$inp\response\AFIT_RF.fmt
Response Functions     in Units of :      cm^
Energy of Final Spect. in Units of : MeV

Chi-squared P.D.F. Using the Default Spectrum     =    3.615
Final Chi-squared P.D.F.                          =    0.973
NOTE: Chi-squared Per Degree of Freedom was set to:    0.800


*** RESULTS FOR THE FINAL SPECTRUM: ***

     DN              M             C      (C-M)/S     (C-M)/M
      1   5.270000E+00  1.829808E+00    -0.90663    -0.65279
      2   8.770000E+00  2.072266E+00    -1.06069    -0.76371
      3   1.303000E+00  1.697030E+00     0.42000     0.30240
      4   1.877000E+00  1.472146E+00    -0.26304    -0.21569
      5   1.597000E+00  1.712727E+00     0.22643     0.07247
      6   1.104000E+00  1.717651E+00     0.89650     0.55584
      7   8.680000E+00  1.610143E+00    -1.93918    -0.81450

Note 1: DN = detector number
        M = measured count rate
        C = calculated count rate
        S = estimated standard uncertainty
Note 2: M<0 indicates data not used for the deconvolution
```

MAXED Output Solution for ^{239}PuBe Source

Energy (MeV)	^{239}PuBe Flux	Energy (MeV)	^{239}PuBe Flux
1.0000E-08	7.8110E+07	4.2500E+00	7.0183E+00
2.5120E-08	2.0855E+08	4.5000E+00	5.4517E+00
6.3100E-08	4.4526E+08	4.7500E+00	6.0586E+00
1.0000E-07	8.7965E+06	5.0000E+00	2.5938E+00
2.5100E-07	6.3547E+03	5.2500E+00	4.7464E+00
1.0000E-06	1.1165E-01	5.5000E+00	3.9767E+00
1.0000E-05	6.7033E-04	5.7500E+00	3.7940E+00
1.0000E-04	6.2042E-05	6.0000E+00	2.2834E+00
1.0000E-03	2.8868E-05	6.2500E+00	2.2917E+00
1.0000E-02	5.3245E-05	6.5000E+00	5.3981E+00
2.5120E-02	3.5651E-05	6.7500E+00	1.7202E+00
3.9810E-02	1.8857E-05	7.0000E+00	4.0451E+00
6.3100E-02	1.8940E-05	7.2500E+00	4.2010E+00
1.0000E-01	2.8423E-05	7.5000E+00	1.0645E+00
1.5850E-01	6.7204E-05	7.7500E+00	9.6518E-01
2.5000E-01	1.2182E-04	8.0000E+00	1.0072E+00
5.0000E-01	5.8794E-04	8.2500E+00	7.4472E-01
7.5000E-01	1.1035E-03	8.5000E+00	1.8590E+00
1.0000E+00	2.3524E-02	8.7500E+00	6.2494E-01
1.2500E+00	2.0349E-02	9.0000E+00	5.8265E-01
1.5000E+00	1.1641E-01	9.2500E+00	1.5385E+00
1.7500E+00	3.5567E-01	9.5000E+00	3.4671E-01
2.0000E+00	2.7757E-01	9.7500E+00	1.7388E-01
2.2500E+00	2.7691E-01	1.0000E+01	4.4166E-04
2.5000E+00	2.2262E+00	1.0300E+01	1.1381E-03
2.7500E+00	1.7196E+00	1.0500E+01	0.0000E+00
3.0000E+00	1.5052E+00	1.0800E+01	0.0000E+00
3.2500E+00	2.2404E+00	1.1000E+01	0.0000E+00
3.5000E+00	1.2746E+00	1.1300E+01	0.0000E+00
3.7500E+00	1.5683E+00	1.1500E+01	0.0000E+00
4.0000E+00	5.0879E+00	1.1800E+01	0.0000E+00

Appendix I. MCNP6 Output for ^{239}PuBe Spectrum

Energy (MeV)	^{239}PuBe Flux	Energy (MeV)	^{239}PuBe Flux
1.0000E-08	5.7156E-08	4.5000E+00	8.1889E-08
2.5120E-08	3.4394E-07	4.7500E+00	9.1005E-08
6.3100E-08	1.2202E-06	5.0000E+00	3.8961E-08
1.0000E-07	7.3768E-07	5.2500E+00	7.1294E-08
2.5100E-07	5.3714E-07	5.5000E+00	5.9733E-08
1.0000E-06	1.6476E-07	5.7500E+00	5.6989E-08
1.0000E-05	3.0224E-07	6.0000E+00	3.4299E-08
1.0000E-04	3.1161E-07	6.2500E+00	4.8307E-08
1.0000E-03	3.5782E-07	6.5000E+00	1.2664E-07
1.0000E-02	3.8316E-07	6.7500E+00	4.0356E-08
2.5120E-02	1.5985E-07	7.0000E+00	9.4898E-08
3.9810E-02	9.3015E-08	7.2500E+00	9.8555E-08
6.3100E-02	8.9080E-08	7.5000E+00	2.4972E-08
1.0000E-01	9.2083E-08	7.7500E+00	2.2643E-08
1.5850E-01	1.2496E-07	8.0000E+00	2.3630E-08
2.5000E-01	1.5200E-07	8.2500E+00	1.7471E-08
5.0000E-01	3.2310E-07	8.5000E+00	4.3612E-08
7.5000E-01	2.2881E-07	8.7500E+00	1.4661E-08
1.0000E+00	1.9723E-07	9.0000E+00	1.3669E-08
1.2500E+00	1.7061E-07	9.2500E+00	3.6092E-08
1.5000E+00	1.5140E-07	9.5000E+00	8.1338E-09
1.7500E+00	1.7711E-07	9.7500E+00	4.0793E-09
2.0000E+00	1.3822E-07	1.0000E+01	2.2904E-10
2.2500E+00	1.3789E-07	1.0300E+01	3.9348E-10
2.5000E+00	1.3972E-07	1.0500E+01	0.0000E+00
2.7500E+00	9.7225E-08	1.0800E+01	0.0000E+00
3.0000E+00	8.5104E-08	1.1000E+01	0.0000E+00
3.2500E+00	1.2667E-07	1.1300E+01	0.0000E+00
3.5000E+00	7.2066E-08	1.1500E+01	0.0000E+00
3.7500E+00	8.0171E-08	1.1800E+01	0.0000E+00
4.0000E+00	7.6425E-08	1.2000E+01	0.0000E+00
4.2500E+00	1.0542E-07		

Appendix J. MCNP6 Output for Steel Box Spectrum (MAXED *a priori*)

Energy (MeV)	Steel Box Flux	Uncertainty	Energy (MeV)	Steel Box Flux	Uncertainty
1.00E-08	8.94E-08	0.0143	9.00E-01	8.09E-08	0.1013
2.51E-08	5.49E-07	0.0081	1.00E+00	9.91E-08	0.1142
6.31E-08	1.93E-06	0.0058	1.10E+00	7.67E-08	0.1158
1.00E-07	1.17E-06	0.008	1.20E+00	7.07E-08	0.1115
2.51E-07	8.33E-07	0.0109	1.30E+00	5.63E-08	0.1266
1.00E-06	2.25E-07	0.0319	1.40E+00	7.75E-08	0.1262
1.00E-05	4.29E-07	0.0283	1.50E+00	5.74E-08	0.1517
1.00E-04	4.09E-07	0.0315	1.60E+00	9.69E-08	0.1541
1.00E-03	4.47E-07	0.032	1.70E+00	5.34E-08	0.1605
1.00E-02	4.87E-07	0.0311	1.80E+00	6.96E-08	0.166
2.51E-02	2.03E-07	0.0482	1.90E+00	7.90E-08	0.1653
3.98E-02	1.01E-07	0.0639	2.00E+00	3.33E-08	0.2245
6.31E-02	1.14E-07	0.0634	2.10E+00	4.08E-08	0.1862
1.00E-01	1.31E-07	0.0564	2.20E+00	3.38E-08	0.2518
1.59E-01	1.55E-07	0.0539	2.30E+00	8.36E-08	0.2577
2.50E-01	1.73E-07	0.0515	2.40E+00	1.08E-07	0.2177
5.00E-01	3.73E-07	0.0415	2.50E+00	1.28E-07	0.2534
6.00E-01	1.21E-07	0.074	2.60E+00	0.00E+00	0
7.00E-01	1.12E-07	0.088	2.70E+00	0.00E+00	0
8.00E-01	1.12E-07	0.0943	2.80E+00	0.00E+00	0

Appendix K. MAXED Output and Flux Spectrum of the Steel Box

MAXED Output for the Steel Box

```
Deconvolution Using the MAXED (Maximum Entropy) Algorithm
==========================================================

File with Input Data :  AFIT_Exp_BoxN1.ibu

File with Default Spectrum          :  c:\U_M_G\FC\$inp\def_spec\AFIT_Box2.flu
Default Spectrum Fluence Format     : fluence rate per bin
Energy of Default Sp.  in Units of : MeV

File with Response Function         :  c:\U_M_G\FC\$inp\response\AFIT_RF.fmt
Response Functions     in Units of :       cm^
Energy of Final Spect. in Units of : MeV

Chi-squared P.D.F. Using the Default Spectrum     =   16.036
Final Chi-squared P.D.F.                          =    0.863
NOTE: Chi-squared Per Degree of Freedom was set to:    0.700


*** RESULTS FOR THE FINAL SPECTRUM: ***

     DN              M             C      (C-M)/S     (C-M)/M
      1   1.189000E+00  1.197886E+00     0.06224     0.00747
      2   6.712000E+00  1.681162E+00    -2.34209    -0.74953
      3   1.500000E+00  1.640234E+00     0.42488     0.09349
      4   2.702500E+00  2.040542E+00    -0.47103    -0.24494
      5   2.487400E+00  2.092365E+00    -0.37811    -0.15881
      6   1.659600E+00  1.660692E+00     0.00072     0.00066
      7   1.077700E+00  1.144632E+00     0.08626     0.06211

Note 1: DN = detector number
        M = measured count rate
        C = calculated count rate
        S = estimated standard uncertainty
Note 2: M<0 indicates data not used for the deconvolution
```

MAXED Flux Spectrum Solution for the Steel Box

Energy (MeV)	MAXED Box Flux	Energy (MeV)	MAXED Box Flux
1.0000E-08	4.0334E+07	9.0000E-01	2.0157E+00
2.5100E-08	1.6434E+08	1.0000E+00	1.3514E+01
6.3100E-08	5.3309E+08	1.1000E+00	1.2198E+01
1.0000E-07	2.7846E+07	1.2000E+00	1.0010E+01
2.5100E-07	9.3852E+04	1.3000E+00	1.3514E+01
1.0000E-06	4.3115E+00	1.4000E+00	1.0237E+01
1.0000E-05	2.4589E-02	1.5000E+00	9.5260E+00
1.0000E-04	1.1646E-03	1.6000E+00	1.2782E+01
1.0000E-03	2.6733E-04	1.7000E+00	1.4579E+01
1.0000E-02	3.9401E-04	1.8000E+00	1.5485E+01
2.5100E-02	2.6819E-04	1.9000E+00	1.1993E+01
3.9800E-02	1.4810E-04	2.0000E+00	9.8020E+00
6.3100E-02	2.3956E-04	2.1000E+00	1.3585E+01
1.0000E-01	5.4736E-04	2.2000E+00	9.3053E+00
1.5900E-01	2.8552E-03	2.3000E+00	1.3147E+01
2.5000E-01	3.1553E-02	2.4000E+00	1.8260E+01
5.0000E-01	5.7347E-01	2.5000E+00	1.0058E+01
6.0000E-01	1.1219E+00	2.6000E+00	0.0000E+00
7.0000E-01	2.6469E+00	2.7000E+00	0.0000E+00
8.0000E-01	2.2804E+00		

Appendix L. MCNP6 Output for Free-Field Spectrum (MAXED *a priori*)

Energy (MeV)	Free-Field Flux	Uncertainty	Energy (MeV)	Free-Field Flux	Uncertainty
1.00E-08	1.01E-07	0.0135	9.00E-01	9.90E-08	0.0844
2.51E-08	6.17E-07	0.0076	1.00E+00	1.13E-07	0.0999
6.31E-08	2.18E-06	0.0055	1.10E+00	1.02E-07	0.1007
1.00E-07	1.32E-06	0.0076	1.20E+00	8.37E-08	0.1042
2.51E-07	9.56E-07	0.0103	1.30E+00	1.13E-07	0.1236
1.00E-06	2.66E-07	0.0294	1.40E+00	8.56E-08	0.1177
1.00E-05	4.74E-07	0.027	1.50E+00	7.73E-08	0.1204
1.00E-04	4.99E-07	0.0286	1.60E+00	8.75E-08	0.1199
1.00E-03	5.21E-07	0.0293	1.70E+00	9.98E-08	0.1364
1.00E-02	5.53E-07	0.0291	1.80E+00	1.06E-07	0.1436
2.51E-02	2.49E-07	0.0438	1.90E+00	8.21E-08	0.1239
3.98E-02	1.29E-07	0.0559	2.00E+00	6.71E-08	0.1467
6.31E-02	1.50E-07	0.0551	2.10E+00	9.30E-08	0.172
1.00E-01	1.61E-07	0.0523	2.20E+00	6.37E-08	0.1983
1.59E-01	1.86E-07	0.0477	2.30E+00	9.00E-08	0.1783
2.50E-01	2.08E-07	0.0471	2.40E+00	1.25E-07	0.165
5.00E-01	4.38E-07	0.0366	2.50E+00	3.33E-07	0.1671
6.00E-01	1.29E-07	0.0637	2.60E+00	0.00E+00	0
7.00E-01	1.30E-07	0.0725	2.70E+00	0.00E+00	0
8.00E-01	1.12E-07	0.0819	2.80E+00	0.00E+00	0

Appendix M. MAXED Output and Flux Spectrum of Free-Field Measurements

MAXED Output for Free-Field

```
Deconvolution Using the MAXED (Maximum Entropy) Algorithm
==========================================================

File with Input Data :  AFIT_Exp_FFsc2.ibu

File with Default Spectrum         :  c:\U_M_G\FC\$inp\def_spec\AFIT_DSFF.flu
Default Spectrum Fluence Format    : fluence rate per bin
Energy of Default Sp.  in Units of : MeV

File with Response Function        :  c:\U_M_G\FC\$inp\response\AFIT_RF.fmt
Response Functions     in Units of :      cm^
Energy of Final Spect. in Units of : MeV

Chi-squared P.D.F. Using the Default Spectrum     =   18.204
Final Chi-squared P.D.F.                          =    0.907
NOTE: Chi-squared Per Degree of Freedom was set to:    0.900


*** RESULTS FOR THE FINAL SPECTRUM: ***

     DN              M             C      (C-M)/S      (C-M)/M
      1   2.168000E+00  2.067824E+00    -0.41974     -0.04621
      2   9.801000E+00  2.525952E+00    -2.31942     -0.74228
      3   2.092100E+00  2.302488E+00     0.47878      0.10056
      4   3.604100E+00  2.613070E+00    -0.52878     -0.27497
      5   3.383700E+00  2.651812E+00    -0.51497     -0.21630
      6   2.414100E+00  2.139240E+00    -0.12376     -0.11386
      7   1.571500E+00  1.508814E+00    -0.05540     -0.03989

Note 1: DN = detector number
        M = measured count rate
        C = calculated count rate
        S = estimated standard uncertainty
Note 2: M<0 indicates data not used for the deconvolution
```

MAXED Flux Spectrum Solution for the Free-Field

Energy (MeV)	MAXED Free-Field Flux	Energy (MeV)	MAXED Free-Field Flux
1.0000E-08	2.4864E+06	9.0000E-01	2.7243E+00
2.5100E-08	3.7014E+07	1.0000E+00	1.6255E+01
6.3100E-08	2.5495E+08	1.1000E+00	1.2581E+01
1.0000E-07	4.8883E+07	1.2000E+00	1.1597E+01
2.5100E-07	4.6585E+05	1.3000E+00	9.2347E+00
1.0000E-06	2.2249E+01	1.4000E+00	1.2712E+01
1.0000E-05	4.5264E-02	1.5000E+00	9.0901E+00
1.0000E-04	7.8973E-04	1.6000E+00	1.2576E+01
1.0000E-03	1.3061E-04	1.7000E+00	6.9304E+00
1.0000E-02	2.0881E-04	1.8000E+00	9.0329E+00
2.5100E-02	1.3299E-04	1.9000E+00	1.0253E+01
3.9800E-02	6.7001E-05	2.0000E+00	4.3218E+00
6.3100E-02	1.1574E-04	2.1000E+00	5.2951E+00
1.0000E-01	2.9742E-04	2.2000E+00	4.3867E+00
1.5900E-01	2.0187E-03	2.3000E+00	1.0850E+01
2.5000E-01	3.7371E-02	2.4000E+00	1.4017E+01
5.0000E-01	6.8760E-01	2.5000E+00	2.5384E+00
6.0000E-01	1.6557E+00	2.6000E+00	0.0000E+00
7.0000E-01	3.7716E+00	2.7000E+00	0.0000E+00
8.0000E-01	3.7716E+00		

Appendix N. MCNP6 NPF Calculation Spectra

MCNP6 Steel Box Spectrum

Energy (MeV)	Steel Box Flux	Uncertainty	Energy (MeV)	Steel Box Flux	Uncertainty
1.00E-08	8.9442E-08	0.010	9.00E-01	7.9748E-08	0.073
2.51E-08	5.4303E-07	0.006	1.00E+00	9.5966E-08	0.078
6.31E-08	1.9268E-06	0.004	1.10E+00	8.2029E-08	0.084
1.00E-07	1.1658E-06	0.006	1.20E+00	8.5693E-08	0.094
2.51E-07	8.3459E-07	0.008	1.30E+00	6.2441E-08	0.090
1.00E-06	2.2470E-07	0.023	1.40E+00	7.3567E-08	0.093
1.00E-05	4.1795E-07	0.020	1.50E+00	7.1905E-08	0.108
1.00E-04	4.1288E-07	0.022	1.60E+00	7.7271E-08	0.109
1.00E-03	4.5110E-07	0.023	1.70E+00	6.3448E-08	0.112
1.00E-02	4.7224E-07	0.022	1.80E+00	6.2932E-08	0.117
2.51E-02	1.9709E-07	0.035	1.90E+00	7.0959E-08	0.113
3.98E-02	1.0564E-07	0.044	2.00E+00	4.0566E-08	0.148
6.31E-02	1.0955E-07	0.045	2.10E+00	4.4093E-08	0.141
1.00E-01	1.3092E-07	0.040	2.20E+00	4.5651E-08	0.161
1.59E-01	1.5814E-07	0.038	2.30E+00	7.5676E-08	0.169
2.50E-01	1.7363E-07	0.037	2.40E+00	1.0877E-07	0.167
5.00E-01	3.7284E-07	0.029	2.50E+00	1.5317E-07	0.163
6.00E-01	1.2151E-07	0.055	2.60E+00	0.0000E+00	0.000
7.00E-01	1.0925E-07	0.061	2.70E+00	0.0000E+00	0.000
8.00E-01	1.0525E-07	0.067	2.80E+00	0.0000E+00	0.000

MCNP6 Free-Field Spectrum

Energy (MeV)	Free-Field Flux	Uncertainty	Energy (MeV)	Free-Field Flux	Uncertainty
1.00E-08	1.02E-07	0.0096	9.00E-01	1.02E-07	0.0597
2.51E-08	6.16E-07	0.0054	1.00E+00	1.10E-07	0.0712
6.31E-08	2.18E-06	0.0039	1.10E+00	1.06E-07	0.0766
1.00E-07	1.32E-06	0.0054	1.20E+00	8.28E-08	0.0753
2.51E-07	9.59E-07	0.0072	1.30E+00	9.96E-08	0.0856
1.00E-06	2.59E-07	0.0211	1.40E+00	8.09E-08	0.0874
1.00E-05	4.86E-07	0.0189	1.50E+00	8.19E-08	0.0903
1.00E-04	5.05E-07	0.0202	1.60E+00	8.44E-08	0.0924
1.00E-03	5.34E-07	0.0204	1.70E+00	8.21E-08	0.1022
1.00E-02	5.49E-07	0.0207	1.80E+00	9.31E-08	0.1048
2.51E-02	2.41E-07	0.0314	1.90E+00	9.52E-08	0.0994
3.98E-02	1.26E-07	0.0398	2.00E+00	6.57E-08	0.1323
6.31E-02	1.47E-07	0.0394	2.10E+00	7.94E-08	0.1234
1.00E-01	1.56E-07	0.0369	2.20E+00	7.15E-08	0.1333
1.59E-01	1.81E-07	0.0343	2.30E+00	8.94E-08	0.159
2.50E-01	2.08E-07	0.0334	2.40E+00	1.04E-07	0.1257
5.00E-01	4.33E-07	0.0261	2.50E+00	3.03E-07	0.1225
6.00E-01	1.42E-07	0.0495	2.60E+00	0.00E+00	0
7.00E-01	1.24E-07	0.0544	2.70E+00	0.00E+00	0
8.00E-01	1.17E-07	0.0593	2.80E+00	0.00E+00	0

Bibliography

[1] B. Obama, *Prague Speech*, Prague, April, 2009.

[2] J. C. Nellis and J. F. Marquart, "Protection Factors of Combat Systems," *Combating WMD Journal*, vol. Winter/Spring, no. 8, pp. 44-46, 2012.

[3] C. Eisenhauer and L. Spencer, "Approximate Procedure for Calculating Protection From Initial Nuclear Radiation From Weapons," National Bureau of Standards Center for Radiation Research, Gaithersburg, 1988.

[4] C. R. Heimbach, "Final Report of Radiation Shielding in Armored Vehicles," Defense Technical Information Center, Alexandria, 1988.

[5] R. Schwenk, A. Rainis and R. Rexroad, "Nuclear Vulnerability Analysis of the U.S. M60A1 Tank in an Initial Radiation Environment (#1998)," U.S. Army Armament Research and Development Command, Aberdeen Proving Grounds, 1977.

[6] S. Stueker, A. E. Rainis and R. E. Rexroad, "Calculation of Residual Radiation Protection Afforded by the M113A1 Armored Personnel Carrier," U.S. Army Armament Research and Development Command, Aberdeen Proving Grounds, 1978.

[7] S. Stueker, A. E. Rainis and R. M. Schwenk, "M113A1 Armored Personnel Carrier - Initial Radiation Protection Factors," U.S. Army Armament Research and Development Command, Aberdeen Proving Grounds, 1978.

[8] A. Rainis, J. Kinch and J. Jacobson, "Calculation of Residual Radiation Protection Afforded by the XM1 Medium Tank," U.S. Army Armament Research and Development Command, Aberdeen Proving Ground, 1980.

[9] M. A. Schmoke, W. J. Post and R. E. Rexroad, "Residual Radiation Shielding Characteristics of the XM-803 (MBT-70 Pilot II) Tank," USA Ballistic Research Laboratories, Aberdeen Proving Ground, 1973.

[10] J. A. Stoddard, "Fallout Protection Factor Analysis Capability," Defense Technology Information Center, San Diego, CA, 1987.

[11] A. F. Bielajew, Fundamentals of the Monte Carlo method for neutral and charged particle transport, Ann Arbor, MI: The University of Michigan, 2001.

[12] X.-5. M. C. Team, "MCNP-A General Monte Carlo N-Particle Transport Code, Version 5," Los Alamos National Laboratories, Los Alamos, 2003.

[13] H. Caton, "Radiation Transport Calculations of a Simple Structure Using the Vehicle Code System with 69-Group Cross Sections and the Monte-Carlo Neutron and Photon Code," Ballistic Research Laboratory, Aberdeen Proving Grounds, 1989.

[14] H. Caton and J. A. Morrissey, "Radiation Protection Factors of Selected Light Vehicles Against Residual Radiation," U.S. Army Laboratory Command: Ballistic Research Laboratory, Aberdeen Proving Ground, 1988.

[15] M. B. Emmett, W. A. Rhoades, R. L. Childs and J. O. Johnson, "A User's Manual for MASH 1.0 - A Monte Carlo Adjoint Shielding Code System (U)," Defense Technical Information Center, Alexandria, VA, 1993.

[16] G. Radulescu, C. O. Slater and D. E. Peplow, "Nuclear Vulnerability Analyses with MCNP: FY2006 Status Report," Nuclear Science and Technology Division, Ft. Belvoir, VA, 2007.

[17] S. G. Mashnik, J. S. Bull, H. G. Hughes, R. E. Prael and A. J. Sierk, "Current Status of MCNP6 as a simulation tool useful for space and accelerator applications," Los Alamos National Laboratory, Los Alamos, 2012.

[18] J. W. Durkee and M. R. James, "MCNP6 Verification and Validation for the MCNPX_65 and MCNPX_EXTENDED Test Sets," Los Alamos National Laboratory, Los Alamos, 2012.

[19] C. J. Bridgman, Introduction to the Physics of Nuclear Weapons Effects, Wright-Patterson AFB, OH: Air Force Institute of Technology, 2001.

[20] K. S. Krane, Introductory Nuclear Physics, Hoboken: John Wiley & Sons, 1988.

[21] R. L. Bramblett, R. I. Ewing and T. W. Bonner, "A New Type of Neutron Spectrometer," *Nuclear Instrument Methods,* vol. 1, p. 9, 1960.

[22] G. F. Knoll, Radiation Detection and Measurement (4th Ed.), Ann Arbor: John Wiley & Sons, Inc., 2010.

[23] M. Awschalmo and R. S. Sanna, "Applications of Bonner Sphere Detectors in Neutron Field Dosimetry," US department of Energy, New York, NY, 1983.

[24] M. Reginatto and P. Goldhagen, "MAXED, A Computer Code for the Deconvolusion of Multisphere Neutron Spectroscopy Data using the Maximum Entropy Method," Environmental Measurements Laboratory , New York, NY, 1998.

[25] A. V. Thmoas and A. V. Alevra, "Bonner Sphere Spectrometers - A Critical Review," *Nuclear Instruments and Methods in Physics Research,* vol. A, no. 476, pp. 12-20, 2002.

[26] M. Reginatto, B. Weigel, A. Zimbal and F. Langner, "UMG Version 3.3, Unfolding with Maxed and Gravel," Physkalisch-Technishe Bundesanstalt (PTB), Braunschweig, 2004.

[27] M. Team, "MCNP6 User's Manual," Los Alamos National Laboratory, Los Alamos, 2012.

[28] J. K. Shultis and J. K. Faw, "An MCNP Primer," Kansas State University, Manhattan, KS, 2011.

[29] C. R. Heimbach, "Radiation Protection-Factor Measurements of a Lined Iron Box in Simulated Fission and Fusion Tactical Nuclear Environments," Defense Technical Information Center, Alexandria, 1984.

[30] V. Mares and H. Schraube, "Evaluation of the response matrix of a Bonner sphere spectrometer with LiI detector from thermal energy to 100 MeV," *Nuclear Instruments and Methods in Physics Research,* vol. 337, pp. 461-473, 1994.

[31] B. N. Laboratory, "National Nuclear Data Center," Brookhaven National Laboratory, 2013. [Online]. Available: http://www.nndc.bnl.gov/sigma/plotCart.jsp?cursor_x=&cursor_y=&submit=Update+Plot&xmin=0.001&xmax=1.0E8&xscale=log&ymin=9.88254E-9&ymax=47240.5&yscale=log&width=700&height=500&legends=upperRightCorner&plot0=0&plot1=1&plot2=2&plot3=3. [Accessed 03 12 2013].

[32] D. E. Hinkle, W. Wiersma and S. G. Jurs, Applied Statistics for the Behavioral Sciences, Cengage Learning, 5th Ed., 2002.

[33] M. A. Oliver, "Army Pulse Radiation Facility (APRF) Gamma Dose Measurements," US Army Combat Systems Test Activity, Aberdeen Proving Grounds, MD, 1993.

[34] ENDF/B-VII.1, "National Nuclear Data Center," Brookhaven National Laboratory, 2011. [Online]. Available: http://www.nndc.bnl.gov/sigma/getPlot.jsp?evalid=15019&mf=3&mt=1&nsub=10. [Accessed 16 August 2013].

[35] A. Decker, *The NSERC Steel Box Construction Standard Operating Procedures (SOP)*, West Point, NY: NSERC, DTRA, 2013.

[36] D. J. Cossairt and K. Vaziri, "Neutron Dose Per Fluence and Weighting Factors for Use at High Energy Accelerators," FERMILAB-PUB-08-244-ESH-REV, Warrenville, IL, 2008.

[37] ICRP, 2010, "Conversion Coefficients for Radiological Protection Quantities for External Radiation Exposures," *ICRP Publication 116*, pp. 40 (2-5), Ann. ICRP.

[38] K. G. Veinot and N. E. Hertel, "Effective Quality Factors for Neutrons Based on the Revised ICRP/ICRU Recommendations," *Radiation Protection Dosimetry*, vol. 115, no. 1-4, pp. 536-541, 2005.

[39] A. Klett and B. Burgkhardt, *The New Remcounter LB6411: Measurement of neutron Ambient Dose Equivalent H*(10) according to ICRP60 with high sensitivity*, Bad Wildbad, GE: Forschungszentrum Karlsruhe GmbH, 1997.

Vita

MAJ Andrew W. Decker graduated from the United States Military Academy with a Bachelor of Science degree in General Psychology in June 2002. He was commissioned as a Second Lieutenant in the U.S. Army in the Military Intelligence branch. His first assignment was to the 172nd Separate Infantry Brigade, where he began assisting in the brigade's transition to becoming the 172nd Stryker Brigade Combat Team (SBCT). During that time, LT Decker served as an Infantry Battalion Assistant S2, an Executive Officer for the 572nd Military Intelligence Company, and a Platoon Leader twice. Shortly after the deployment of the 172nd SBCT to Iraq in August 2005, CPT Decker was selected serve as S2 for the 4-14 Cavalry Squadron, a position he held for the remainder of the 16-month tour, including the brigade's deployment extension to Baghdad in support of the 2006 "Surge."

Upon redeployment, CPT Decker was assigned to Ft. Huachuca in February 2007 to attend the Captain's Career Course (CCC), but he was unexpectedly selected to serve as the Deputy Secretary of the General Staff and speechwriter for the Commanding General of the U.S. Army Intelligence Center and Fort Huachuca. He successfully served two Commanding Generals before finally attending the CCC and was subsequently selected to return to Iraq as part of a Military Transition Team (MTT).

Deploying a second time to Iraq in December 2008, CPT Decker and his MTT directly supported the 9th Iraqi Army Division, living and working alongside their counterparts for nearly one year. CPT Decker interfaced directly with the Division G2, as well as the Reconnaissance, Surveillance, and Target Acquisition Battalion

Commander, to improve the intelligence collection capability and professionalism of the Iraqi forces.

Upon redeployment in December 2009, CPT Decker was assigned to the I Corps G2 at Ft. Lewis, Washington, where he served as an action officer in the G2 Operations Office for 18 months. After that time, CPT Decker deployed to Wright-Patterson AFB in August 2011 to attend Wright State University, and later the Air Force Institute of Technology, in pursuit of a Master of Science Degree in Nuclear Science. Upon graduation in March 2014, MAJ Decker will be assigned to the Defense Threat Reduction Agency (DTRA).

REPORT DOCUMENTATION PAGE

Form Approved
OMB No. 0704–0188

1. REPORT DATE (DD–MM–YYYY) 27-03-2014	2. REPORT TYPE Master's Thesis	3. DATES COVERED *(From — To)* June 2012 – March 2014
4. TITLE AND SUBTITLE Verification and Validation of Monte Carlo n-Particle Code 6 (MCNP6) with Neutron protection Factor Measurements of an Iron Box		5a. CONTRACT NUMBER 5b. GRANT NUMBER 5c. PROGRAM ELEMENT NUMBER
6. AUTHOR(S) Decker, Andrew W. MAJ, USA		5d. PROJECT NUMBER 13P318 5e. TASK NUMBER 5f. WORK UNIT NUMBER
7. PERFORMING ORGANIZATION NAME(S) AND ADDRESS(ES) Air Force Institute of Technology Graduate School of 2950 Hobson Way WPAFB OH 45433-7765		8. PERFORMING ORGANIZATION REPORT NUMBER
9. SPONSORING / MONITORING AGENCY NAME(S) AND ADDRESS(ES) Defense Threat Reduction Agency (DTRA) 8725 John J. Kingman Rd Stop 6201 Fort Belvoir, VA 22060-6201 (703) 767-5870 Dtra.publicaffairs@dtra.mil		10. SPONSOR/MONITOR'S ACRONYM(S) DTRA OP/CSU 11. SPONSOR/MONITOR'S REPORT NUMBER(S)

12. DISTRIBUTION / AVAILABILITY STATEMENT
Distribution A. Approved for Public Release; Distribution Unlimited

13. SUPPLEMENTARY NOTES

14. ABSTRACT

Using a 1984 benchmark experiment, MCNP6 replicated the neutron flux and neutron protection factor (NPF) measurements of an iron box, which simulated a basic military vehicle, resulting in less than 5% difference from the published results. Additionally, the neutron flux spectrum of a ^{239}PuBe source was characterized using a Bonner Sphere Spectrometer (BSS) and the solution unfolded using the Maximum Entropy Deconvolution (MAXED) program, producing a χ^2/df of 0.97. Utilizing a steel box provided by the DTRA, measurements of neutron flux from a D-D neutron accelerator were recorded via BSS inside and outside of the box. Both flux spectra were unfolded through MAXED using MCNP6 computations as *a priori*, which resulted in χ^2/df values of 0.86 and 0.91, respectively. NPF assessments of the steel box were then conducted using experimental and MCNP6 flux spectra for the box, as well as *H*(10)* scaling, with final results differing by less than 1%. MAXED software was leveraged for all flux spectrum unfolding, incorporating updated BSS response functions generated within this research from MCNP6. This experiment and its conclusions strongly support the verification and validation of MCNP6 for modeling NPF assessments of military vehicles.

15. SUBJECT TERMS
Radiation Protection Factor, Neutron Protection Factor, MCNP, Bonner Sphere

16. SECURITY CLASSIFICATION OF:			17. LIMITATION OF ABSTRACT	18. NUMBER OF PAGES	19a. NAME OF RESPONSIBLE PERSON
a. REPORT	b. ABSTRACT	c. THIS PAGE			McHale, Stephen R. LTC Ph.D. USA
U	U	U	UU	140	19b. TELEPHONE NUMBER (Include Area Code) (937) 255-6565 x4438 stephen.mchale@afit.edu

Standard Form 298 (Rev. 8–98)
Prescribed by ANSI Std. Z39.18